A STUDY OF EXOTIC COMPOUND NUCLEAR SYSTEMS AND SUBSEQUENT FRAGMENT EMISSION USING SKYRME ENERGY DENSITY FORMALISM

A THESIS

Submitted for the partial fulfillment of requirement for the award of the degree of

DOCTOR OF PHILOSOPHY

By

Shivani Jain

(Reg. No: 901612016)

Under the supervision of

Dr. Manoj K. Sharma
Professor

Dr. Raj Kumar
Associate Professor

THAPAR INSTITUTE
OF ENGINEERING & TECHNOLOGY
(Deemed to be University)

SCHOOL OF PHYSICS AND MATERIALS SCIENCE

THAPAR INSTITUTE OF ENGINEERING AND TECHNOLOGY, PATIALA - 147004

PUNJAB, INDIA

SEPTEMBER 2022

Dedicated to My Mother,
My Strongest Support.

THESIS CERTIFICATE

This is to certify that the thesis titled "**A STUDY OF EXOTIC COMPOUND NUCLEAR SYSTEMS AND SUBSEQUENT FRAGMENT EMISSION USING SKYRME ENERGY DENSITY FORMALISM**", submitted by **Ms. Shivani Jain**, for the fulfillment of the requirements for the award of Degree of Doctor of Philosophy in the School of Physics and Materials Science, Thapar Institute of Engineering and Technology, Patiala, is a record of the candidate's own work carried out by her under my supervision. The matter presented in this thesis has not been submitted in part or full for the award of any degree in any other university or institute.

Supervisors

MSharma

Manoj Kumar Sharma
Professor
School of Physics Materials Science
TIET, Patiala - 147004
Punjab, INDIA

Date: 20/09/2022

Place: Patiala

Raj Kumar

Raj Kumar
Associate Professor
School of Physics Materials Science
TIET, Patiala - 147004
Punjab, INDIA

Date: 20/09/2022

Place: Patiala

ACKNOWLEDGEMENTS

Thank you God *for all your blessings to me. For the strength you give me each day and for all the people around me who make life more meaningful. At this moment, I am writing these words in the completion of this thesis. So, I hereby express my gratitude for some very important people through these small letters.*

To

Respected Dr. Manoj K. Sharma *and* ***Dr. Raj Kumar***

*It is very difficult to "***Thank both of you***" in just few words. But still, I want to share few things which inspired and helped me a lot to deal with the situations. Both of you always teach me "***How to make things better and better, by giving The Best out of my improved version***". This has given me encouragement to work hard, stay determined and focused towards my work. Also, you never give up on your students, and that is the best thing I see in you and aspired to be like that. With your teachings, whatever I achieved in my past, have in the present and will get in future are solely dedicated to both of you. I am always very much thankful to you for '***Everything***'. I really feel blessed and fortunate to be your student.*

Doctoral Committee members*,* ***SPMS faculty members*** *and* ***Dean RSP***

I would like to thank my doctoral committee, Dr. Alka Upadhyay, Dr. Sunil Devi and Dr. A. K. Lal for their valuable suggestions and constructive ideas during the progress report held every six months. My special thanks goes to Prof. Kulvir Singh, Head, School of Physics and Materials Science, TIET, Patiala for providing all the necessary facilities in the department. I greatly appreciate the help and co-operation of all the faculty members and staff of the SPMS for their help and kind support. My sincere thanks also to Prof. Rafat Siddique, Dean, Research and Sponsored Projects, TIET, Patiala for providing the grants to attend the conferences and necessary resources to accomplish my research work.

Dear lab-mates *and* ***friends***

"**A friend is someone who helps you up when you are down, and if they can't, they lay down beside you and listen**". *There is nothing more I can say. These words* *are expressing all my feelings and* “**Thank you all for everything**”.

Here, I am mentioning their names:

Dr. Neha Grover, Dr. Amandeep Kaur, Dr. Kanishka Sharma, Dr. Gurjit Kaur, Dr. Rajni Mittal, Dr. Gudween Sawhney, Dr. Aman Deep Kaur, Dr. Ishita Sharma, Dr. Deepika Jain, Dr. Kirandeep Sandhu, Dr. Gurvinder Kaur, Dr. Sangeeta, Dr. Amanpreet Chhatwal, Dr. Navjot Kaur, Kaushlendra Pandey, Raveena, Dr. Santhosh K. Mahadevan, Kaveri, Aman, Shivani Punj, Trisha, Neeraj Sharma, Shuaib, Kundan Kumar, Nishu, Shubhpreet.

And there are some more special names, who are my buddies:

Vishal Parmar, Nitin Sharma, Shilpa Rana, Harshit Sharma, Ashutosh Kaushik and Chahat Jindal - Thank you for all the madness we did together.

My lovely family:

Parents, Sumit Jain (brother), Sapna Jain (sister), Bharat Jain (brother-in-law), Navya Jain (niece), Pulkit Jain (nephew) and Hitika (niece), who have laughed with me, cried with me, helped me when there was a need, and proven to me that there are indeed flowers to be found in a world that at times seems to be full of weeds, I say thank you, I love you, and you mean everything to me.

Thanks to one and all.

Shivani Jain

ABSTRACT

In this thesis, the formation and subsequent decay mechanisms of compound nuclear systems induced via heavy-ion reactions have been studied at the low-energy regime. For this analysis, the nucleus-nucleus interaction potential derived using the semiclassical SEDF approach is considered as a tool to estimate the fusion barrier characteristics, which are used as input to calculate the fusion cross-sections witih the Wong formula (and its extended version) for incident energies lying across the Coulomb barrier. Additionally, the influence of different density distribution functions and approximations employed within the SEDF approach has been studied in view of the fusion barrier characteristics and the fusion cross-sections. For comparative analysis, the phenomenological potentials, like Prox77, Pox88 and Woods-Saxon etc., are considered and analyzed the corresponding influence in nuclear fusion dynamics. Further, to study the subsequent decay mechanisms of the formed compound nucleus (CN), the mass and charge distributions of excited CN have been examined within the framework of collective clusterization approach of Dynamical Cluster-decay Model (DCM). The model based on the Quantum Mechanical Fragmentation Theory (QMFT). In the fusion-fission dynamics of heavy-ion induced reactions, the role of deformations (to octupole β_3 deformation) and corresponding optimum orientations has also been investigated. In view of above, the present thesis is divided into eight chapters, which are briefly described as:

Chapter 1 begins with the basic understandings related to the subatomic particles and their interactions with the other nuclei, taken place at the low-energy regime (beam energy $\leq$ 15 MeV/nucleon). In the present thesis to study the nucleus-nucleus interactions, the heavy-ion (with mass and charge numbers $\geq$ to that of $^4_2$He nucleus) reactions are taken into consideration. Later, the theoretical models developed to study the heavy-ion collisions are discussed. Also, a description regarding the relevance of deformations and orientations degrees of freedom in nuclear fusion-fission dynamics is discussed. The motivation of this work is to study the formation and subsequent decay mechanisms of compound nuclear systems using Skyrme Energy Density Formalism and phenomenological model.

In **Chapter 2**, the formalisms used to derive the nucleus-nucleus interaction potential on the basis of the semiclassical SEDF approach and the phenomenological model are discussed. The mathematical formulations defining the repulsive Coulomb and centrifugal potentials are discussed for the spherical-spherical, spherical-deformed and deformed-deformed pairs of colliding nuclear partners. Further, the fusion barrier characteristics (barrier position R_B, barrier height V_B and barrier curvature $\hbar\omega_B$) extracted from the total interaction potential, obtained by combining nuclear, Coulomb and centrifugal potentials, are used as input terms to calculate the fusion cross-sections. To estimate the fusion cross-sections as a function of center of mass energies, the Wong formula and its extended version are employed. In order to study the mass and charge distribution of compound nuclear systems, the expressions for the fragmentation potential and preformation probability obtained within the collective clusterization approach are illustrated. The Appendixes A and B are given to detail the curvature radii of deformed surfaces. In the following Chapters, the results and calculations are discussed.

In **Chapter 3**, different density approximations such as frozen, sudden and modified sudden are employed within the Skyrme Energy Density Formalism and compared with the phenomenological relaxed-density approach for Ni-based reactions. These approximations give different ways in which individual densities of projectile and target can be added for obtaining compound nucleus density. On the basis of this, the corresponding influence of above mentioned density approximations has been analyzed in view of the fusion barrier characteristics and subsequently on the fusion cross-sections (σ_{fus}) for ^{18}O, ^{40}Ca, ^{58}Ni and ^{132}Sn+^{58}Ni reactions. The fusion cross-sections obtained using extended ℓ-summed Wong model are compared with the available experimental data across the Coulomb barrier energies for the ^{58}Ni-based reactions.

In **Chapter 4**, the role of three-parameter Fermi (3pF) and three-parameter Gaussian (3pG) density functions in the fusion dynamics has been explored in comparison to the two-parameter Fermi (2pF) employed within the semiclassical SEDF approach. For the case of the three-parameterized density functions (3pF and 3pG), an additional parameter 'w' influences the tail and nearby region, and hence the barrier characteristics get modified accordingly. In view of this, the role of 2pF, 3pF and 3pG density functions has been analyzed by calculating the fusion barrier height V_B (and barrier position R_B) for a variety of nuclear reactions with the mass-asymmetry spread from symmetric to asymmetric reaction partners, and the results are compared with the available experimental data. In addition to this, the fusion cross-sections for ^{58}Ni-based reactions are calculated using extended ℓ-summed Wong model and the collective effect of V_B, R_B and $\hbar\omega_B$ (barrier height, position and curvature respectively) for the use of above mentioned density distributions has been examined. The ℓ_{max}-values have been obtained using the sharp cut-off model for above barrier energies and extrapolated for below barrier energies.

In **Chapter 5**, the relevance of deformation and orientation degrees of freedom has been explored for the synthesis of heavy and superheavy nuclei. In view of this, the octupole deformation (β_3) which distorts the spherically symmetric or quadrupole deformed (β_2) nuclei into a pear shape has been taken into account. The influence of octupole deformed nuclei on the optimum (or uniquely fixed) orientations obtained for the 'elongated' and 'compact' fusion configurations of these nuclei has been analysed and discussed in comparison to that of the quadrupole deformed nuclei. Also, to investigate the effect of β_3-deformation in reference to that of β_2, a systematic analysis has been done for the the soft-pear shape nuclei with small β_3-deformations and rigid-pear shape nuclei with strong β_3-deformation. Additionally, the '+' and '−' sign effects of β_3-deformation have been discussed. The analysis done in this chapter is exercised using the SEDF and phenomenological based potentials.

As an extension of above analysis, **Chapter 6** is devoted to investigate the significance of deformation and associated optimum/uniquely fixed orientations for the formation of compound nuclei via cold and hot fusion reactions. The proposed set of optimum orientations corresponding to β_3-deformed nuclei, discussed in the earlier chapter, is utilized to understand the respective influence on the fusion barrier characteristics and fusion cross-sections for ^{16}O and ^{48}Ca-induced reactions. In these reactions, β_3-deformed nuclei are taken as targets belonging to different mass-regions of the Periodic Table. The above analysis is exercised for around 200 spherical-plus-β_3 deformed pairs of colliding nuclear partners. The results are compared with the available experimental data for ^{16}O+^{150}Sm (β_{22} = 0.205, β_{32} = -0.055) reaction.

In **Chapter 7**, the disintegration of light and heavy-mass isotopes of Thorium i.e. ^{222,224,226,228,230}Th* compound nucleus have been discussed using the SEDF and phenomenological potentials within the collective clusterization approach of QMFT. In this analysis, the significance of octupole deformations and corresponding cold optimum orientations has been explored in terms of the fragmentation potential and preformation probability. The obtained results are discussed in comparison with the quadrupole deformation of decaying fragments. Additionally, the mass- and charge-distributions of considered isotopes of Th are compared with the experimentally obtained yield profiles.

At the end, in **Summary** chapter, all the results discussed in the above chapters on the basis of Skyrme Energy Density Formalism, in comparison with the phenomenological models, are summarized. The future scope of the work done in the present thesis is discussed briefly.

Contents

List of Tables

List of Figures

THESIS BASED PUBLICATIONS

In International Journals

1. "Effect of different nuclear density approximations on fusion dynamics within Skyrme Energy Density Formalism"

   Shivani Jain, Raj Kumar and Manoj K. Sharma

   Eur. Phys. J. A, **54**, 203 (2018)

   Impact Factor: *3.043*

2. "Analysis of the barrier characteristics and related fusion properties using 2pF, 3pF and 3pG density function"

   Shivani Jain, Manoj K. Sharma and Raj Kumar

   Nucl. Phys. A **997**, 121699 (2020)

   Impact Factor: *1.659*

3. "Optimum orientations for octupole deformed nuclei in fusion configurations"

   Shivani Jain, Manoj K. Sharma and Raj Kumar

   Phys. Rev. C **101**, 051601(R) (2020)

   Impact Factor: *3.296*

4. "Fusion of spherical-octupole pairs of colliding nuclei for compact and elongated configurations"

   Shivani Jain, Manoj K. Sharma and Raj Kumar

   Chin. Phys. C Vol. **46**, No. 1, 014102 (2022)

   Impact Factor: *2.145*

5. "Investigation of octupole deformed fragments decaying from even-even isotopes of $^{222-230}Th^{*}$"

   Shivani Jain, Raj Kumar, S. K. Patra and Manoj K. Sharma

   Phys. Rev. C **105**, 034605 (2022)

   Impact Factor: *3.296*

In National and International Conferences/Symposiums

1. "Fusion cross-sections for ^{6}Li+^{90}Zr reaction studied using Skyrme Energy Density Formalism"

   Shivani Jain, Gurvinder Kaur and Manoj K. Sharma

   Proceeding of the DAE-BRNS Symp. on Nucl. Phys. **61** (2016)

2. "Comparative analysis of various density approximations within the Energy Density Formalism"

   Shivani Jain, Raj Kumar and Manoj K. Sharma

   Proceeding of the DAE-BRNS Symp. on Nucl. Phys. **62** (2017)

3. "Relative relevance of Skyrme forces in reference to barrier characteristics of deformed nuclei"

   Shivani Jain, Vishal Parmar, Raj Kumar and Manoj K. Sharma

   Proceeding of the DAE-BRNS Symp. on Nucl. Phys. **63** (2018)

4. "Study of fusion hindrance via cold configuration within SIII Skyrme force"

   Shivani Jain, Raj Kumar and Manoj K. Sharma

   Proceeding of the DAE-BRNS Symp. on Nucl. Phys. **64** (2019).

5. "Impact of octupole deformation on the fusion barrier of ^{48}Ca+^{232,280}Rn reactions"

   Shivani Jain, Raj Kumar and Manoj K. Sharma

   Centenary Celebration on Nuclear Structure and Nuclear Reaction, page no. 26, March 2 – 4 (2020) Aligarh Muslim University, Aligarh

6. "Impact of pear-shape nuclei on fusion barrier and synthesis of new elements"

   Shivani Jain, Raj Kumar and Manoj K. Sharma

   First International conference on Technologies for smart green connected society (2021) – ICTSGS SCOPUS Conference

7. "Mass and charge dispersion analysis of ^{224}Th* using SIII and GSkI Skyrme foces"

   Shivani Jain, Raj Kumar and Manoj K. Sharma

   Proceedings of DAE-BRNS Symposium on Nucl. Phys. **65** (2021)

8. "Impact of hexadecapole deformed targets in fusion dynamics of ^{16}O-induced reactions"

   Harshit Sharma, **Shivani Jain**, Amritpal, Raj Kumar and Manoj K. Sharma

Nuclear Physics Conference on Low Energy Nuclear Reaction Dynamics, March 7 – 9 (2022), Aligarh Muslim University, Aligarh

9. "Fusion-fission dynamics of compound nuclear systems formed via pear-shape deformed targets"
   Shivani Jain, Raj Kumar and Manoj K. Sharma
   25^{th} Punjab Science Congress-2022 on Future Endeavours of Science and Technology for sustainable growth February 7 – 9, (2022), Sri Guru Teg Bahadur Khalsa College, Sri Anandpur Sahib, Punjab

ABBREVIATIONS

CN	Compound Nucleus
SEDF	Skyrme Energy Density Formalism
EDF	Energy Density Formalism
HF	Hartree-Fock
DCM	Dynamical Cluster-decay Model
QMFT	Quantum Mechanical Fragmentation Theory
TKE	Total Kinetic Energy
ETF	Extended Thomas-Fermi
2pF	Two-parameter Fermi
3pF	Three-parameter Fermi
3pG	Three-parameter Gaussian
ER	Evaporation Residue
LPs	Light Particles
IMF	Intermediate Mass Fragment
HMF	Heavy Mass Fragment
SHE	Super Heavy Element
P-T	Projectile-Target

NOTATIONS

A	Mass Number of nucleus
Z	Charge Number of nucleus
N	Neutron Number of nucleus
R_0	Half-density Radius
ρ	Nuclear-density
ρ_0	Central density
a	Surface thickness factor
b	Surface diffuseness factor
w	Wine-bottle parameter
T	Temperature
$\bar{R}$	Radius of curvature
α	Angle of rotation of radius vector
β	Deformation parameter
θ	Orientation of symmetry axis
ϕ	Azimuthal angle
$\triangle R$	Neck-length parameter
$Y_\lambda^{(0)}$	Spherical-harmonic function of axial-symmetric shapes
s_0	Minimum separation distance
η_A	Mass-asymmetry parameter
η_Z	Charge-asymmetry parameter
E^*_{CN}	Excitation energy of excited Compound Nucleus
$E_{c.m.}$	Center of mass energy
Q	Q-value of entrance-channel
Q_{eff}	Effective Q-value
ℓ	Angular momentum quantum number
μ	Reduced mass
I	Moment of inertia
R	Separation distance between two nuclei
V_B	Barrier height
R_B	Barrier position
$\hbar\omega_B$	Barrier curvature
V_0	Step potential
R_a, R_b	Classical tunneling points
σ_{fus}	Fusion cross-section
σ_{fis}	Fission cross-section
σ_{Expt}	Experimental cross-section

Chapter 1

INTRODUCTION

1.1 An overview

"*Universe - An opportunity to understand the origin, purpose and destruction of a life.*"

In the space-time frame of Universe, all the belongings of this cosmos whether in the form of matter or energy were initially confined within an infinitely dense and hot point, which later exploded. This Big Bang went through a superfast cosmic inflation, powered by small vibrations of quantum fluctuations and eventually led to form hot soups of tiniest particles (leptons and quarks). As the temperature dropped down, the neutrons and protons comprised of quarks came into existence. But, the space was still very hot preventing the nucleons (neutrons/protons) to hold together and form a positively charged nucleus. After 300 thousand years of Big Bang explosion, the recombination of nucleons occurred and formed Hydrogen and Helium nuclei of positive charges. These ionized ions got surrounded by the negatively charged electrons moving in their orbits to form a neutral atom. At this moment, the transition of electrons between different orbits allowed the emission of photons, enabling the light to travel freely in the dark space. In the era of recombination, the cosmos cooled down to an extent that, different kinds of fundamental forces came into existence and started to play significant role for the interactions among the atomic and subatomic particles. Under the influence of such interactions, the expansion of Universe continues even at the age of billions of years and possesses numerous galaxies due to the coalition of Hydrogen and Helium gases.

The galaxies of this macrocosm are filled with numerous stars, surrounded by the planetary systems. In the second largest galaxy the Milky Way, Earth is the only astronomical planet with the possibility of life to evolve and thrive. In Earth's quarter part of land and rest area covered with water, one can see diversity in the nature and its belongings, e.g. rock materials, planets/animals (of land and water), woods, human, etc. In other words, the

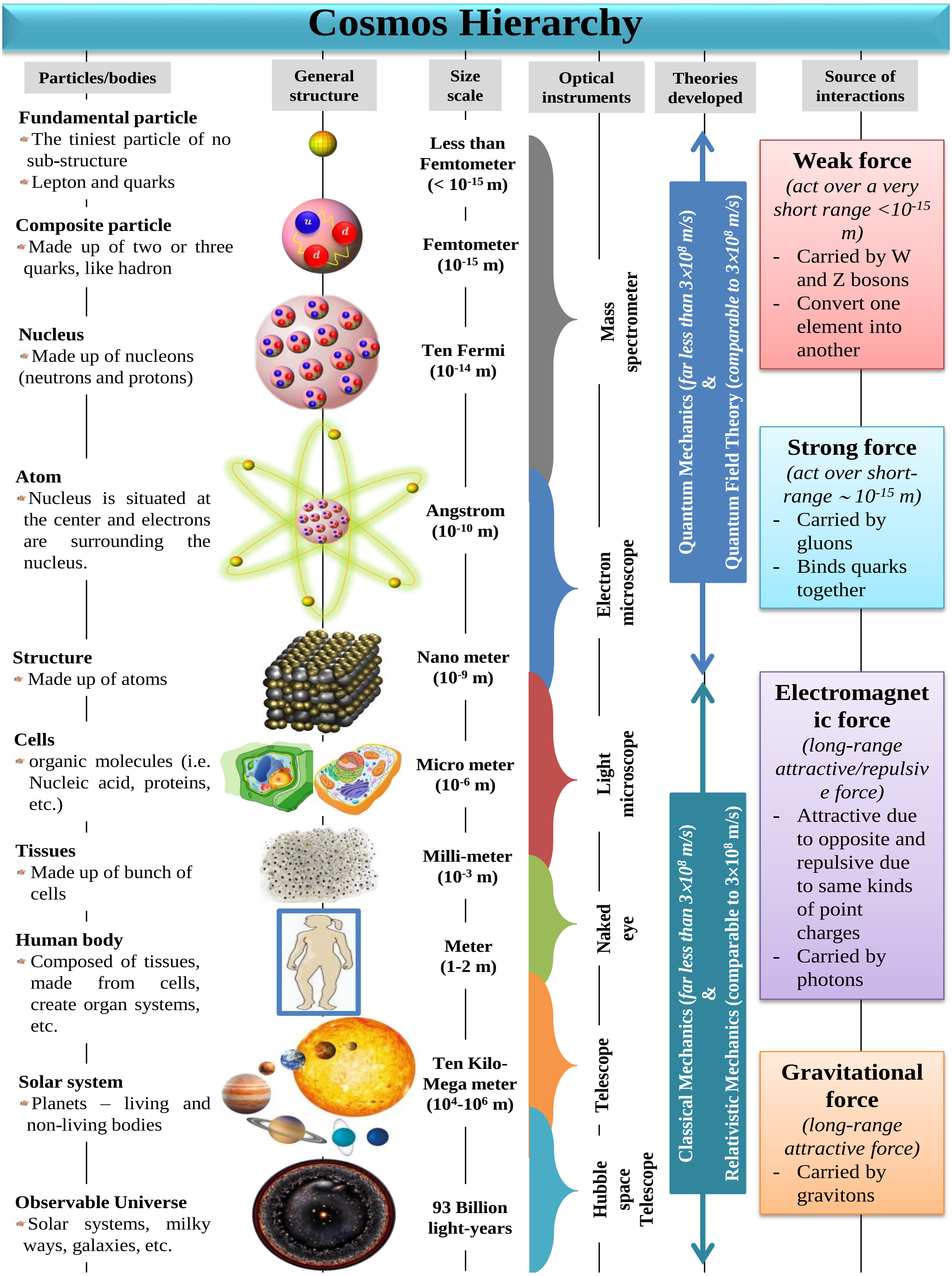

Figure 1.1: The cosmos hierarchy and schematic picture of particles/bodies of different sizes, corresponding optical instruments and source of interactions among different bodies.

diversity explains the behavior of subatomic/elementary particles at different scale of time, energy and distance. Since we humans are not ubiquitous like the elementary particles of no sub-structure, we always stay curious and desirous to understand the natural phenomena. With this basic nature, the man had extracted different tools and prospects from the natural resources to make life easy in many aspects. In the present time, the innovations and technologies provided to this world have been advanced so much that a person sitting in his/her room can easily have a glimpse of any parts of the globe, stars, celestial planets, etc. So the things discovered, philosophized and written in the manuscripts related to the behavior of small-sized particles and their applications in the physical world are discussed mainly through the scientific language developed on the basis of theoretical/experimental analysis and mathematical formalisms. The study of such phenomena is so vast that it took many years and significant efforts to reach at logical statements and scientific facts. With these enormous efforts, nowadays, it has become easy to visualize and compare the bodies of different sizes, i.e. from 10^{-18} m to billion light-years, in a single frame. In Fig. 1.1, an attempt has been made to demonstrate the cosmos hierarchy on a brief note.

The hierarchy helps in understanding how the subatomic particles are involved in the formation of other bodies of relatively bigger sizes through the fundamental forces, which are categorized as: weak, strong, electromagnetic and gravitational force. For the interactions taking place lower than the femtoscale (10^{-15} m), the weak forces have been found to play their role in the conversion of an elementary particle into another kind. Further at few Fermi scale $\sim 10^{-15}$ m, the subatomic particle interactions occur with the effect of the short-range attractive strong force or its residual part. Beside this, the +/- charges and orbital/spin motions evoke the long-range electromagnetic force showing attractive and repulsive behavior for the like and unlike charged particles, respectively. Due to the presence of above said strong, weak and electromagnetic fundamental forces, the particles feel both the repulsion and attraction towards the other ones existing in their surroundings, and subsequently construct bodies of relatively bigger sizes at a point of balance between different forces. As one moves from smaller sized ($<10^{-6}$ m) particles towards the relatively bigger sized bodies (see Fig. 1.1), the gravitational force can be experienced, even in our daily lives. The particles/objects of different sizes residing in this cosmos are always in motion, with the speed either comparable or very less than the speed of light 'c', i.e. 3×10^{8} metre per second. Note that, the bodies moving with the speed comparable to c are dealt with the relativistic approach. Different properties of the macro and microscopic particles/objects shown in Fig. 1.1 have been understood under the two cornerstones of Physics, i.e. the Classical and Quantum Mechanical theories, respectively. The systems which are manifested under the classical approach possess certain properties and distinguishable behavior under different circumstances. On the other side, the corpuscles and their interactions with the other subatomic particles which are very difficult to observe are discussed on the basis of probability under the shed of Quantum Mechanical (QM) laws.

Quantum Physics based on the probabilistic analysis has opened up many fields, discussing about the problems related to the matter in solid state, molecules, atoms, nuclei, subatomic particles and their related phenomena. Specifically, in the field of Nuclear Physics, the concept of quantum tunneling effect had been originated with the discovery of radioactive decay by Henri Becquerel in 1896 [1]. In contrast to the laws of Classical Mechanics, the quantum tunneling effect illustrated the possibility of crossing the potential barrier by the nucleus or nucleons possessed with sufficient kinetic energy. On the basis of this conceptual idea, the researchers had provided numerous mathematical formalism based on QM to study the nucleus, its structural properties, and variety of nuclear reaction mechanisms, like nuclear fusion, fission, elastic and inelastic scattering, direct reactions, etc. which take place at different scale of energy. All these studies related to the nucleus and its constituent particles are very difficult and complicated to compile in a single frame. Therefore, the models and theories developed to comprehend the nuclear structure, reactions dynamics, finite/infinite nuclear systems, nucleo-synthesis, etc. are categorized as specific fields of Nuclear Physics. In the present thesis, the main motive is to study the nucleus-nucleus interactions, taking place at the low-energy regime, and understand the role of different nuclear properties in the reaction dynamics. The relevant discussion is provided in the following section.

1.2 Nucleus-nucleus interaction at low-energy

To study nucleus-nucleus interaction, the famous scientist Ernest Rutherford in 1917 had made an attempt to empathize the nucleus and its interaction with another one via a transmutation process. He had directed the beam of alpha-particles (or Helium-4 nuclei) on Nitrogen-14, which in turn, scattered Oxygen-17 and Hydrogen nuclei [2]. A successful ex-

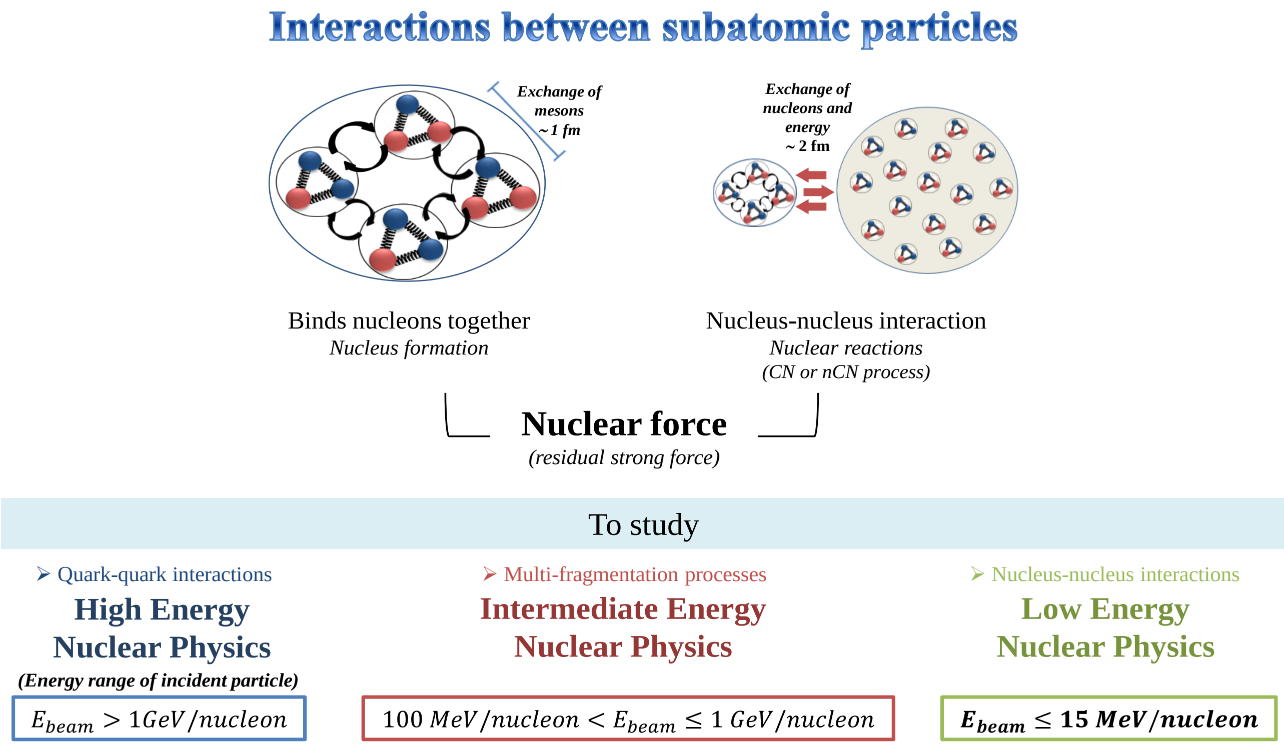

Figure 1.2: A schematic diagram for Nuclear force of interactions between subatomic particles. The energy ranges provided are categorized to study different interactions between subatomic particles at the scale of few fermi.

periment of artificial nuclear reaction had encouraged the researchers to work on different combinations of nuclei, in order to comprehend various nuclear properties and discover new elements of the Periodic Table. With the course of time, it has been analyzed that, the mass and charge numbers of nuclei are the basic information in determining the nuclear radius, density, volume, binding energy, angular/spin momenta, etc. On the basis of these static properties, the influence of attractive/repulsive forces has been explored. Likewise, in the collision of two positively charged nuclei, the Coulomb force shows repulsive behavior. Due to the angular momenta of colliding nuclei acting in the outward direction, the centrifugal force comes into picture and shows repulsion between them. The existence of these repulsive forces would never allow the interaction and binding between two nuclei. Here, a simple question arises that which force binds the two or more nucleons/nuclei together and what are its limitations? To answer this question, the researchers named this force as strong force, which is known to be "***the strongest force***" amongst all the fundamental forces. It lasts over a very small distance of about few quadrillionth of a meter. That means, it has saturation property and comes into existence for those interactions, which take place at the scale of few fermi.

For the interactions between nucleons taking place at a distance of about 1 fm, the nuclear force comes into picture, which in result binds the nucleons and forms a nucleus comprised of neutrons and protons. The information regarding this force was initially tested for the bound state of a nucleus, which is possible due to exchange of meson (or muon) particles between the nucleons. Therefore, the meson particles which had been predicted by Hideki Yukawa in 1935 [3] and later discovered by Carl Anderson and his student Seth Neddermeyer in 1936 [4] are known to be the nuclear force carriers. The exchange of mesons, which takes place within a very short-range of distance ($\approx 10^{-15}$ m), illustrates the saturation property of nuclear force. Also, the physicists had analyzed the influence of nuclear force between two nuclei, when they are in the close proximity region of about 2 fm. Such interactions may lead to different nuclear processes, like Compound Nuclear (CN) reaction and non-Compound Nuclear (nCN) reactions [5–10]. For convenience, a schematic diagram for the above said interactions related to the strong and residual strong force (or nuclear force) is shown in Fig. 1.2. In studying the reaction dynamics of subatomic particles, the beam energy (E_{beam}) of incident particles is classified as: (1) $E_{beam} > 1$ GeV/nucleon, (2) $100 < E_{beam} \leq 1$ GeV/nucleon and (3) $E_{beam} \leq 15$ MeV/nucleon, also shown in Fig. 1.2. On the basis of these energy regimes in the field of Nuclear Physics, the related research has been done differently and categorized as High Energy, Intermediate Energy and Low Energy Nuclear Physics, respectively. In the present thesis, the main focus is to discuss about the nucleus-nucleus interactions which are leading towards the CN reactions, occurring in the low-energy regime.

With the advent of nuclear reaction, the researchers have considered this process as a probe to understand the role of nuclear forces for a variety of projectile-target (P-T) combinations. Important to mention that, in the present work, the heavy-ion nuclei are taken as the beam of incident particles and fixed target nucleus to study CN reactions. The interaction between selected choices of P-T combinations may form an intermediate nuclear entity, known as compound nucleus and the process is named as Compound Nuclear reaction. In CN process, the projectile nucleus should possess sufficient kinetic energy and share its nucleons and energy with the target in the propinquity region. In 1936 [11], N. Bohr proposed the compound nuclear theory of nuclear reactions. He assumed and later evidenced through experiments that, the formation of a compound nucleus is considered as an intermediate stage of two-step process:

1. Projectile nucleus + target nucleus $\longrightarrow$ Compound nucleus*

2. Compound nucleus* $\longrightarrow$ Product nucleus + outgoing particle.

The formed compound nucleus possesses a high value of angular momentum and excitation energy. Transferring of nucleons and energy among two nuclei takes a very small time (of about 10^{-22} sec), as compared to the life ($\approx 10^{-16}$ sec) of compound nucleus in its excited states. For an illustration, if the incident particle travels with the speed of about 10^7 m/s, and for sharing the nucleons, the particle has to reach into the target nucleus whose diameter is of the order of 10^{-14} m, therefore the reaction time taken for the amalgamation of incident projectile and target nuclei will be of the order of 10^{-21} sec (i.e. diameter of target/speed of incident projectile). Since the CN life time scale in its excited state is much larger than the reaction time, one can figure out the formation possibility of a new nuclear entity through the heavy-ion induced reactions. The above idea had inspired the physicists to analyze the fusion possibility between different choices of colliding nuclear partners and later the disintegration of formed nucleus into binary fragments. This way, the researchers have put their efforts in synthesizing the new isotopes, lying either nearer or far away from the β-stability line, at the low energy regime.
In earlier times, it was understood that, the fusion process was more preferable among the projectile-target of light-mass nuclei (lighter than or equivalent to Iron and Nickel elements), because the existence of nuclear force between small sized nuclei overcomes the Coulomb force. On the other hand, in the heavier mass nuclei, there are large number of protons which cause significant effect of Coulomb repulsion between them, and subsequently such nuclei become more fissile. Nowadays, with the help of highly-advanced technologies, the artificial production of elements in different mass-region has become possible. In other words, one is able to determine the fusion cross-sections even at the scale of pico-barn (10^{-12} b) over a wide range of beam or center of mass energies [12]. Henceforth, a variety of formed CN in an excited state de-excite to the stable state either by emitting similar or different fragments. The disintegration of excited CN occurs with the effect of temperature (or excitation energy), rotational motion, nuclear shape configuration (deformation and orientation) etc. These intrinsic nuclear properties give a comprehensive knowledge for the occurrence of different nuclear decay mechanisms, viz. light-, intermediate-, heavy-mass fragment emission and fission process. These competing phenomena followed by the CN

process are also referred as different scenarios for obtaining new elements, which are further harvested for the fundamental understanding related to various nuclear properties and the associated applications in diverse areas such as radiation, astro physics, medical and health sector, etc. To study the heavy-ion induced compound nuclear reactions at the low-energy regime, the theoreticians have developed numerous models and theories, and found the total interaction potential as the basic term to have a comprehensive knowledge over the reaction dynamics and associated nuclear properties.

1.3 Theoretical models to study heavy-ion collisions

The term total interaction potential is considered as a basic ingredient and, it is comprised of the Coulomb potential (V_C), centrifugal potential (V_ℓ) and nuclear potential (V_N). For convenience, a schematic diagram which shows the behavior of total and contributing potentials with the variation of separation distance (R) between two nuclei, acting along the collision axis, is shown in Fig. 1.3. One may note from this figure that, the repulsive profiles of Coulomb and centrifugal potentials with respect to R are well established for varieties of projectile-target combinations. Important to mention that, there can be relative change in the magnitude of V_C and V_ℓ. On the other hand, due to uncertain nature of interactions involved within the colliding nuclei, the theoreticians have given different relations of nuclear potential to define various nuclear properties. In 1930s, H. Yukawa had given a potential, which is labeled after his name, and its exponentially decaying profile generally used to study the nucleon-nucleon interactions [3]. Later, in the mid of 1950s, a first semi-empirical relation of nuclear potential had been developed by R. D. Woods and D. S. Saxon [13]. This Woods-Saxon nuclear potential gives a depth at the short-range distance, then monotonically increase and becomes flat at larger value of separation distance. Besides, it is believed that, for the formation of a compound nuclear system, the projectile nucleus should get captured by the target forming intermediate equilibrated CN state. On the basis of this, the theoreticians had defined the nuclear potential of gaussian distribution representing bell curve in the inverted form, or one can say gaussian potential well which represents the deep pocket of nuclear potential, for convenience see the dash-dot line of nuclear potential in Fig. 1.3. Analogous to the gaussian potential, various approaches had been given like

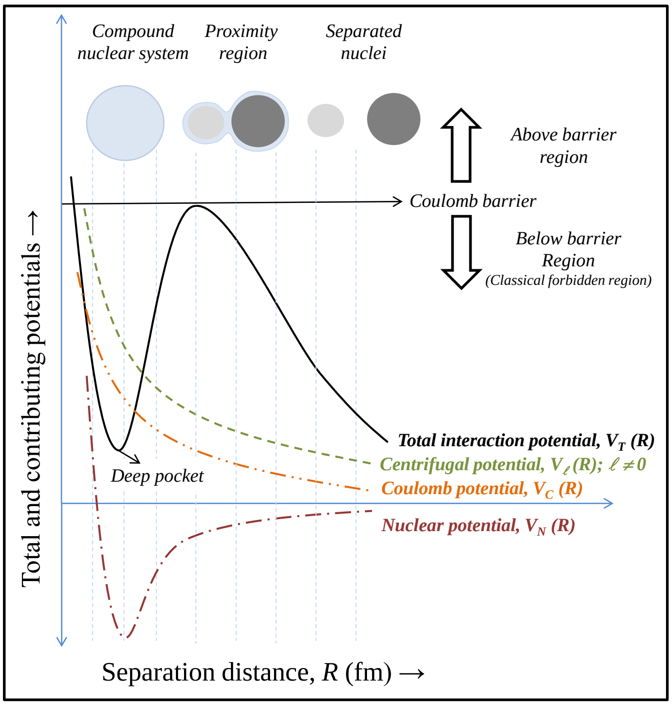

Figure 1.3: A schematic diagram of repulsive potential (Coulomb potential V_C, centrifugal potential V_ℓ), attractive potential (nuclear potential V_N) and total interaction potential, as a function of separation distance R (fm).

Energy Density Formalism (EDF) [14–21], double-folding method [22, 23] and phenomenological models [24–28], etc. In the present work, the nucleus-nucleus interaction potential is derived using the EDF approach. For comparative analysis, the nuclear potentials obtained from the phenomenological approaches are also employed. A brief description of EDF based nuclear potential is given in the subsection below.

1.3.1 Skyrme Energy Density Formalism

In 1965, Kohn and his co-workers had developed the Energy Density Formalism [14–21] and according to this theory, the total energy of fermions can be defined as a function of nucleon density [14]. This approach has turned the complicated calculations into the simpler ones and many authors were able to define several nuclear properties. Later, based on EDF approach, D. Vautherin and D. M. Brink had derived the nuclear potential in terms of the nuclear binding energy with the use of Hartree-Fock (HF) method for the spherical [29] as well as deformed cases [30]. These HF based calculations were carried out using the Skyrme force parameters, which reproduce the experimental binding energies and nuclear radii for closed shell nuclei. The concept of Skyrme force, based on some parameters, had been introduced by the British physicist T. H. R. Skyrme [31–34]. With the advent of Skyrme force parameters, the researchers had employed these parameters within the energy density formalism as algebraic function of the nucleon density ρ, kinetic energy density τ and spin-orbit density $\vec{J}$ functions [29, 30]. Later on, in order to derive the nuclear interaction potential between two colliding nuclei, Brink and Stancu had stated in Ref. [35] that, the difference in the expectation energies of interacting nuclei and infinitely separated nuclei defines the nucleus-nucleus interaction potential. Thus, in the Skyrme Energy Density Formalism (SEDF), the Hamiltonian used to derive the potential is basically a function of ρ, τ and $\vec{J}$ terms. In the earlier studies [29, 36–39], these terms had been obtained through the microscopic approaches, e.g. Hartree-Fock approximations [29]. On the basis of HF method, the nuclear density, kinetic energy density and spin-orbit density terms were obtained via the Slater determinant [39]. Such approaches are good in studying the nuclear structure properties of a finite nuclear system. However, while dealing with the nucleus-nucleus interactions or heavy-ion collisions, the calculations done using the microscopic approach become complicated and require lots of computational efforts. To overcome this difficulty, the researchers had opted the semiclassical approach to work on the heavy-ion collisions. According to the semiclassical approach, one can obtain the nuclear density profile on the basis of electron-scattering experiment data [40] and kinetic-energy and spin-orbit density terms through the extended Thomas-Fermi approach (ETF) [41–44], to be discussed in the following paragraphs.

The density of a nucleus defines the mass distributed over a small volume (fm^3). In other words, the nucleus with the size of approximately few fm residing at the center of an atom possesses very high density of about 10^{17} kg/m^3. This density remains constant for a while and decays abruptly at the edge of the nucleus, as shown in Fig. 1.4; that means the nucleus is not a hard core entity. Basically, the distribution of nucleons within the nucleus helps in defining the central density (ρ_0) and tail region of the nuclear density. The researchers have suggested numerous mathematical approaches [40, 45–50], which are addressed in reference to the experimental results, for defining the density distribution normalized to the total number of nucleons residing within the nucleus. Initially, in 1929, N. F. Mott had illus-

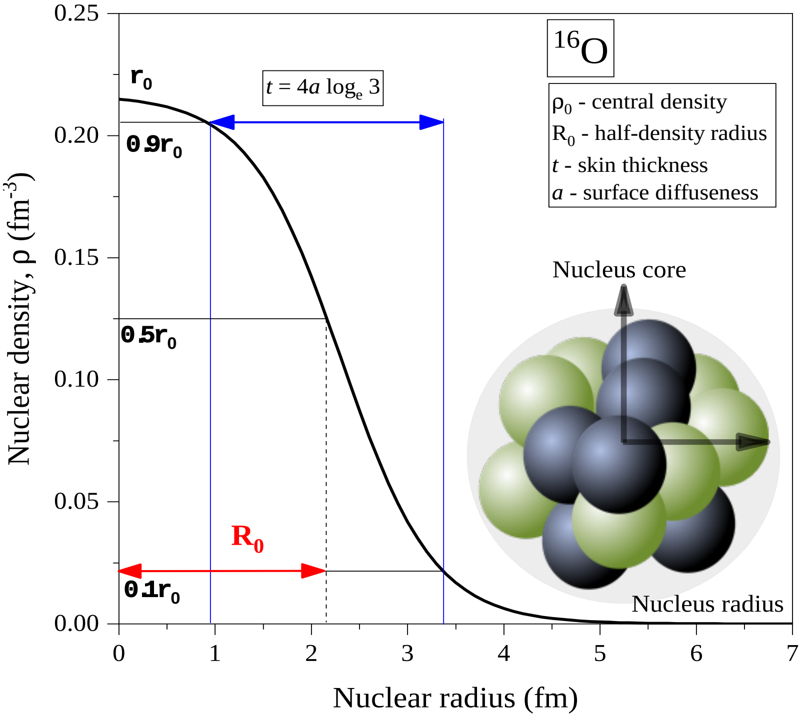

Figure 1.4: The nuclear density distribution ρ (fm^{-3}) shown from center to the edge of a nucleus (e.g. ^{16}O) illustrates the central density 'ρ_0', half-density radius 'R_0', skin thickness 't' and surface diffuseness 'a' parameters.

trated about the nuclear size through the electron scattering from the atomic nucleus [51,52]. Later, the information regarding the finite size were treated under the Born approximation given by Guth [53] and individually by Rose in 1948 [54]. Thereafter, in 1950 [55], L. R. B. Elton had provided the exact calculations of finite size, which was extended by Hofstadter and Stanford [56, 57]. Besides, the experimentalists Lyman, Hanson and Scott observed the finite size of light-mass nuclei effects at Illinois in 1955 [58]. However, for medium and heavy-mass nuclei, the concept of Born approximation was not enough [59]. Therefore, the smoothed variation of Fermi type function of two-parameter was introduced for defining the nuclear size and related terms, e.g. surface thickness and diffuseness factors, through a radial function density ($\rho(r)$) term. Also one can see a typical behavior of nuclear density calculated using the Fermi model [60] for ^{16}O in Fig. 1.4.

Based on the electron scattering experiment data, the two-parameter Fermi (2pF) model gives the quantitative information regarding the nuclear density distribution. The Fermi density ρ (fm^{-3}) depicted in Fig. 1.4 is a radial function and shows central density ρ_0 of nucleus core, which remains constant over a distance and then falls suddenly. From this distribution, one can extract relevant information related to the nuclear size like half-density radius R_0 (the distance corresponds to the half of ρ_0), surface thickness t (the distance at which ρ falls from $0.9\rho_0$ to $0.1\rho_0$) parameters. In Refs. [55, 61], the authors have compared the 2pF density function with the self-consistently determined nuclear densities. Important to mention here that, in the heavy-ion collisions, the surface part of colliding nuclei play prime role which is defined through the tail region. In Ref. [61], it has been observed that the self-consistently calculated densities are similar to that of the Fermi density in the surface/tail region of the density. Thus, the use of Fermi density is justified to study the heavy-ion collisions. Apart from 2pF density function, the physicists had also given three-parameter density functions, e.g. three-parameter Fermi (3pF) and three-parameter Gaussian (3pG) density functions. In the present work, I have considered the two- and three-parameter density functions to analyze the relative change in the tail region of nuclear densities and corresponding influence in the reaction dynamics.

Further, for determining the kinetic energy τ and spin-orbit density $\vec{J}$ terms, the authors Grammaticos and Voros [43, 44] had given the expressions for τ and $\vec{J}$ terms as a function of nuclear density in terms of $\hbar$ unit, within the framework of extended Thomas-Fermi approach (ETF). This exercise had given a semiclassical approach in determining τ and $\vec{J}$ terms, which further help in deriving the Skyrme Hamiltonian density functions for heavy-ion collisions. With the aid of semiclassical approach within the Skyrme Energy Density Formalism, the total energy of a system becomes the function of nuclear density alone. For determining $\tau(\rho)$ and $\vec{J}(\rho)$, one can introduce the exchange effects via the density approximations. In literature [62–64], different kinds of density approximations have been discussed and taken into consideration to understand the amalgamation process between two colliding nuclei. The sudden and adiabatic density approximations are the most commonly used faster and slower processes, respectively, for the consolidation of two nuclei into one another. For an illustration, if the kinetic energy (or relative average velocity $\approx 10^7$ m/s) of the projectile is about 1 MeV per nucleon, then the time of collision is of the order of 2×10^{-22} s, provided the interaction should take place at a separation distance of 2 fm. This time scale is smaller than the period of relaxation for projectile nucleus to get fused into one another. For such situation, the sudden density approximation is considerable [65–69]. On the other hand, the adiabatic density approximation refers the relatively slow approach and allows a continuous exchange of energy between two colliding nuclei for complete amalgamation of projectile into target nuclei [66,68]. On the basis of above discussed density approximations, one can observe the corresponding change in the behavior of nuclear potential. Along with the sudden density approximation, many authors have adopted other alternative ways of adding nuclear densities, like frozen, modified-sudden and relaxed-density approximations, and employed within the SEDF and phenomenological based potentials to observe the corresponding influence in fusion dynamics [28, 65, 67, 69, 70]. In the present thesis, the effect of above mentioned density approximations has been studied for the heavy-ion induced reactions and discussed the related results in the Chapter 3 of the present thesis.

So far, I have discussed about the nucleus-nucleus interaction potential which is obtained through the semiclassical approach of Skyrme Energy Density Formalism using the ETF method. It is noteworthy that, for addressing the nuclear properties of a large variety of nuclei which are lying nearer or far away from the β-stability line, many authors have given different sets of Skyrme force parameters [35,45,71–78]. In the present work, different choices of Skyrme forces have been taken into account and analyzed their importance in studying the heavy-ion induced reactions at the low-energy regime. Also, the phenomenological model, i.e. nuclear proximity theorem [24] and Woods-Saxon approach [28], based potentials are considered and compared with the SEDF based potential for different projectile-target combinations. Further, the addition of nuclear potential with the Coulomb and centrifugal potentials gives the Coulomb barrier, see in the schematic picture of Fig. 1.3. In other words, the fusion threshold barrier (or Coulomb barrier) opposes the amalgamation of two positively charged nuclei owing to mutual repulsive Coulomb and centrifugal potentials. If a projectile nucleus has sufficient kinetic energy, it may overcome/penetrate the barrier posed by the mutual interaction of colliding partners and a new nuclear entity may be synthesized. As it is known that, the nuclear structure effects play a prominent role at the below barrier energies. However, these effects start disappearing at the above barrier energies due to dominant behavior of centrifugal potential over the nuclear proximity potential. Therefore, the interaction between two nuclei may lead to the formation of a compound nucleus along with the other competing nuclear decay mechanisms at different range of incident energies, lying across the Coulomb barrier. Also, it has been analyzed by many theoreticians that, the fusion barrier characteristics (barrier position R_B, barrier height V_B and barrier curvature $\hbar\omega_B$) are sensitive towards the mass/charge number, deformation, orientation, excitation energy, angular momentum, etc. In the present work, I intend to examine the importance of quadrupole and octupole deformed nuclei, in reference to the spherical shapes, in the fusion-fission dynamics. The relevant role of excitation energy, angular momentum etc. is duly addressed.

In the formation and disintegration of an excited compound nuclear system at the low-energy region, the nuclear surface interactions take place, therefore the outer surface shape of colliding nuclei plays a very crucial role. The shape of a nucleus in its ground state can be spherical or deformed. In general, the doubly magic nuclei in which neutron and protons shells are completely filled are spherical. As the nucleons are added beyond the magic number, it causes a long-range correlation and the nuclear shape starts deviating from spherical configuration. In Fig. 1.5(a), the number of protons (Z) and neutrons for isotopes lying near and far away from the $N = Z$ line are shown on the horizontal and vertical axes, respectively. In this figure, the color mapping represents the value of static quadrupole (β_2) deformation of different signs i.e. +/-, along with the spherical nuclei. As per the Nuclear Data Table of ground state deformations of Möller *et al* [79], the spherical nuclei and prolate nuclei ($\beta_2^+ > 0$) of rugby ball shape are found as the most abundant nuclei in this island of nuclides, in comparison to oblate nuclei ($\beta_2^- < 0$) of disc shape.

Note that, in the present work, the nuclear shapes considered are axially symmetric shapes and colliding in a plane. To give the evidence of deformed shapes, the researchers have used the Coulomb excitation process as a tool to measure the electric transition probabilities [80–85]. Amongst all the deformed shapes of different order ($\beta_{\lambda=2,3,4}$), the shapes e.g. quadrupole β_2 and hexadecapole β_4 deformed nuclei possessing symmetry around the axial and reflection axes are the most commonly observed nuclei [86–94]. However, it is very difficult to give the evidence of axial-symmetry and reflection-symmetry breaking shapes (pear shapes). In other words, the symmetry-breaking pear shapes of nuclei are very rare. With the consistent efforts and advancements in the technologies, the researchers were able to experience the existence of octupole deformed pear-shapes (up to β_3) nuclei. In literature [83,95–100], there are very few experimentally observed β_3-deformed nuclei, and limited cases are reported for proton numbers (Z) = 34, 56, 86 and 88 and neutron numbers (N) = 34, 56, 88, 134 and 136. The presence of octupole deformation in a nucleus enhances the nuclear Schiff moments, which in turn, influences the Electric Dipole Moments (EDMs). Thus, the octupole deformed nuclei are important in obtaining the permanent EDMs [83, 101]. Also, in the nuclear fusion process, the non-zero EDMs in one of the fusing partners (i.e. $^{16}O+^{224}Ra$) show remarkable impact on the fusion barrier and sub-barrier cross-sections [84].

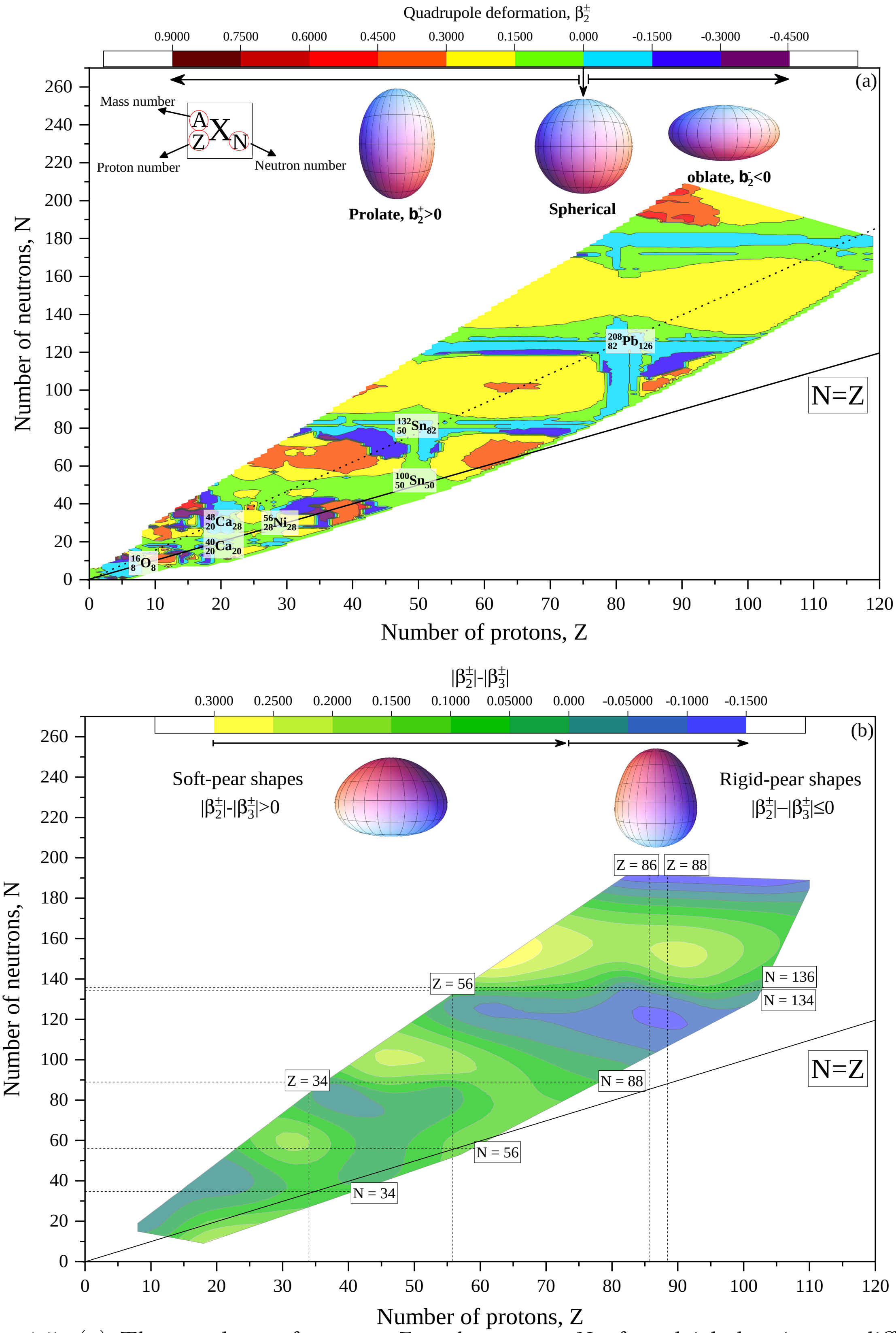

Figure 1.5: (a) The numbers of proton Z and neutron N of nuclei belonging to different mass-region shown along the horizontal and vertical axes, respectively, and the corresponding value of nuclear deformations (spherical, prolate $\beta_2^+ > 0$ and oblate $\beta_2^- < 0$) [79] represented through the color mapping. (b) The difference between the magnitude of quadrupole $\beta_2^{\pm}$ and octupole $\beta_3^{\pm}$ deformations is represented by the color mapping with respect to the number of nucleons (neutrons and protons).

In the present thesis, the importance of nuclear deformations in nuclear fusion-fission mechanisms has been discussed for octupole deformed nuclei, in comparison to the quadrupole deformed and spherical shapes of colliding nuclei. From Fig. 1.5(b), one can see that, most of the octupole deformed nuclei fall away from the N = Z line. In this figure, the color mapping represents the difference in the magnitude of $\beta_2^{\pm}$ and $\beta_3^{\pm}$ deformations. In order to analyze the importance of magnitude as well as +/- signs of β_3-deformation in the synthesis process, the octupole deformed nuclei are categorized as: (1) for $|\beta_2^{\pm}| - |\beta_3^{\pm}| > 0$ and (2) $|\beta_2^{\pm}| - |\beta_3^{\pm}| \leq 0$ cases, the related octupole deformed nuclei are called as soft- and rigid-pear shape nuclei. In the present thesis, the importance of 'elongated or cold' and 'compact or hot' configurations of the above said pear-shapes has been explored.

Like deformation degree of freedom, the orientation of a deformed nucleus relative to the spherical or deformed colliding nuclear partner also plays important role to study the compound nuclear reactions at the low energy. For the synthesis of heavy and superheavy elements, either of the two nuclear mechanisms, namely hot and cold fusion processes are used [12,102–105]. These fusion phenomena have been described successfully when either one or both of the colliding nuclear partners are deformed [106–109]. For such kind of target-projectile combinations, the fusion barrier extracted from the total interaction potential depends on the deformation and orientation of deformed nucleus relative to the colliding nuclear partner (spherical or deformed). As an illustration, the lowest barrier height and largest interaction distance between the colliding nuclei exhibit the polar orientation (θ=0^o or 180^o) of a prolate nucleus, and leads to the cold fusion process. On the other hand, the highest barrier height and smallest interaction distance related to the equatorial orientation (θ=90^o) of β_2^+ leads to a hot fusion process. The theories explained to illustrate the concept of hot and cold fusion processes are developed on the basis of uniquely fixed or optimum orientation (θ_{opt}) for quadrupole deformed nuclei [110–113]. These orientations depend on +/- signs of β_2 deformation. As a consequence, an enhancement is observed in fusion probability of heavy/superheavy nuclear systems [114–122]. In addition to the above analysis, the impact of reflection symmetry-breaking pear shapes of octupole deformed nuclei needs further exploration in nuclear fusion-fission kinds of processes. In view of this, I have worked on θ_{opt} which define both the cold and hot fusion configurations of octupole deformed nuclei. Therefore, in our recent work [123], it has been observed that, the octupole deformed nuclei which distort the spherically symmetric or quadrupole deformed nuclei into pear shape significantly modify θ_{opt}, in reference to that obtained for β_2-deformed nuclei in [110]. Further the corresponding influence of the above mentioned nuclear shapes and their related orientation effects in nuclear fusion-fission dynamics [124, 125] has been discussed in detail in Chapters 5, 6 and 7.

1.3.2 Wong model and its extended version

The heavy-ion collisions at the low-energy regime may lead to the formation of a compound nuclear system and subsequent decay mechanisms. The total interaction potential, comprised of Coulomb, centrifugal and nuclear potentials, is considered as a basic and important tool to understand the compound nuclear reaction dynamics. In order to determine the possibility of formation and subsequent decay dynamics, the details of fusion barrier characteristics (barrier position R_B, barrier height V_B and barrier curvature $\hbar\omega_B$) extracted from the total interaction potential are required. These barrier parameters get influenced under various factors, like deformation, orientation, angular momentum, temperature/energy etc. Also, one can notice the barrier modifications due to different choices of nuclear potentials derived either through phenomenological model or SEDF approach, various nuclear density approximations and relative change in the tail region of nuclear density due to two- and three-parameter density function. Further, the role of above said factors can be observed in terms of the fusion cross-sections (σ_{fus}), for a wide range of incident energies lying across the Coulomb barrier, calculated using the Wong formula given by C. Y. Wong in 1973 [126]. On the basis of scattering and partial wave theory [127], the researchers had given a formula to calculate the total reaction cross-sections. Based on this relation, Wong had obtained a simple analytical expression by approximating the interaction barriers using the inverted Harmonic Oscillator. As a consequence, the formula for σ_{fus} as a function of V_B, R_B, and $\hbar\omega_B$ has been obtained for ℓ^{th}-partial wave. Also, Wong had conducted ℓ-summation under several approximations, which uses the $\ell = 0$ case or s-partial wave barrier characteristics [126]. Further, in [128], the ℓ-summations has been performed explicitly by the authors and renamed the procedure as extended ℓ-summed Wong model. The fusion cross-section determined using this extended version of the Wong formula is expressed in terms of quantum-mechanical transmission probability for the ℓ^{th}-partial wave. In the calculation of σ_{fus} via extended ℓ-summed Wong model, the values of ℓ_{max} are obtained using the sharp

cut-off model [129] for the above barrier energies and extrapolated for the below barrier energies. The calculated values of fusion cross-sections over a wide range of center of mass energies ($E_{c.m.}$) for the considered choices of projectile-target combinations are compared with the available experimental results. With this comparative analysis, one can observe the significance of deformations, orientations and other factors for energies lying below, near and above the Coulomb barrier. Also, the fusion hindrance phenomena can be studied using different choices of Skyrme force, density approximations and density distribution functions especially at the sub-barrier region. Important to mention that, to deal with the fusion hindrance phenomena, an extra energy is required to fuse the colliding nuclear partners and is called as the extra-push energy. In view of this, many authors have implemented this idea and analyzed the influence of different factors, such as channel-coupling effects, dynamical deformations and phenomenological model, which in turn provides extra-push energy at below barrier region to address the fusion hindrance [130–135].
After investigating the fusion possibility among variety of projectile-target combinations, the formed CN in an excited state decays generally via the binary fragments. The models and theories adopted to understand the probability of possible decaying fragments from the equilibrated CN is discussed in the following section.

1.3.3 Quantum Mechanical Fragmentation Theory

The behavior of a nucleus analogy to an incompressible liquid was proposed by George Gamow [136]. Due to the collective effect of nuclear intrinsic properties, the competition between the cohesive nuclear force and repulsive Coulomb force leading towards the fission process of excited compound nuclei was partially illustrated on the basis of the liquid-drop model (LDM). Further with the use of this model, the nucleons were assumed to be distributed uniformly, however the obtained results were not so satisfying especially for non-magic nucleons or valence particles. In other words, there was discrepancy of shell effects which define nucleon distribution in an adequate manner. In view of this, the researchers initiated with the one-center shell model with the use of Nilsson Oscillator potential [137]. Later for highly deformed nuclei, Maruhn and Greiner had given Asymmetric Two Center Shell Model (ATCSM) [138–141] and developed potential for protons and neutrons moving in separate shells. In this model, the microscopic part of the potential had been obtained with the use of Strutinsky method employed for determining the shell-correction energy, defined as the difference between the single particle energy obtained for the shell quantal distribution of nucleons and uniformly distributed nucleons [142]. On the other side. the macroscopic part in the potential developed on the basis of ATCSM has been obtained via LDM of Myers and Swiatecki [143]. The above approaches are employed mainly to determine the potential energy surface. For full dynamical study of excited Compound nucleus de-excitation, the co-ordinates of mass- (η_A) and charge-asymmetry (η_Z) parameters should be introduced and has been incorporated in the dynamical fragmentation theory, or referred as the Quantum Mechanical Fragmentation Theory (QMFT) [144, 145]. The theory developed on the collective degrees of freedom, i.e. relative separation distance, nuclear deformation, orientation, neck-length parameter, mass- and charge-asymmetry parameters, has been given as a unified description of the two-body channels for illustrating different nuclear mechanisms at the same platform [146, 147].

On the basis of QMFT, one can analyze the dynamic effect of η_A and η_Z co-ordinates in terms of the mass and charge distribution of binary fragments decaying from the heavy-mass Compound nucleus, by solving the Schrodinger equation as a function of these co-ordinates. Here, the probability of formation of the possible binary fragments/clusters is estimated at the CN state. Further, the preformed clusters can penetrate through the interaction potential developed between two fragments at a fixed turning point. With the use of the neck-length parameter $\triangle R$, which is the only parameter of this collective clusterization approach or Dynamical Cluster-decay Model (DCM), one can fix the turning point of the barrier penetration. The probability of pre-born fragments is termed as preformation probability P_0 and shows inverse trend from that of fragmentation potential. On the basis of these conceptual ideas, the authors have spent many years and given rigorous efforts in understanding the disintegration of excited CN in terms of cross-sections, mass/charge distribution or yields, with the effect of static/dynamic nuclear deformation and orientation, shell-effects, temperature, angular momenta, etc. [148–152]. In the present thesis, the behavior of mass and charge distributions has been understood for different choices of the nuclear potentials obtained using different sets of Skyrme force parameters [74] within the semiclassical approach of SEDF [125, 153]. The above analysis has been discussed for the disintegration of light- and heavy-mass isotopes of actinide (i.e. Thorium) at the low values of excitation energy [125].

1.4 Motivation of the work

I am interested to study (i) the formation of an exotic compound nuclear system, which is formed in an excited state via the heavy-ion collision process, and (ii) subsequent decay mechanisms such as fission process. For the above analysis, the nucleus-nucleus interaction potential is known to be the basic tool to understand the fusion possibility between the considered choices of projectile-target (P-T) combinations and possible binary fragmentation analysis of the formed nuclear entity. Unlike Coulomb and centrifugal potentials, the study of nuclear potential for variety of colliding nuclear partners is the main concern. In the present work, the semiclassical approach of Skyrme Energy Density Formalism (SEDF), which gives effective nuclear interaction potential, is used to study the heavy-ion induced reactions. The employment of different sets of Skyrme force parameters within SEDF help in addressing the nuclear properties of nuclei belonging to different mass-region.

Here, the semiclassical SEDF approach based nuclear potential expressed in terms of the Skyrme Hamiltonian density function depends on the nuclear density ρ, kinetic energy density τ and spin-orbit density $\vec{J}$ terms. The τ and $\vec{J}$ obtained within the framework of extended Thomas-Fermi approach (ETF) are also density dependent terms. This motivates to understand the exchange and non-exchange effects among the two colliding nuclear partners, via the density approximation. In the present work, different density approximations: sudden, modified-sudden, frozen and relaxed-density approximations, have been employed within the SEDF and phenomenological based potentials. The corresponding effects have been observed on the fusion barrier characteristics and subsequently on the fusion cross-sections, at below, near and above the Coulomb barrier energies, for the considered P-T combinations. In addition to this, the relative change in the tail region of density profile, due to two- and three-parameter density functions, shows respective modifications in the fusion dynamics. This analysis prompts in making a better choice of density distribution function for addressing the fusion hindrance phenomena of the mass-symmetric and asymmetric nuclear partners. Also, the calculated fusion cross-sections using the Wong formula and its extended version are compared with the available experimental data, for the incident energies lying across the Coulomb barrier. Such comparative analysis motivates to empathize the importance of nuclear structure effects in the sub-barrier region.

In addition to above, the incorporation of deformations (up to β_3) and orientation effects within the SEDF and phenomenological based potentials aids to understand the significance of symmetry-breaking pear shapes in the nuclear fusion as well as the decay mechanisms, as compared to the spherical-symmetry nuclear shapes. In other words, the optimized orientations corresponding to the 'elongated' and 'compact' fusion configurations of pear-shape octupole deformed nuclei may illustrate the production possibility of new elements and help in extending the periodic-table. Also, the mass- and charge-distributions of formed compound nuclear systems have also been examined by including deformations (up to β_3) and related optimum orientations effects within the Dynamical Cluster-decay Model (DCM), which is based on the collective clusterization approach of Quantum Mechanical Fragmentation Theory (QMFT). Also, in the above analysis, the role of different Skyrme forces has been analyzed via the mass and charge dispersion of light- and heavy-mass isotopes of actinide, at the low excitation energies.

To give a systematic detail on the above said ideas regarding the formation and disintegration of exotic compound nuclear systems formed via the heavy-ion induced reactions, the present thesis is categorized according to the following mentioned objectives:

- The effect of different density approximations for compound nuclear systems within the framework of SEDF. It is proposed to study heavy-ion induced reactions using phenomenological and SEDF based potentials.
- The relevance of different Skyrme based potentials in reference to fusion-fission process
- The role of nuclear deformations in context of reaction dynamics
- Comparison of theoretical results with available experimental data and possible predictions for future experiments

The organization of present thesis on the basis of above said objectives is discussed in the following section.

1.5 Organisation of Thesis

The present thesis is organized as follows:

In **Chapter 2** of Methodology, different density distributions and approximations are employed within the semiclassical approach of Skyrme Energy Density Formalism (SEDF). Thus, the effective nucleus-nucleus interaction potential obtained due to the SEDF approach as a constituent term of the total interaction potential helps in determining the probability of fusion between the considered choices of projectile-target combinations and relevant idea of decaying fragments. To understand the role of nucleus deformed shapes and their relative orientation in the compound nucleus formation and related decay mechanisms, these degrees of freedom, i.e. deformation (taken up to β_3) and orientation are introduced within the SEDF approach through the nuclear radius vector. Subsequently, the collective effect of barrier characteristics can be examined via determining the fusion cross-sections using the Wong formula and the mass (and charge) distributions of formed nuclear entity via the collective clusterization approach.

Chapter 3 discusses about different density approximations, which illustrate different ways of adding the projectile-target densities for obtaining the compound nucleus density. These density approximations have been introduced within the Skyrme Hamiltonian density terms, which in turn, help in determining the fusion barrier characteristics. For the above analysis, the Ni-based reactions are taken into consideration and obtained the fusion cross-sections, depending on the barrier parameters, across the Coulomb barrier energies.

In **Chapter 4**, the idea is to explore the relevance of different density functions in the formation of compound nuclei, formed from symmetric and asymmetric kinds of projectile-target combinations. Here, the two-parameter Fermi (2pF), three-parameter Fermi (3pF) and three-parameter Gaussian (3pG) density functions have been utilized within the SEDF approach to study the fusion dynamics of ^{58}Ni-based reactions. In this chapter, one is able to understand the significance of additional parameter, involved within the three-parameter density functions, in fusion dynamics of above said projectile-target combinations. So far, the analysis has been done for colliding nuclei of spherical shapes.

In **Chapter 5**, the influence of soft- and rigid-pear shapes has been explored, in reference to the quadrupole deformed nuclei, at the uniquely fixed or optimum orientations, defining the 'compact or hot' and 'elongated or cold' fusion configurations. The results obtained with the effect of quadrupole and octupole deformations and related optimum orientations are discussed using the SEDF and phenomenological based potentials.

In **Chapter 6**, a detailed analysis of the fusion probability among the spherical-octupole and quadrupole-octupole deformed pairs of colliding nuclei has been discussed in terms of fusion barrier and fusion cross-sections. In this chapter, the significant impact of pear-shape nuclei has been illustrated over all the orientations, via integrating the fusion cross-sections using the Wong formula. The results are discussed in reference to that of quadrupole deformations and compared with the available experimental data of fusion cross-sections across the Coulomb barrier energies.

In **Chapter 7**, an exercise has been done in order to analyze the possibility of octupole deformed fragments in the decay of light- and heavy-mass isotopes of Thorium, i.e. $^{222,224,226,228,230}Th^*$. To carry forward the above idea, the mass- and charge-dispersion of chosen Th isotopes have been analyzed by including deformations (up to β_3) and related optimum orientation effects within the collective clusterization approach.

At the end, **Chapter 8** gives a brief note on the work done in reference to the proposed objectives of the present thesis along with the future possibilities that arise from the established results.

Bibliography

[1] H. Becquerel, Compt. Rend. **122**, 420 (1896).

[2] E. Rutherford F. R. S., Phil. Mag. Ser. 6 Vol. 37, No. 222, June 1919.

[3] H. Yukawa, Proc. Phys.-Math. Soc. Jpn. **17**, 48 (1935).

[4] S. H. Neddermeyer and C. D. Anderson, Phys. Rev. **51**, 884 (1937).

[5] N. V. Antoneko *et al*, Phys. Lett. B **319**, 425-430 (1993).

[6] N. V. Antoneko *et al*, Phys. Rev. C **51**, 5 (1995).

[7] M. K. Sharma *et al*, Phys. Rev. C **70**, 044606 (2004).

[8] D. P. Singh *et al*, Phys. Rev. C **80**, 014601 (2009).

[9] P. K. Rath *et al*, Phys. Rev. C **79**, 051601(R) (2009).

[10] P. K. Rath *et al*, Phys. Rev. C **88**, 044617 (2013).

[11] N. Bohr, Science **86**, 2225 (1937).

[12] Yu. Ts. Oganessian *et al*, Phys. Rev. C **70**, 064609 (2004).

[13] R. D. Woods and D. S. Saxon, Phys. Rev. **95**(2), 577-578 (1954).

[14] W. Kohn and L. J. Sham, Phys. Rev. Vol. **137** No. 6A (1965).

[15] W. Kohn and L. J. Sham, Phys. Rev. A **137**, 1697 (1967).

[16] P. Hohenber and W. Kohn, Phys. Rev. **136**, 1384 (1964).

[17] R. A. Berg and L. Wilets, Phys. Rev. **101**, 201 (1956).

[18] K. A. Brueckner *et al*, Phys. Rev. **171**, 1188 (1968).

[19] W. Scheid and W. Greiner, Z. Phys. **226**, 364 (1969).

[20] R. J. Lombard, Ann. Phys. (N. Y.) **77**, 380 (1973).

[21] C. Ngô *et al*, Nuc. Phys. A**240**, 353 (1975).

[22] G. R. Satchler and W. G. Love, Phys. Rep. (Review Section of Physics Letters) **55**, No. 3, 183-254 (1979).

[23] O. N. Ghodsi and N. M. Amiri, Phys. Rev. C **104**, 044618 (2021).

[24] J. Blocki *et al*, Ann. Phys. **105**, 427-462 (1977).

[25] P. Möller and J. R. Nix, Nucl. Phys. A **361**, 117 (1981).

[26] W. Reisdorf, J. Phys. G: Nucl. Part. Phys. **20**, 1297 (1994).

[27] V. Y. Denisov, Phys. Lett. B **526**, 315 (2002).

[28] V. Yu. Denisov, Phys. Rev. C **91**, 024603 (2015).

[29] D. Vautherin and D. M. Brink, Phys. Rev. C **5**, 626 (1972).

[30] D. Vautherin, Phys. Rev. C **7**, 1 (1973).

[31] T. H. R. Skyrme, Proc. Roy. Soc. Lond. **A226**, 521-530 (1954).

[32] T. H. R. Skyrme, Proc. Roy. Soc. Lond. **A230**, 277-286 (1955).

[33] J. S. Bell and T. H. R. Skyrme, Phil. Mag. **1**, 1055-1068 (1956).

[34] T. H. R. Skyrme, Nucl. Phys. **9**, 615-635 (1959).

[35] D. M. Brink and Fl. Stancu, Nucl. Phys. A**243**, 175-188 (1975).

[36] P. Hohenberg and W. Kohn, Phys. Rev. **136**, B864-B871 (1964).

[37] D. R. Hartree, Proc. R. Soc. London **A113**, 621 (1928).

[38] V. Fock, Z. Phys. **61**, 126 (1930).

[39] J. C. Slater, Phys. Rev. **81**, 3 (1951).

[40] H. De Vries *et al* , Atomic data and Nuclear data tables **36**, 495-536 (1987).

[41] H. A. Bethe, Phys. Rev. **167**, 879 (1968).

[42] W. D. Myers and W. J. Swiatecki, Ann. Phys. (N. Y.) **55**, 395 (1969).

[43] B. Grammaticos and A. Voros, Ann. Phys. **123**, 359-380 (1979).

[44] B. Grammaticos and A. Voros, Ann. Phys. **129**, 153-171 (1980).

[45] M. Brack, C. Guet, H. -B. Hakanson, Phys. Rep. **123**, 275-364 (1985).

[46] L. Bennour *et al*, Phys. Rev. C **40**, 2834 (1989).

[47] H. Feshbach, *Theoretical Nuclear Physics; Nuclear Reactions* (John Wiley & Sons), New York (1992).

[48] J. Bartel and K. Benchrikh, Eur. Phys. J. A **14**, 179-190 (2002).

[49] V. Yu. Denisov and W. Norenberg, Eur. Phys. J. A **15**, 375-388 (2002).

[50] O. N. Ghodsi and M. Khalaz, Int. J. Mod. Phys. E, Vol. **27**, No. 02, 1850016 (2018).

[51] N. F. Mott, Proc. Roy. Soc. **A124**, 425 (1929).

[52] N. F. Mott, Proc. Roy. Soc. **A135**, 429 (1932).

[53] E. Guth, Wien. Anz. Akad. Wiss. **24**, 299 (1934).

[54] M. E. Rose, Phys. Rev. **73**, 282 (1948).

[55] L. R. B. Elton, Proc. Phys. Soc. Lond. A **63**, 1115 (1950).

[56] R. Hofstadter, Rev. Mod. Phys. **28**, 214 (1956).

[57] K. K. Seth, Physics Today 11, 5, 24 (1958).

[58] E. M. Lyman, A. O. Hanson and M. B. Scott, Phys. Rev. **79**, 228 (1955).

[59] D. C. Tayal, *Nuclear Physics*, General Properties of Atomic Nucleus, page no. 11, published in Himalaya Publishing House Pvt. Ltd. (2012).

[60] B. Hahn, D. G. Ravenhall and R. Hofstadter, Phys. Rev. **101**, 1131 (1956).

[61] R. K. Gupta, D. Singh and W. Greiner, Phys. Rev. C **75**, 024603 (2007).

[62] K. A. Brueckner *et al*, Phys. Rev. **173**, 944 (1968).

[63] J. Galin *et al*, Phys. Rev. C **9**, 1018 (1974).

[64] J. D. Perez, Nucl. Phys. A **191**, 19 (1972).

[65] Li Guo-Qiang, J. Phys. G: Nucl. Part. Phys. **17**, 1-34 (1991).

[66] T. Ichikawa, K. Hagino and A. Iwasmoto, Phys. Rev. Lett. **103**, 202701 (2009).

[67] R. Kumar, M. K. Sharma and R. K. Gupta, Nucl. Phys. A **870-871**, 42-57 (2011).

[68] T. Ichikawa, Phys. Rev. C **92**, 064604 (2015).

[69] S. Jain. R. Kumar and M. K. Sharma, Eur. Phys. J. A **54**, 203 (2018).

[70] V. Yu. Denisov and W. Norenberg, Eur. Phys. J. A **15**, 375-388 (2002).

[71] Fl. Stancu and D. M. Brink, Nucl. Phys. A**270**, 236-254 (1976).

[72] D. M. Brink and Fl. Stancu, Nucl. Phys. A**299**, 321-332 (1978).

[73] Keh-Fei LIU *et al*, Nucl. Phys. A**534**, 1-24 (1991).

[74] B. K. Agarwal, S. Shlomo and V. Kim Au, Phys. Rev. C **72**, 014310 (2005).

[75] B. K. Agarwal, S. K. Dhiman and R. Kumar, Phys. Rev. C **73**, 034319 (2006).

[76] Lie-Wen Chen *et al*, Phys. Rev. C **82**, 024321 (2010).

[77] M. Dutra *et al*, Phys. Rev. C **85**, 035201 (2012).

[78] Zhen Zhang and Lie-Wen Chen, Phys. Rev. C **94**, 064326 (2016).

[79] P. Möller *et al*, At. Data and Nucl. Data Tables **109-110**, 1-204 (2016).

[80] H. Wollersheim *et al*, Nucl. Phys. A **556**, 261 (1993).

[81] A. Bharti and S. K. Khosa, Phys. Rev. C**53**, 2528 (1996).

[82] ZHU Sheng-jiang *et al*, Chin. Phys. Lett. **14**, 569 (1997).

[83] L. P. Gaffney *et al*, Nature **497**, 199 (2013).

[84] R. Kumar, J. A. Lay and A. Vitturi, Phys. Rev. C **92**, 054604 (2015).

[85] M. Alimohammadi, L. Fortunato and A. Vitturi, Eur. Phys. J. A **134**, 570 (2019).

[86] D. R. Bès and Z. Szymanski, Nucl. Physics **28**, 42-62 (1961).

[87] C. W. Towsley *et al*, Nucl. Phys. A **204**, 574-592 (1973).

[88] R. W. Ibbotson *et al*, Phys. Rev. Lett. **80**, 10 (1998).

[89] E. Nacher *et al*, Phys. Rev. Lett. **92**, 23 (2004).

[90] A. Gorgen and W. Korten, J. Phys. G: Nucl. Part. Phys. **43**, 024002 (2016).

[91] N. T. Jarallah, Energy Procedia **157**, 276-282 (2019).

[92] Manju *et al*, Proceedings of DAE Symp. Nucl. Phys. **63**, (2018).

[93] Manju *et al*, Eur. Phys. J. A **55**, 5 (2019).

[94] Manju *et al*, Nucl. Phys. A **1010**, 122194 (2021).

[95] W. Nazarewicz, P. Olanders and I. Ragnarsson, Nucl. Phys. A **429**, 269-295 (1984).

[96] I. Ahmad and P. A. Butler, Annu. Rev. Nucl. Part. Sci. **43**, 71-116 (1993).

[97] P. A. Butler and W. Nazarewicz, Rev. Mod. Phys. **68**, 349-421 (1996).

[98] P. A. Butler, J. Phys. G: Nucl. Part. Phys. **43**, 073002 (2016).

[99] B. Bucher *et al*, Phys. Rev. Lett. **116**, 112503 (2016).

[100] S. J. Zhu *et al*, Phys. Rev. Lett. **124**, 032501 (2020).

[101] W. Urban *et al*, Nucl. Phys. A **613**, 107-131 (1997).

[102] R. G. Stokstad *et al*, Phys. Rev. C **21**, 2427 (1980).

[103] K. Morita *et al*, J. Phys. Soc. Japan **73**, 2593 (2004).

[104] Yu. Ts. Oganessian *et al*, Phys. Rev. C **74**, 044602 (2006).

[105] K. Morita *et al*, J. Phys. Soc. Japan **76**, 043201 (2007).

[106] A. Sandulescu *et al*, Phys. Lett. B **60**, 225 (1976).

[107] R. K. Gupta, A. Sandulescu and W. Greiner, Phys. Lett. B **67**, 257 (1977).

[108] R. K. Gupta, C. Parvulescu, A. Sandulescu and W. Greiner, Z. Phys. A **283**, 217 (1977).

[109] R. K. Gupta, A. Sandulescu and W. Greiner, Z. *Natureforsch.* **32a**, 704 (1977).

[110] R. K. Gupta *et al*, J. Phys. G: Nucl. Part. Phys. **31**, 631-644 (2005).

[111] A. Nasirov *et al*, Nucl. Phys. A **759**, 342-369 (2005).

[112] N. Wang *et al*, Phys. Rev. C **74**, 044604 (2006).

[113] M. Ismail and W. M. Seif, Phys. Rev. C **81**, 034607 (2010).

[114] A. S. Umar *et al*, Phys. Rev. C **81**, 064607 (2010).

[115] D. Jain, R. Kumar and M. K. Sharma, Nucl. Phys. A **915**, 106-124 (2013).

[116] Long Zhu *et al*, Phys. Rev. C **90**, 014612 (2014).

[117] F. Lari and O. N. Ghodsi, Commun. Theor. Phys. **65**, 213-218 (2016).

[118] I. Sharma, M. S. Gautam and M. K. Sharma, International J. Mod. Phys. E **26**, 1750077 (2017).

[119] K. Hagino, Phys. Rev. C **98**, 014607 (2018).

[120] M. Bhuyan, R. Kumar and B. V. Carlson, Journal of Physics: Conf. Series **1291**, 012017 (2019).

[121] T. Sahoo, M. Kaur, R. N. Panda, P. R. Das and S. K. Patra, Int. J. Mod. Phys. E **28**, 1950095 (2019).

[122] R. Kumar, M. Bhuyan, D. Jain and B. V. Carlson, Chapter 52 Title: *Theoretical description of low-enegry nuclear fusion*, Book Title: *Nuclear Fusion*, Edited by: A. Shukla and S. K. Patra, ISBN: 9780429288647, Publishers: CRC Press, London (2020).

[123] S. Jain, M. K. Sharma and R. Kumar, Phys. Rev. C **101**, 051601(R) (2020).

[124] S. Jain, R. Kumar and M. K. Sharma, Chin. Phys. C Vol. **46**, No. 1, 014102 (2022).

[125] S. Jain, R. Kumar, S. K. Patra and M. K. Shamra, Phys. Rev. C **105**, 034605 (2022).

[126] C. Y. Wong, Phys. Rev. Lett. **31**, 766 (1973).

[127] C. Amsler, *Nuclear and Particle Physics*, IOP Publishing (2015).

[128] R. Kumar *et al*, Phys. Rev. C **80**, 034618 (2009).

[129] M. Beckerman *et al*, Phys. Rev. C **23**, 4 (1981).

[130] W. J. Swiatecki, Nucl. Phys. A **376**, 275-291 (1982).

[131] H. Gaggeler *et al*, Z. Phys. A – Atoms and Nuclei **361**, 291-307 (1984).

[132] M. Dasgupta *et al*, Annu. Rev. Nucl. Part. Sci. **48**, 401-61 (1998).

[133] C. Simenel, Eur. Phys. J. A **48**, 152 (2012).

[134] K. Sekizawa and K. Yabana, Phys. Rev. C **88**, 014614 (2013).

[135] K. Washiyama, Phys. Rev. C **91**, 064607 (2015).

[136] G. Gamow, Proc. R. Soc. Lond. A **126**, 632-644 (1930).

[137] S. G. Nilsson, Dan. Mat. Fys. Medd. **29**, 16 pp.1-69 (1955).

[138] J. Maruhn and W. Greiner, Z. Physik **251**, 431 (1972).

[139] R. A. Gherghescu, Phys. Rev. C **67**, 014309 (2003).

[140] R. A. Gherghescu, D. N. Poeneru and W. Greiner, Rom. J. Phys. Vol. **50**, Nos. 3-4, p. 377-383 (2005).

[141] R. A. Gherghescu *et al*, J. Phys. G: Nucl. Part. Phys. **32**, L73-L84 (2006).

[142] V. M. Strutinksy, Nucl. Phys. A**95**, 420-442 (1967).

[143] W. D. Myers and W. J. Swiatecki, Arkiv Fizik **36**, 343 (1967).

[144] J. Maruhn and W. Greiner, Phys. Rev. Lett. **32**, 548 (1974).

[145] R. K. Gupta, W. Scheid and W. Greiner, Phys. Rev. Lett. **35**, 353 (1975).

[146] H. Fink *et al*, Proc. Int. Conf. on Reactions between Complex Nuclei, Nashville, Tenn., USA, (North-Holland, Amsterdem), p.21 (1974).

[147] H. Fink *et al*, Proc. Int. School on Nuclear Physics, Predeal, Romania, p.75 (1974).

[148] S. Kumar and R. K. Gupta, Phys. Rev. C **55**, 1 (1997).

[149] M. Kaur, M. K. Sharma and R. K. Gupta, Phys. Rev. C **86**, 064610 (2012).

[150] D. Jain *et al*, Phys. Rev. C **85**, 024615 (2012).

[151] A. Kaur and M. K. Sharma, Phys. Rev. C **99**, 044611 (2019).

[152] N. K. Virk, M. K. Sharma and R. Kumar, Nucl. Phys. A **981**, 89-106 (2019).

[153] S. Jain, R. Kumar and M. K. Sharma, Proceedings of the DAE Symp. on Nucl. Phys. **65** (2021).

Chapter 2

Methodology

2.1 Introduction

To study the fusion and subsequent decay mechanisms of compound nuclear (CN) systems formed via heavy-ion induced reactions, the present chapter of Methodology briefs about the methods and approaches defining the interaction potentials, probability of fusion among colliding nuclei and subsequent decay of excited CN etc. For comprehensive understanding of nuclear reactions, the nucleus-nucleus interaction potential plays important role and the same is derived using the semiclassical approach of Skyrme Energy Density Formalism (SEDF) [1, 2] expressed as an algebraic function of kinetic energy density τ, spin-orbit density $\vec{J}$ and nuclear density ρ. With the use of this approach, one can understand different ways of adding the nuclear densities of colliding nuclei to obtain the compound nucleus density [3–9]. Also, the relative change in the tail region of density profiles (due to two and three-parameterized density functions) shows corresponding effect on the fusion barrier characteristics (barrier position R_B, barrier height V_B and barrier curvature $\hbar\omega_B$) and subsequently on the fusion cross-sections (σ_{fus}) for a variety of projectile-target combinations [10]. Here, the σ_{fus} which represents the collective effect of R_B, V_B and $\hbar\omega_B$ factors is calculated using the Wong formula of s-partial wave [11] and its extended version which takes into account the different partial waves via explicit summation of ℓ-values [12], over a wide range of incident energies ($E_{c.m.}$) lying across the Coulomb barrier.
Further, the Dynamical Cluster-decay Model (DCM) [13, 14] is applied to probe various decay mechanisms of CN formed in an excited state via heavy-ion induced reactions at the low-energy regime (i.e. $\leq$15 MeV/nucleon). The model has been built on the collective clusterization approach of Quantum Mechanical Fragmentation Theory (QMFT) [15]. On the basis of QMFT, the fragmentation potential $V(\eta)$ which is comprised of micro- [16–19] and macroscopic [1, 2, 11, 20] terms is discussed in detail. Further, the preformation probability, which is the solution of stationary Schrodinger equation in mass (and charge)

asymmetry parameter, defines the possibility of preformed fragments within the compound nuclear system. The preformed fragments start penetrating through the turning points and corresponding penetration probability is estimated using the Wentzen-Krammers-Brillouin (WKB) approximation [21]. Henceforth, with the collective effect of preformation and penetration probabilities, one can obtain the decay cross-sections over wide range of center of mass energy. As it is known that, the possible target-projectile combination forms an excited compound nucleus, and subsequently disintegrates generally into binary fragments under various conditions, such as excitation energy/temperature, angular momentum, deformations, orientations, etc. In the methodology, these factors are discussed to understand their corresponding impact in the nuclear fusion and corresponding decay mechanisms.
The Chapter begins with the nuclear radius term, which is an input term of contributing potentials (nuclear, Coulomb and centrifugal) and cross-sections. Further, the detail of nucleus-nucleus potential derived using the SEDF and phenomenological methods, along with the long-range repulsive potentials is given.

2.2 Nuclear radius

The shape of a nucleus as an intrinsic degree of freedom participates in evaluating the formation possibility of a compound nuclear system and subsequent fragments emission. Mathematically, one can define different shapes (either spherical or deformed) of nuclei in terms of the nuclear radius vector $R_i(\alpha_i)$, as given below [22–26]

$$
\begin{aligned}
R_i(\alpha_i, \phi_i) &= R_{0i}\left[1 + \sum_{\lambda,m} \beta_{\lambda i} Y_\lambda^m(\alpha_i, \phi_i)\right], \qquad (2.1)\\
R_{0i} &- \text{radius of nucleus which is in the spherical equilibrium shape}\\
\alpha_i &= \text{angle between radius Vector and symmetry axis}\\
\phi_i &- \text{Azimuthal angle} \neq 0 \text{ for non-coplanar case}\\
&= 0 \text{ for co-planar case}\\
\lambda &= 2, 3, 4, \ldots.\\
&- \text{the quantum number corresponds to deformed shapes of different order}\\
m &= -\lambda \text{ to } \lambda.
\end{aligned}
$$

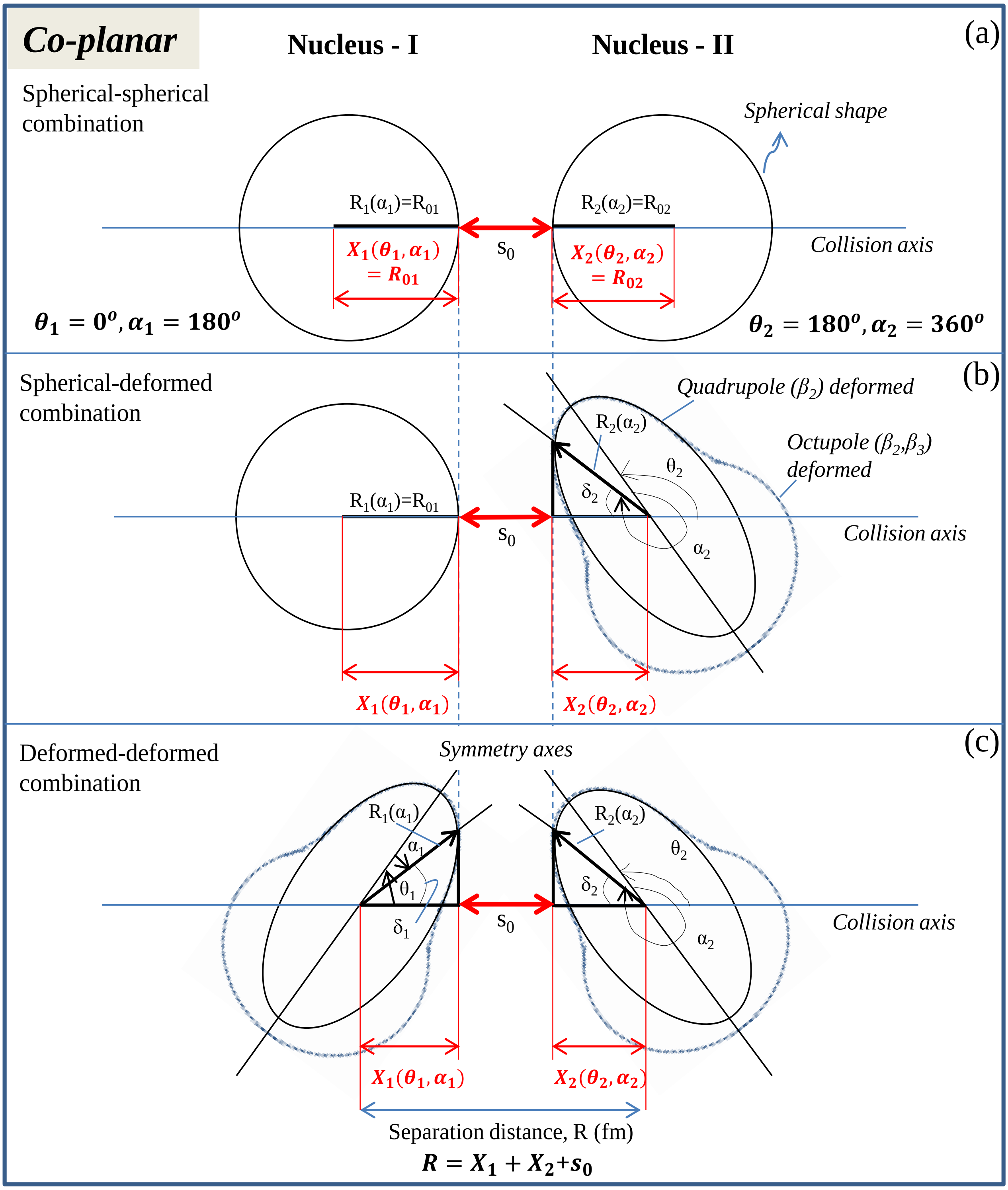

Figure 2.1: Geometrical representations of (a) spherical-plus-spherical, (b) spherical-plus-deformed, and (c) deformed-plus-deformed pairs of colliding nuclei, lying in the same plane. Note that, for deformed Nuclear I and Nucleus II, $X_i(\theta_i, \alpha_i) = R_i(\alpha_i)\cos\delta_i$, $i = 1, 2$; $\delta_1^{\beta_2} = \theta_1 - \alpha_1$, $\delta_1^{\beta_2\beta_3} = 180 + \theta_1 - \alpha_1$ and $\delta_2 = 180 + \theta_2 - \alpha_2$.

$$
\begin{aligned}
&& - && \text{magnetic quantum number, } m = 0 \text{ for axial symmetric shapes} \\
\beta_{\lambda i} && - && \text{the static deformation parameter [26]} \\
Y_\lambda^0(\alpha, \phi = 0) && = && \sqrt{\frac{(2\lambda+1)}{4\pi}} P_\lambda(cos\alpha);\ P_\lambda \text{ - Legendre polynomials.}
\end{aligned}
$$

Here, $i = 1$, 2 correspond to Nucleus I (projectile or fragment 1) and Nucleus II (target or fragment 2), respectively. Important to mention that, I have worked on axial symmetric shapes ($m = 0$) of two nuclei, colliding in a plane ($\phi_i = 0$). Apart from this, the term R_{0i} corresponds to the radius of spherical equilibrium shape. Different models give different expressions for R_{0i}, which are to be provided in the upcoming sections [10, 27–29]. On the basis of above relation, the importance of reflection-symmetry breaking pear-shapes (with axial-symmetry) of octupole deformed ($\beta_3^\pm$) nuclei has been explored in the fusion-fission nuclear mechanisms, in reference to the spherical and quadrupole deformed nuclei [8, 10, 30–32]. The values of static deformations (up to $\beta_3^\pm$) are taken from the Nuclear Data Table of ground state deformations, given by P. Mӧller and his co-authors [26].

Additionally, in relation to the deformation parameter β_λ, the term quadrupole moment Q_λ is introduced [33–36], which is in relation to the experimental data of transition energies $B(E\lambda)$ gave the evidence of nuclear shapes. Therefore, for a uniformly charged spheroidal shape of a nucleus, the quadrupole moment Q_λ as a function of β_λ is given as [33, 35]

$$
Q_\lambda = \frac{3}{\sqrt{(2\lambda+1)\pi}} Z R_0^\lambda \bar{\beta}_\lambda. \tag{2.2}
$$

Here, Z is the atomic number of the nucleus and $R_0 = 1.2A^{1/3}$ fm. In the above expression, $\bar{\beta}_\lambda$ is a function of β_2, β_3, β_4,....... deformation parameters. In the present work, $\bar{\beta}_\lambda$ is taken upto β_3 as given below:

$$
\bar{\beta}_2 = \beta_2 + \sqrt{\frac{5}{4\pi}} \left[\frac{4}{7}\beta_2^2 + \frac{8}{15}\beta_3^2 \right]. \tag{2.3}
$$

Therefore, the quadrupole moment Q_2 as function of (β_2) and (β_2, β_3) reads as

$$
\begin{aligned}
Q_2(\beta_2, \beta_3) &= \frac{3}{\sqrt{(2\lambda+1)\pi}} Z R_0^\lambda \left\{ \beta_2 + \sqrt{\frac{5}{4\pi}} \left[\frac{4}{7}\beta_2^2 + \frac{8}{15}\beta_3^2 \right] \right\} \quad \text{and} \\
Q_2(\beta_2) &= \frac{3}{\sqrt{(2\lambda+1)\pi}} Z R_0^\lambda \left[\beta_2 + \sqrt{\frac{5}{4\pi}} \times \frac{4}{7}\beta_2^2 \right].
\end{aligned} \tag{2.4}
$$

Also, one can analyze the relevance of octupole deformation by taking difference of $Q_2(\beta_2, \beta_3)$ and $Q_2(\beta_2)$ terms, which depend directly on the β_3-deformation, as given below

$$Q_2(\beta_2, \beta_3) - Q_2(\beta_2) = \frac{3}{\sqrt{(2\lambda+1)\pi}} Z R_0^{\lambda} \left[\sqrt{\frac{5}{4\pi}} \times \frac{8}{15} \beta_3^2 \right]. \tag{2.5}$$

The Eqs. (2.1)-(2.5) define the intrinsic degrees of freedom for individual nuclei. For nuclei colliding in a plane, the related mathematical details will be discussed hereafter.

To study the formation and disintegration of compound nuclear system formed via heavy-ion induced reactions, different pairs of projectile-target (P-T) combinations, which can either be of spherical or deformed shapes, are taken into consideration. The geometrical representations for spherical-plus-spherical, spherical-plus-deformed and deformed-plus-deformed nuclei of P-T combinations are shown in Fig. 2.1.

For coplanar nuclei, the surface interactions take place at the minimum separation distance s_0, determined by variety of iterative methods [37–39]. From Fig. 2.1, one can clearly see that s_0 is parallel to the separation distance R(fm) between the centers of Nucleus I and Nucleus II. It is equal to the distance between the two surfaces of colliding nuclei facing each other along the collision axis, as given below

$$s_0 = R - X_1(\alpha_1, \theta_1) - X_2(\alpha_2, \theta_2). \tag{2.6}$$

In the above expression, the radius $X_i(\alpha_i, \theta_i)$ (here, i = 1, 2) is the projection of radius vector $R_i(\alpha_i)$ (Eq.(2.1)) over the collision axis. The projected radii $X_i(\alpha_i, \theta_i)$ as function of independent variables, i.e. θ_i (angle between collision and symmetry axes) and α_i angles, are different for spherical, quadrupole and octupole deformed shapes as depicted in Fig. 2.1. For deformed nuclei, the orientation of symmetry axis θ_i comes into existence and for a given value of θ_i, the value of α_i can be obtained by minimizing Eq.(2.6) with respect to α_1 and α_2 respectively for Nucleus I and II, as given below

$$\begin{aligned} \frac{\partial s_0}{\partial \alpha_1} &= \frac{\partial s_0}{\partial \alpha_2} = 0; \\ \Rightarrow \tan(\delta_1) = -\frac{R_1'(\alpha_1)}{R_1(\alpha_1)} \quad &\text{and} \quad \tan(\delta_2) = -\frac{R_2'(\alpha_2)}{R_2(\alpha_2)}. \end{aligned} \tag{2.7}$$

In the above expression, $R_i'(\alpha_i)$ is the first derivative of radius vector $R_i(\alpha_i)$ with respect to α_i.

With the detail of angles α_i and θ_i, one can obtain the radius of curvature $\bar{R}$ (the mean curvature radius) which describe the geometry of two colliding curved surfaces. The product of mean principal radii ($R_{i1}(\alpha_i)$ and $R_{i2}(\alpha_i)$) obtained for Nucleus I and Nucleus II give the inverse of square of mean curvature radius, as given below [37]

$$\begin{aligned} \frac{1}{\bar{R}^2} &= \left(\frac{R_{11}(\alpha_1)+R_{12}(\alpha_1)}{R_{11}(\alpha_1)R_{12}(\alpha_1)}\right) \times \left(\frac{R_{21}(\alpha_2)+R_{22}(\alpha_2)}{R_{21}(\alpha_2)R_{22}(\alpha_2)}\right), \\ \bar{R} &= \left[\left(\frac{R_{11}(\alpha_1)R_{12}(\alpha_1)}{R_{11}(\alpha_1)+R_{12}(\alpha_1)}\right) \times \left(\frac{R_{21}(\alpha_2)R_{22}(\alpha_2)}{R_{21}(\alpha_2)+R_{22}(\alpha_2)}\right)\right]^{1/2}. \end{aligned} \tag{2.8}$$

Note that, the derivation regarding the principal radii of curvature $R_{i1}(\alpha_i)$, $R_{i2}(\alpha_i)$ are provided in Appendixes A and B. The factor $\bar{R}$ gives the detail of nuclear geometry.

Based on the above said geometrical description for the two nuclear systems colliding in a close proximity region (of about 2 fm), many authors were able to evaluate the nucleus-nucleus interaction potential ($V_N(R)$), Coulomb potential ($V_C(R)$) as well as centrifugal potential ($V_\ell(R)$). The mathematical formulations related to $V_N(R)$, $V_C(R)$ and $V_\ell(R)$ potentials are discussed in the following sections.

2.3 Nuclear potential

As discussed in the Chapter 1, the nuclear force between two finite nuclei comes into existence within the range of few fermi scale. Many authors had established numerous mathematical formalisms for deriving the nuclear force in terms of potential energy as a function of separation distance between two nuclear systems [proximity potentials, Woods-Saxon potential, SEDF potential] [20]. Here, the nuclear potential energy is based on the "Proximity Force Theorem". On the basis of this theorem, the potential energy (the energy possessed by a nucleus relative to another one) defining the nuclear force among two gently curved surfaces is proportional to the interaction potential per unit area between the colliding nuclei, that is,

$$V_N(s) \propto \text{potential energy per unit area between curved objects},$$

$$= \quad 2\pi \times \text{geometrical factor} \times \text{universal function of separation distance.}$$
$$= \quad 2\pi \bar{R} \int_{s=s_0}^{\infty} e(s) ds. \tag{2.9}$$

In the above expression, the nuclear potential energy V_N is a function of separation distance s $(=R - X_1 - X_2$, already discussed) and the proportionality constant corresponds to 2π times the geometrical factor, defining the curved gap or crevice between two interacting nuclei in the proximity region. Important to mention that, the term interaction energy per unit area $e(s)$ is integrated over the distance from $s = s_0$ (minimum separation distance) to ∞. At large values of s or R (separation distance), the nuclear potential energy term reduces to zero which justifies the saturation property of the nuclear force.

The authors of Ref. [20] evaluated the term $e(s)$, in terms of the Universal function $\phi(s)$ which depends only on s, is given as follows

$$V_N(R) = 4\pi \bar{R} \gamma b \phi(s); \;\; 2\gamma b \phi(s) = \int e(s) ds. \tag{2.10}$$

As discussed in Chapter 1, the surface diffuseness (a) defined in terms of surface thickness term 't' (shown in Fig.1.3), corresponds to the distance at which nuclear density fall from 0.9 of central density (ρ_0) to 0.1 of ρ_0. The term 'b' also called as surface diffuseness is related to a, as [20] $t = 4a \log_e 3 \Rightarrow b = (\pi/\sqrt{3})a \approx 0.99$ fm.

Important to mention that, the effective interaction depends on the stiffness/softness of the colliding nuclei. Henceforth, the nuclear surface tension coefficient $\gamma(A_s)$ in MeVfm^{-2} has been introduced as a function of asymmetry parameter, $A_s(= (\frac{N-Z}{A}))$, as given below

$$\gamma(A_s) = \gamma_0[1 - k_s A_s^2] \;\; MeV fm^{-2}. \tag{2.11}$$

In the above relation of $\gamma(A_s)$, the values of surface energy constant γ_0=1.01734 and surface-asymmetry constant k_s=1.79 MeV/fm^{-2} have been obtained using the Lysekil mass formula [40]. Note that, the relevant information related to the mean curvature radius or radius of curvature $\bar{R}$ is discussed in the above sections and Appendixes A and B of this chapter.

2.3.1 Phenomenological model based potentials

According to the notion of Proximity Force Theorem [20], the nuclear proximity potential V_N of Eq.(2.10) is directly proportional to the Universal function $\phi(s)$, which was evaluated by different methods [41–49]. In Ref. [20], J. Blocki and his collaborators had given a simple analytical cubic-exponential polynomial $\phi(s)$, that tends to zero at ξ_0=2.54 fm (for convenience see Fig.4 of [20]). The cubic-exponential function $\phi(s)$ as a function of s is given as

$$\phi(s) = \begin{cases} -\frac{1}{2}(s-\xi_0)^2 - 0.0852(s-\xi_0)^3; s \leq 1.2511 \ \text{fm} \\ \\ -3.437 \exp\left(-\frac{s}{0.75}\right); s > 1.2511 \ \text{fm} \end{cases}. \tag{2.12}$$

Important to mention that, in the above polynomial relation, the independent variable s is defined in units of surface diffuseness factor b. In addition to above, another proximity potential, i.e. Prox88 [48, 50] a modified version of Prox77, is taken into account, in order to address the fusion hindrance. The modification in Prox77 has been done by altering the values of coefficients $\gamma_0(= 1.2496 \text{ MeVfm}^{-2})$ and $k_s(= 2.3)$, which in turn, lowers the barrier height (to be discussed in Chapter 6).

Apart from the above discussed nuclear potential developed on the basis of phenomenological model of Proximity Theorem [20], the energy density formalism gives an alternative method to understand the heavy-ion collisions by introducing the Skyrme force parameters within the Hamiltonian density functions [2, 51, 52].

2.3.2 Skyrme Energy Density Formalism

With the advent of Skyrme force parameters, the researchers had employed the Skyrme force parameters within the energy density formalism as an algebraic function of the nucleon ρ, kinetic energy τ and spin-orbit $\vec{J}$ density terms. The expectation value of total energy E comprised of total kinetic and potential energies can be written in terms of Hamiltonian density functions [51]

$$\begin{aligned} E &= \langle \phi, (T+V)\phi \rangle \\ &= \sum_i \left\langle i|\frac{p^2}{2m}|i\right\rangle + \frac{1}{2}\sum_{ij} \langle ij|\bar{v}_{12}|ij\rangle + \frac{1}{6}\sum_{ijk} < ijk|v_{123}|ijk > \end{aligned}$$

$$= \int H(\vec{r})d^3r = \int \left[\frac{\hbar^2}{2m}\tau(\vec{r}) + H_0(\vec{r}) + H_1(\vec{r}) + H_2(\vec{r}) + H_3(\vec{r}) + H_{so}(\vec{r})\right] d^3r. \tag{2.13}$$

In the above expression, the term $\tau(\vec{r})$ refers to the kinetic energy density term and $\frac{\hbar^2}{2m}$ has a constant value of 20.7784 MeVfm^2. Further, the most common Hamiltonian terms that is,

$$\begin{aligned} H_0(\vec{r}) &- \text{zero-range term}, \\ &\propto t_0 \text{ and } x_o, \\ H_1(\vec{r}) \,\&\, H_2(\vec{r}) &- \text{exchange term}, \\ &\propto t_1, t_2, x_1 \text{ and } x_2, \\ H_3(\vec{r}) &- \text{density-dependent term}, \\ &\propto \alpha, t_3 \text{ and } x_3, \\ H_{so}(\vec{r}) &- \text{spin-orbit density term}, \\ &\propto W_0. \end{aligned}$$

Here, the zero-range, exchange, density-dependent and spin-orbit density terms are proportional to the Skyrme force parameters obtained via addressing the nuclear properties, e.g. binding energy, nuclear radius, incompressibility etc. [53–59]. The related expressions for the above said Hamiltonian terms (H_0, H_1, H_2, H_3 and H_{so}) are provided in Table 2.1 and the parameters correspond to the SIII Skyrme force [53]. The left column of this table defines the Hamiltonian terms for the nuclei colliding at a finite distance and the right column is for the infinitely separated nuclei.

There are different versions of Skyrme forces [55, 56], which have been evaluated with different sets of parameters and additional Hamiltonian terms defining various nuclear properties (e.g. iso-spin effect, asymmetry factor, tensor coupling effect, etc.) of nuclei which were not introduced in earlier Skyrme forces. With such modifications in $H(r)$, the authors had analyzed corresponding effect on the fusion barrier characteristics, and subsequently on the fusion-fission cross-sections [60, 61]. In the present thesis, the considered Skyrme forces are SIII [53], SLy4 [54], SSk [56] and GSkI [55]. These Skyrme forces cover a wide range barrier characteristics, which in turn, show corresponding effect on the fusion and decay dynamics of excited CN.

Colliding nuclei at finite distance	Infinitely Separated nuclei
$H(\rho,\tau,\vec{J})$=	$H_i(\rho_i,\tau_i,\vec{J_i})$=
Kinetic energy-density term, K	
$\frac{\hbar^2}{2m}\tau(\rho)$	$\frac{\hbar^2}{2m}\tau_i(\rho_i)$
Zero-range term, H_0	
$\frac{1}{4}t_0\left[(2+x_0)\rho^2-(2x_0+1)(\rho_n^2+\rho_p^2)\right]$	$\frac{1}{4}t_0\left[(2+x_0)\rho_i^2-(2x_0+1)(\rho_{in}^2+\rho_{ip}^2)\right]$
Effective-mass term, H_1	
$\frac{1}{8}\left[t_1(2+x_1)+t_2(2+x_2)\right]\tau\rho$ -$\frac{1}{8}\left[t_1(2x_1+1)-t_2(2x_2+1)\right]\left[\sum_{q=n,p}\rho_q\tau_q\right]$	$\frac{1}{8}\left[t_1(2+x_1)+t_2(2+x_2)\right]\tau_i\rho_i$ -$\frac{1}{8}\left[t_1(2x_1+1)-t_2(2x_2+1)\right]\left[\sum_{q=n,p}\rho_{iq}\tau_{iq}\right]$
Finite-range term, H_2	
$\frac{1}{32}\left[3t_1(2+x_1)-t_2(2+x_2)\right](\nabla\rho)^2-$ $\frac{1}{32}\left[3t_1(2x_1+1)+t_2(2x_2+1)\right]$ $\times\left[(\nabla\rho_n)^2+(\nabla\rho_p)^2\right]$	$\frac{1}{32}\left[3t_1(2+x_1)-t_2(2+x_2)\right](\nabla\rho_i)^2-$ $\frac{1}{32}\left[3t_1(2x_1+1)+t_2(2x_2+1)\right]$ $\times\left[(\nabla\rho_{in})^2+(\nabla\rho_{ip})^2\right]$
Density-dependent term, H_3	
$\frac{t_3}{24}\rho^\alpha\left[(2+x_3)\rho^2-(2x_3+1)(\rho_n^2+\rho_p^2)\right]$	$\frac{t_3}{24}\rho_i^\alpha\left[(2+x_3)\rho_i^2-(2x_3+1)(\rho_{in}^2+\rho_{ip}^2)\right]$
Spin-orbit term, H_{so}	
-$\frac{W_0}{2}\left[\rho\nabla\cdot\vec{J}+\sum_{q=n,p}\rho_q\nabla\cdot\vec{J_q}\right]$	-$\frac{W_0}{2}\left[\rho_i\nabla\cdot\vec{J_i}+\sum_{q=n,p}\rho_{iq}\nabla\cdot\vec{J_{iq}}\right]$

Table 2.1: The detail of Hamiltonian density functions, which are proportional to the Skyrme force parameters (t_j, x_j, α and W_0; $j = 0-3$), is given for the compound nuclear system and individual nuclei ($i = 1, 2$ stand respectively for Nucleus I and Nucleus II).

Further, within the framwork of energy density formalism [1], one can obtain the interaction energy per unit area $e(s)$ (as defined in Eq.(2.10)) by calculating the expectation energy *E(R)* of colliding nuclei at a finite separation distance R and the energy of individual nuclei (separated by infinite distance), as given below

$$E(R)-E(\infty)=e(r \text{ or } s)=\int[H(\rho,\tau,\vec{J})-H_1(\rho_1,\tau_1,\vec{J_1})-H_2(\rho_2,\tau_2,\vec{J_2})]ds. \qquad (2.14)$$

Now, one can substitute the interaction energy relation obtained from Skyrme Hamiltonian function of Eq.(2.14) in Eq.(2.10). Subsequently, one can have a final relation of nucleus-nucleus potential derived using the Skyrme Energy Density Formalism (SEDF), as given below

$$V_N(R)=2\pi\bar{R}\int_s^\infty\{H(\rho,\tau,\vec{J})-H_1(\rho_1,\tau_1,\vec{J_1})-H_2(\rho_2,\tau_2,\vec{J_2})\}ds. \qquad (2.15)$$

From the above relation, it is clear that, the Hamiltonian functions which are proportional to the Skyrme force parameters are function of nuclear density ρ, kinetic energy density τ and spin-orbit density $\vec{J}$ terms. The latter terms that is τ and $\vec{J}$ have been derived using the extended Thomas-Fermi approach [62, 63].

In general, the average kinetic energy term for the number of nucleons residing within a volume of few fm^3 can be defined in terms of density, as given below

$$\begin{aligned} E_{avg} &= \frac{3}{5} \times \text{Fermi Energy}, \\ &= \frac{3}{5}\frac{\hbar^2}{2m}(3\pi^2\rho)^{2/3}. \end{aligned} \tag{2.16}$$

Further, the kinetic-energy density τ as a function of density ρ can be written as

$$\begin{aligned} \frac{\hbar^2}{2m}\tau(\rho) &= E_{avg} \times \rho, \\ &= \frac{\hbar^2}{2m}\left[\frac{3}{5}(3\pi^2\rho)^{2/3}\right] \times \rho = \frac{3}{5}(3\pi^2)^{2/3}\rho^{5/3}. \end{aligned} \tag{2.17}$$

With the use of $\tau(\rho)$ [Eq.(2.17)], the researchers were not able to define a proper profile of $V_N(R)$. Henceforth, there is a requirement of some correction terms, which had been introduced using the extended Thomas-Fermi approach in [64], given below

$$\begin{aligned} \tau_q(\rho_q) &= \frac{3}{5}(3\pi^2)^{2/3}\rho_q^{5/3} + \frac{1}{36}\frac{(\vec{\nabla}\rho_q)^2}{\rho_q} + \frac{1}{3}\Delta\rho_q + \frac{1}{6}\frac{\vec{\nabla}\rho_q \cdot \vec{\nabla}f_q}{f_q} \\ &+ \frac{1}{6}\frac{\rho_q\Delta f_q}{f_q} - \frac{1}{12}\rho_q\left(\frac{\vec{\nabla}f_q}{f_q}\right)^2; \text{ here, } q = n \text{ or } p. \end{aligned} \tag{2.18}$$

In Eq.(2.18), the term $\tau_q(\rho_q)$ is defined as the kinetic energy density function of nucleon density (ρ_q). Here, the subscripts $q = n$ and p stand for the neutron and proton, respectively. In the above expression, the term f_q is called as the effective-mass form factor and determined as [65]

$$\begin{aligned} f_q &= \left|\frac{m}{m^*}\right| = \frac{2m}{\hbar^2}\frac{\partial E(R)}{\partial \tau_q}, \\ f_q &= 1 + \frac{2m}{\hbar^2}\left[\frac{1}{4}\left(t_1 + \frac{t_1x_1}{2}\right) + \frac{1}{4}\left(t_2 + \frac{t_2x_2}{2}\right)\right]\rho(r) - \\ &\quad \frac{2m}{\hbar^2}\left[\frac{1}{4}\left(t_1x_1 + \frac{t_1}{2}\right) - \frac{1}{4}\left(t_2x_2 + \frac{t_2}{2}\right)\right]\rho_q(r). \end{aligned} \tag{2.19}$$

Further, the interaction potential obtained due to the orbital- and spin-angular momenta of colliding nuclei involve the spin-orbit density term $\vec{J}$ (and $\vec{J}_q$), which was further obtained for the second and higher order of $\hbar$ as a function of nucleus and nucleon densities, i.e. ρ and ρ_q [64]. The term $\vec{J}$ (and $\vec{J}_q$) for higher order of $\hbar$ has very negligible influence. Therefore, the second-order spin-orbit density term $\vec{J}_q$ is given as

$$J_q(\rho_q) = -\frac{2m}{\hbar^2}\frac{W_0}{2}\left(\frac{\rho_q \nabla(\rho + \rho_q)}{f_q}\right). \tag{2.20}$$

In Eqs.(2.18) and (2.20), the terms τ_q and $\vec{J}_q$ are kinetic energy and spin-orbit density terms, respectively, of nucleons. Further, to obtain the total value of τ and $\vec{J}$ for the compound nuclear system, the nuclear densities of colliding nuclei can be added in different manners, as discussed below:

- **Sudden density approximation:** One can obtain the $\tau(\rho)$ and $\vec{J}(\rho)$ terms for the compound nuclear system as [3]

$$\begin{aligned} \tau(\rho) &= \tau_n(\rho_n = \rho_{n_1} + \rho_{n_2}) + \tau_p(\rho_p = \rho_{p_1} + \rho_{p_2}) \\ \vec{J}(\rho) &= \vec{J}_n(\rho_n = \rho_{n_1} + \rho_{n_2}) + \vec{J}_p(\rho_p = \rho_{p_1} + \rho_{p_2}). \end{aligned} \tag{2.21}$$

- **Frozen density approximation:** In this case, the $\tau(\rho)$ and $\vec{J}(\rho)$ terms for the compound nuclear system are obtained as [3]

$$\begin{aligned} \tau(\rho) &= \tau_1(\rho_1 = \rho_{n_1} + \rho_{p_1}) + \tau_2(\rho_2 = \rho_{n_2} + \rho_{p_2}) \\ \vec{J}(\rho) &= \vec{J}_1(\rho_1 = \rho_{n_1} + \rho_{p_1}) + \vec{J}_2(\rho_2 = \rho_{n_2} + \rho_{p_2}). \end{aligned} \tag{2.22}$$

In the above equations, the nucleon densities of individual nuclei ($\rho_{n_i \,\mathrm{or}\, p_i}$) and of compound nucleus nucleon density (ρ_q) are related as

$$\begin{aligned} \rho_{n_i} &= \frac{N_i}{A_i}\rho_i(r); \;\; \rho_{p_i} = \frac{Z_i}{A_i}\rho_i(r), \\ \rho(r) &= \rho_1(r) + \rho_2(r). \end{aligned} \tag{2.23}$$

Here, N_i, Z_i and A_i are the number of neutrons, protons and total nucleons inside a nucleus.

- **Relaxed-density approach:** In this approach, the ion-ion interaction potential, which was obtained in the framework of the Extended Thomas-Fermi (ETF) approach of energy density function theory, under relaxed density approximation [9], is parameterized in the Woods-Saxon form as follows:

$$V_N(R) = \frac{V_0}{1 + \exp\left[(R - R_t)/d\right]}, \tag{2.24}$$

where $V_0 = v_1 C + v_2 C^{1/2}$ is the potential strength in MeV, $v_1 = -27.190$ MeV fm^{-1}, $v_2 = -0.93009$ MeV fm$^{-1/2}$, $d = d_1 + d_2/C$ is the diffuseness parameter in fm, $d_1 = 0.78122$ fm, $d_2 = -0.20535$ fm^2, and $C = R_1 R_2/R_t$ fm. Here, R_i's, the radii of spherical nuclei, are expressed as follows:

$$R_i = 1.2536 A_i^{1/3} - 0.80012 A_i^{-1/3} - 0.0021444/A_i, \tag{2.25}$$

As discussed in the earlier, the nuclear density as a radial function can be obtained using different mathematical approaches. In the present thesis, the two- and three-parameter density functions have been taken into account and are given below.
The 2pF density function reads as follows [22]

$$\rho_i(r_i) = \rho_{0i}\left[1 + \exp\left(\frac{r_i - R_{0i}}{a_i}\right)\right]^{-1}, -\infty \leq r \leq \infty. \tag{2.26}$$

The central density term (ρ_{0i}) of Eq.(2.26) is a normalized term and calculated by the means of integral of nuclear density [22]

$$4\pi \int_0^{\infty} \rho(r) r^2 dr = 1. \tag{2.27}$$

The central density term (ρ_{0i}) comes out to be [22]

$$\rho_{0i} = \frac{3A_i}{4\pi R_{0i}^3}\left[1 + \frac{\pi^2 a_i^2}{R_{0i}^2}\right]^{-1}. \tag{2.28}$$

The values of 2pF density parameters, i.e. spherical half-density radius R_{0i} in fm (also employed in Eq.(2.1)) and surface thickness a_i (in fm), are provided in [66, 67] for mass region A = 4 - 238. Further, the polynomials of these parameters are referred from Ref. [29]

and are obtained by fitting the available experimental data [66,67]

$$\begin{aligned} R_{0i} &= 0.9543 + 0.0994A_i - 9.8851 \times 10^{-4}A_i^2 + 4.8399 \times 10^{-6}A_i^3 - 8.4366 \times 10^{-9}A_i^4, \\ a_i &= 0.3719 + 0.0086A_i - 1.1898 \times 10^{-4}A_i^2 + 6.1678 \times 10^{-7}A_i^3 - 1.0721 \times 10^{-9}A_i^4. \end{aligned} \tag{2.29}$$

The 3pF density function is given as [67]

$$\rho_i(r_i) = \rho_{0i}\left(1 + \frac{w_i r_i^2}{R_{0i}^2}\right)\left[1 + \exp\left(\frac{r_i - R_{0i}}{a_i}\right)\right]^{-1}. \tag{2.30}$$

Here, the central density term ρ_{0i} of the above density function is normalized using Eq.(2.27) and calculated by following the approach of Ref. [29], given as

$$\rho_{0i} = \frac{3A_i}{4\pi R_{0i}^3}\left[1 + \frac{3w_i}{5} + (1 + 2w_i)\frac{\pi^2 a_i^2}{R_{0i}^2} + \frac{7}{5}w_i\frac{\pi^4 a_i^4}{R_{0i}^4}\right]^{-1}. \tag{2.31}$$

The values of 3pF density parameters, R_{0i}, a_i and wine-bottle parameter w_i, are extracted from the data given in Ref. [67] for mass region A = 14 - 166. Further, the polynomials of these parameters are obtained by fitting the corresponding data, and read as [10]

$$\begin{aligned} R_{0i} &= 1.56652 + 0.07285A_i - 5.3503 \times 10^{-4}A_i^2 + 1.74857 \times 10^{-6}A_i^3 - 1.23798 \times 10^{-9}A_i^4, \\ a_i &= 0.33614 + 0.01938A_i - 4.79946 \times 10^{-4}A_i^2 + 4.25566 \times 10^{-6}A_i^3 - 1.23125 \times 10^{-8}A_i^4, \\ w_i &= 0.05658 - 0.01174A_i + 1.75649 \times 10^{-4}A_i^2 - 8.96765 \times 10^{-7}A_i^3 + 1.7808 \times 10^{-9}A_i^4. \end{aligned} \tag{2.32}$$

Here, w_i is a dimensionless quantity.

The 3pG density function [67] is given as follows

$$\rho_i(r_i) = \rho_{0i}\left(1 + \frac{w_i r_i^2}{R_{0i}^2}\right)\left[1 + \exp\left(\frac{r_i^2 - R_{0i}^2}{a_i^2}\right)\right]^{-1}. \tag{2.33}$$

The central density term (ρ_{0i}) of the above density function is normalized upto higher orders using Eq.(2.27) and calculated for the first time in the present work, as follows

$$\rho_{0i} = \frac{A_i}{\pi^{3/2}a_i^3}[(0.765 + 0.604k) + \frac{R_{0i}^2}{a_i^2}(0.604 + 0.766k) + \frac{R_{0i}^4}{a_i^4}(0.1901 + 0.302k)$$

$$+\frac{R_{0i}^6}{a_i^6}(0.0198+0.0634k)-\frac{R_{0i}^8}{a_i^8}(0.00365-0.00495k)]^{-1}; \tag{2.34}$$
$$k=\frac{3}{2}w_i\left(\frac{a_i^2}{R_{0i}^2}\right).$$

The parameters of 3pG density distribution are provided in Ref. [67] for mass region A = 28-209. Further, the polynomials of these parameters are obtained by fitting the related experimental data, and is given as follows [10]

$$\begin{aligned}
R_{0i} &= -0.64823+0.13377A_i-0.00148A_i^2+8.47357\times10^{-6}A_i^3-1.76632\times10^{-8}A_i^4,\\
a_i &= 1.95948+0.00194A_i+1.58635\times10^{-4}A_i^2-1.55798\times10^{-6}A_i^3+4.09371\times10^{-9}A_i^4,\\
w_i &= 0.02242+0.00969A_i-1.04736\times10^{-4}A_i^2+4.44011\times10^{-7}A_i^3-5.94716\times10^{-10}A_i^4.
\end{aligned} \tag{2.35}$$

So far, the methods adopted to derive the nucleus-nucleus interaction potential and its ingredient terms have been discussed. In the upcoming sections, the other contributing potentials (i.e. Coulomb and centrifugal potentials) of the total interaction potential along with the models used to calculate the fusion and decay cross-sections are discussed.

2.4 Coulomb and centrifugal potentials

In general, it is said that the electrostatic or Coulomb potential energy ($V_C(R)$) of a point charged particle (or nucleus) is given as: $V_C(R) \propto e^2$ and $1/R$. For the system of charged particles, one can write it as $V_C(R) \propto \sum_i \frac{e^2}{|\vec{r}-\vec{r_i}|}$. In the case of nuclear collision process, we have two-body system, in which the two nuclei are separated by a distance R. There are Z_1 (and Z_2) number of charged particles of Nucleus I (and Nucleus II), which are the main cause of Coulomb repulsion. Therefore, for charge distribution, the Coulomb potential energy can be read as [68, 69]

$$V_C(R)=\int d\vec{r_1}d\vec{r_2}\frac{e^2}{|\vec{R}+\vec{r_2}-\vec{r_1}|}\rho_1(\vec{r_1})\rho_2(\vec{r_2}). \tag{2.36}$$

On the basis of above formula of Coulomb potential defined for two nuclear systems, the authors have obtained a simple expression for $V_C(R)$, with the use of Fourier transform equations ([69]; references therein). Note that, the expression derived involve the intrinsic properties of nuclear shape that is deformation and orientation degrees of freedom, and consequently categorised the potential in different terms, as given below [70]

$$V_C(R) = V_C(R, \beta_\lambda, \theta) = V_0(R) + V_{i1}(R, \beta_\lambda, \theta_i) + V_{i2}(R, \beta_\lambda, \theta_i) + ... \tag{2.37}$$

If one considers the axial symmetric shapes in heavy-ion induced reactions, then the first three terms are taken into considerations and the rest are opted out [69, 70]. The mathematical relations related to these terms are given in the following:

$$\begin{aligned} V_0(R) &= \frac{Z_1 Z_2 e^2}{R}, \\ V_{i1}(R, \beta_\lambda, \theta_i) &= Z_1 Z_2 e^2 \sqrt{\frac{9}{4\pi}} \sum_\lambda \frac{R_i^\lambda}{R^{\lambda+1}} \beta_{\lambda i} P_\lambda(\cos\theta_i), \\ V_{i2}(R, \beta_\lambda, \theta_i) &= Z_1 Z_2 e^2 \left(\frac{3}{7\pi}\right) \sum_{\lambda,i} \frac{R_i^\lambda}{R^{\lambda+1}} [\beta_{\lambda i} P_\lambda(\cos\theta_i)]^2. \end{aligned} \tag{2.38}$$

Substitute Eq.(2.38) in Eq.(2.36), we get

$$V_C(R) = \frac{Z_1 Z_2 e^2}{R} + \begin{cases} Z_1 Z_2 e^2 \sum_\lambda \left(\frac{R_2^\lambda(\alpha_2)}{R^{\lambda+1}}\right) \beta_\lambda Y_\lambda^{(0)}(\theta_2) \times \left[\frac{3}{2\lambda+1} + \left(\frac{12}{7(2\lambda+1)}\right) \beta_\lambda Y_\lambda^{(0)}(\theta_2)\right], \\ \qquad\qquad \text{for spherical-deformed combination} \\ Z_1 Z_2 e^2 \sum_{\lambda,i} \frac{R_i^\lambda}{R^{\lambda+1}} \left[\sqrt{\frac{9}{4\pi}} P_\lambda(\cos\theta_i) + \left(\frac{3}{7\pi}\right) [\beta_{\lambda i} P_\lambda(\cos\theta_i)]^2\right]. \\ \qquad\qquad \text{for deformed-deformed combination} \end{cases} \tag{2.39}$$

In the above expression, the multipole order λ has been taken up to 3, i.e. $\lambda = 2, 3$. In the present work, the relevance of spherical, quadrupole ($\beta_2^\pm$) and octupole ($\beta_3^\pm$) deformed shapes in nuclear fusion-fission dynamics has been discussed.

Furthermore, the centrifugal potential ($V_\ell(R)$) of repulsive behavior comes into existence due to the rotational motion of the colliding nuclear partners. In heavy-ion induced reactions, the compound nuclear system formed in a very high excited state possesses large value of angular momentum. Here, the total angular momenta (L) of the excited CN is given as L = momentum $\times$ distance = $\sqrt{\ell(\ell+1)\hbar^2}$. Therefore, the potential energy as a form of rotational kinetic energy is given as

$$\begin{aligned} V_\ell(R) &= \frac{1}{2}\mu v^2; \\ &= \frac{1}{2} \times \frac{L^2}{\mu R^2}, \\ \Rightarrow V_\ell(R) &= \frac{\ell(\ell+1)\hbar^2}{2I}. \end{aligned} \tag{2.40}$$

In the above expression, $I = \mu R^2$ defines the moment of inertia for non-sticking configuration of two interacting nuclei. On the other hand, for sticking case, $I = \mu R^2 + \frac{2}{5}m\sum_{i=1,2} A_i R_i^2(\alpha_i, T)$. Here, μ is the reduced-mass of two-body system and given as $\mu = \frac{A_1 A_2}{A_1+A_2} \times$ one atomic mass unit; A_1 and A_2 are the atomic mass numbers of Nucleus I and Nucleus II, respectively. Note that, in the present thesis, the non-sticking case has been considered.

On combining Eqs.(2.10), (2.39) and (2.40), one can obtain the total interaction potential $V_T(R)$ between two nuclei, which are separated by a distance R in fm units, as given below

$$V_T(R) = V_N(R) + V_C(R) + V_\ell(R). \tag{2.41}$$

With the variation of separation distance, from infinity to the closest distance of approach, the total interaction potential ($V_T(R)$) represents a collective effect of Nuclear, Coulomb and centrifugal potentials. In other words, at relatively smaller distance that is $R < R_t = R_1+R_2$ called as the overlapping region, a deep pocket of the total potential comes into picture. In this region, the formation of an excited Compound nuclear system becomes possible. As one moves ahead, due to the prominent effect of Coulomb and centrifugal potentials in comparison to the nuclear potential, there is a rise in $V_T(R)$ at fixed point, which is called as "**Coulomb barrier height**". In the fusion-fission nuclear mechanisms, the nuclear surface interactions (which come after R_t, i.e. $R > R_t$) take place, henceforth, the detail of Coulomb barrier height and related terms that is barrier position and barrier curvature help in estimating the fusion and fission cross-sections, with the effect of energy/temperature, angular momenta, deformations and orientation degrees of freedom, where ever applicable. It has been noted down that, the Coulomb barrier region of the total interaction potential analogous to the inverted Harmonic Oscillator (HO) function, which defines the Harmonic oscillation of mass attached to a spring. From this analysis, one can obtain the angular frequency, ω and subsequently the energy term $\hbar\omega$ which contains the information of barrier curvature.

$$\begin{aligned}
V_T(R)|_{R=R_a}^{R=R_b} &= \frac{1}{2}\mu\omega^2 R^2, \text{ The Potential energy of harmonic oscillator motion} \\
\frac{dV_T(R)}{dR} &= \mu\omega^2 R, \text{ First derivative of } V_T(R) \text{ w.r.t } R \\
\frac{d^2V_T(R)}{dR^2} &= \mu\omega^2, \text{ Second derivative of } V_T(R) \text{ w.r.t } R \\
\Rightarrow \omega &= \left[\frac{1}{\mu}\frac{d^2V_T(R)}{dR^2}\right]^{1/2}.
\end{aligned} \tag{2.42}$$

Therefore, the energy of inverted Harmonic oscillator ($\hbar\omega$) at the barrier position (R_B) which is obtained corresponding to the barrier height (V_B) is given as

$$\hbar\omega_B = \hbar\left[\frac{1}{\mu}\left|\frac{d^2V_T(R)}{dR^2}\right|_{R=R_B}\right]^{1/2}. \tag{2.43}$$

Here, $\hbar\omega_B$ defines the barrier curvature energy at a fixed point i.e. R_B.

2.5 Collective effect of barrier characteristics

On the basis of the scattering and partial wave theory [71], the formula was given to calculate the total reaction cross-section, as given below

$$\begin{aligned}
\sigma &= \int |f(\theta)|^2 d\Omega = \frac{4\pi}{k^2}\sum_{\ell=0}^{\ell_{max}}(2\ell+1)|f_\ell(k)|^2, \\
&= \frac{\pi}{k^2}\sum_{\ell=0}^{\ell_{max}}(2\ell+1)\left|1-\eta_\ell^2\right|.
\end{aligned} \tag{2.44}$$

In the above equation, $|f(\theta)|$ is the scattering amplitude, $k = \sqrt{\frac{2\mu E_{c.m.}}{\hbar^2}}$ and ℓ - the quantum number of partial wave. Based on the above relation (Eq.(2.44)), Wong had given a simple analytical expression by approximating the barriers of inverted Harmonic oscillator (or parabolic approximation) [11]. As a consequence, the formula for determining the fusion reaction cross-sections is given as follows:

$$\begin{aligned}\sigma_{fus}(E_{c.m.}) &= \frac{\pi}{k^2}\sum_{\ell=0}^{\ell_{max}}\frac{2\ell+1}{1+\exp\left[\frac{2\pi}{\hbar\omega_B^\ell}(V_B^\ell - E_{c.m.})\right]}, \\ &= \frac{\pi}{k^2}\sum_{\ell=0}^{\ell_{max}}(2\ell+1)T_\ell(E_{c.m.}). \end{aligned} \tag{2.45}$$

Here, V_B^ℓ signifies the barrier height corresponding to the ℓ^{th}-partial wave and reads as $V_B^\ell = V_B^{\ell=0} + \frac{\hbar\ell(\ell+1)}{2\mu R_B^2}$. Further, $T_\ell(E_{c.m.})$ is the tunneling/penetration probability as a function of barrier characteristics and incident energy obtained using the Hill-Wheeler approximation [72]. Important to mention that, in the present thesis, the values of ℓ_{max} are obtained using the sharp cut-off model [73] for the energies above the Coulomb barrier, and extended for the below barrier energies.

In the above relation, the summation is taken up to ℓ_{max} values. If one integrates the relation for $\ell \to \infty$ and consider the following approximation for barrier curvature: $\hbar\omega_B^\ell \approx \hbar\omega_B^{\ell=0}$, the Eq.(2.45) reduces to

$$\sigma_{fus}(E_{c.m.}) = \frac{R_B^2\hbar\omega_B}{2E_{c.m.}}\ln\left[1+\exp\left(\frac{2\pi}{\hbar\omega_B}(E_{c.m.} - V_B)\right)\right]. \tag{2.46}$$

Further, to observe the effect of deformation and orientation degrees of freedom, the Wong formula (Eq.(2.46)) of fusion cross-sections [$\sigma_{fus}(E_{c.m.})$ or $\sigma_{fus}(E_{c.m.},\theta)$] can be integrated over θ_i (0^o to π or 180^o) orientations, as given below

$$\sigma_{fus}^{int}(E_{c.m.}) = \int_{\theta_i}\sigma_{fus}(E_{c.m.},\theta_i)\sin\theta_i d\theta_i;\ \ \text{here,}\ \ i=1,2. \tag{2.47}$$

2.6 Collective clusterization approach

After the formation of Compound nuclear system in an excited state, the heavy-mass CN disintegrates due to large values of angular momenta, energy/temperature, charge repulsion, etc. (generally into the binary fragments), which may correspond to the Evaporation residue (ER), intermediate-mass fragment (IMF), heavy-mass fragment (HMF) and fission fragments. In the present thesis, I have discussed about the nuclear fission phenomena, which occurs at the low energy regime.

In order to analyze the de-excitation of excited CN into binary fragments, the mass and charge distributions of heavy-mass CN are studied within the framework of Quantum Mechanical Fragmentation Theory (QMFT) [13, 14] by solving the Schrodinger equation as a function of mass- $\left(\eta_A = \left|\frac{A_1-A_2}{A_1+A_2}\right|\right)$ and charge-asymmetry $\left(\eta_Z = \left|\frac{Z_1-Z_2}{Z_1+Z_2}\right|\right)$ co-ordinates, as given below

$$\left\{-\frac{\hbar^2}{2\sqrt{B_{\eta_\xi\eta_\xi}}}\frac{\partial}{\partial\eta_\xi}\frac{1}{\sqrt{B_{\eta_\xi\eta_\xi}}}\frac{\partial}{\partial\eta_\xi}+V_R(\eta_\xi,T)\right\}\psi^\nu(\eta_\xi)=E^\nu\psi^\nu(\eta_\xi). \tag{2.48}$$

Here, $\xi = A$ for mass-dispersion and $\xi = Z$ for charge-dispersion. ν represents the quantum number related to the excited state level of compound nuclear system. In the solution of above Schrodinger equation, one can obtain the preformation probability P_0 as a function of mass-asymmetry parameter η_A [13],

$$P_0(\eta_A) = |\psi(\eta(A_i))|^2\sqrt{B_{\eta_A\eta_A}}\frac{2}{A_{CN}}. \tag{2.49}$$

On the other hand, the P_0 as a function of charge-asymmetry parameter η_Z reads as [14]

$$P_0(\eta_Z) = |\psi(\eta(Z_i))|^2\sqrt{B_{\eta_Z\eta_Z}}\frac{2}{Z_{CN}}. \tag{2.50}$$

In Eqs.(2.49) and (2.50), the states $\psi(\eta(A_i))$ and $\psi(\eta(Z_i))$, respectively, are the vibrational states. The possible outcomes related to the excitations of higher vibrational states are considered by assuming them as Boltzmann-like wave function, such as

$$|\psi|^2 = \sum_{\nu=0}^{\infty}|\psi^\nu|^2\exp(E^\nu/T). \tag{2.51}$$

Here, ν = 0, 1, 2, 3,.... correspond to different states.

In the above equations, $B_{\eta_A\eta_A}$ and $B_{\eta_Z\eta_Z}$ are the smooth hydro-dynamical parameters, for more details see [74].

Further, the preformed fragments inside the potential pocket starts penetrating through the first classical turning point, i.e. $R = R_a = R_1(\alpha_1,T) + R_2(\alpha_2,T) + \triangle R$, and terminates through the second turning point R_b, such that $V(R_a) = V(R_b)$, for clarity see Fig.2.2, where the total interaction potential $V_T(R)$ is plotted as a function of separation distance. The idea of introducing neck-length parameter $\triangle R$ in the above relation, which is introduced

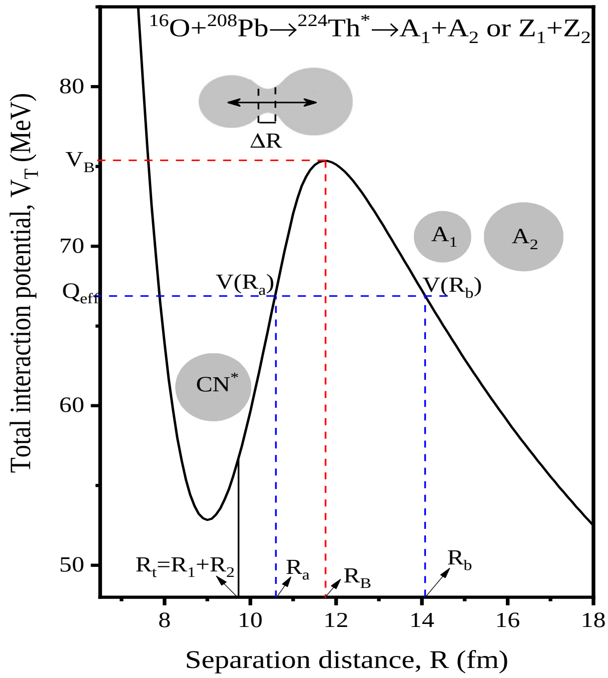

Figure 2.2: The variation of total interaction potential V_T (MeV) as a function of separation distance R (fm) between the colliding nuclear partners is shown for $^{16}O+^{208}Pb \rightarrow ^{224}Th^*$ reaction [32]. Here, $R_a = R_1(\alpha_1, T) + R_2(\alpha_2, T) + \triangle R$ defines the first turning point.

in the DCM based calculations [75–77], is similar to that of saddle- [78, 79] and scission-point [80] statistical fission model. The permissible value of $\triangle R$ lies within the nuclear proximity range of about 2 fm, since the surface interaction between two fragments can take place around this range of $\triangle R$ to experience the nuclear force.

With the knowledge of turning path or points R_a, the term 'Penetration probability' P has been calculated using the WKB approximation and given as [81]

$$P = \exp\left[-\frac{2}{\hbar}\int_{R_a}^{R_b}\{2\mu[V(R) - Q_{eff}]\}^{1/2} dR\right]. \tag{2.52}$$

In the above equation, 'Q_{eff}' is the effective Q-value of the decay channel.

Using Eqs.(2.49) or (2.50) and (2.52), one can calculate the decay cross-sections ($\sigma_{decay}(A_1, A_2)$) of fragments (A_1, A_2) emitting from excited CN, as given below [82, 83]

$$\sigma_{decay}(A_1, A_2) = \frac{\pi}{k^2}\sum_{\ell=0}^{\ell_{max}}(2\ell + 1)P_0 P. \tag{2.53}$$

Important to mention that, for fragments decaying from CN in the symmetric and asymmetric region, the mass and charge numbers of fission fragments come within the ranges

$A_2 = \frac{A_{CN}}{2} \pm 35$ and $Z_2 = \frac{Z_{CN}}{2} \pm 15$ [32], respectively. Here, A_{CN} and Z_{CN} are the mass and charge numbers of the compound nucleus, respectively. $\mu = m[A_1 A_2/(A_1 + A_2)]$ is the reduced mass, m is the nucleon mass. In the calculation of fusion cross-sections, the value of preformation probability P_0 is always taken as unity as the entrance channel has fixed fragments.

While solving the Schrodinger equation [Eq.(2.48)], a term $V_R(\eta, T)$ is involved and defined as the fragmentation potential is given as

$$\begin{aligned} V_R(\eta, T) &= \sum_{i=1}^{2} [V_{LDM}(A_i, Z_i, T)] + \sum_{i=1}^{2} [\delta U_i] \exp(-T^2/T_0^2) \\ &+ V_C(R, Z_i, \beta_{\lambda i}, \theta_i, T) + V_\ell(R, A_i, \beta_{\lambda i}, \theta_i, T) \\ &+ V_N(R, A_i, \beta_{\lambda i}, \theta_i, T). \end{aligned} \tag{2.54}$$

Here, V_{LDM} considered is the temperature-dependent liquid drop model (LDM) of Davidson *et al* [16, 17]. For relevant details, one may refer [18]. The second term i.e. shell-corrections is given by Myer and Switecki [19] with its T-dependence from Davidson *et al* [16]. The constituents of total potential, such as Coulomb potential (V_C), centrifugal potential (V_ℓ) and nuclear proximity potential (V_N), are function of relative separation distance R, charge Z_i (mass A_i) number, temperature T, deformations $\beta_{\lambda i}$ and orientation θ_i degrees of freedom, as discussed earlier.

The temperature T is related to the excitation energy E^*_{CN} of the compound nucleus and given as [84]

$$E^*_{CN} = E_{c.m.} + Q_{in} = \frac{A_{CN}}{9} T^2 - T. \tag{2.55}$$

The temperature effects have been introduced in the radius through the following expression in the above expression, the T-dependent nuclear radius term $R_{0i}(T)$ is given as [85]

$$R_{0i}(T) = R_{0i}[1 + 0.0005T^2]. \tag{2.56}$$

APPENDIX A

Derivation of curvature radius at a point corresponding to the tangent

The speed of rotation of tangent at a given point P defines the curvature ($\overset{\frown}{P_1 P_2}$) of the curve at a point, i.e. curvature radius $R_{\parallel} = R_{i1(\alpha_i)} = \frac{dR(\alpha)}{d\alpha}$ (for convenience see Fig. 2.3), as given below

$$dR(\alpha) = R_{\parallel} d\alpha \Rightarrow R_{\parallel} = \frac{dR(\alpha)}{d\alpha}, \tag{2.57}$$

here,

$$\begin{aligned} dR(\alpha) &= \sqrt{dx^2 + dy^2} = \sqrt{1 + \left(\frac{dy}{dx}\right)^2} dx \text{ and} \\ &\tan\alpha = \frac{dy}{dx}. \end{aligned} \tag{2.58}$$

Differentiating $[\tan\alpha]$ with respect to x, we get

$$\begin{aligned} \frac{d}{dx}[\tan\alpha] &= \frac{d}{dx}\left(\frac{dy}{dx}\right), \\ \Rightarrow [1 + \tan^2\alpha]\frac{d\alpha}{dx} &= \frac{d^2 y}{dx^2}, \\ \Rightarrow d\alpha &= \frac{\frac{d^2 y}{dx^2} \times dx}{[1 + \tan^2\alpha]} = \frac{\frac{d^2 y}{dx^2} \times dx}{[1 + \left(\frac{dy}{dx}\right)^2]}. \end{aligned} \tag{2.59}$$

Substitute $dR(\alpha)$ and $d\alpha$ in Eq.(2.57), we get

$$R_{\parallel} = \frac{\left[1 + \left(\frac{dy}{dx}\right)^2\right]^{3/2}}{|d^2 y/dx^2|}. \tag{2.60}$$

The curvature radius can be defined in the parametric form as [86]

$$R_{\parallel} = \frac{\left[1 + \left(\frac{dy}{d\alpha} \times \frac{d\alpha}{dx}\right)^2\right]^{3/2}}{\left[\frac{d^2 y}{d\alpha^2} \times \frac{dx}{d\alpha} - \frac{dy}{d\alpha} \times \frac{d^2 x}{d\alpha^2}\right] \times [1/\left(\frac{dx}{d\alpha}\right)^3]} = \frac{\left[\left(\frac{dx}{d\alpha}\right)^2 + \left(\frac{dy}{d\alpha}\right)^2\right]^{3/2}}{\left[\frac{d^2 y}{d\alpha^2} \times \frac{dx}{d\alpha} - \frac{dy}{d\alpha} \times \frac{d^2 x}{d\alpha^2}\right]}. \tag{2.61}$$

Now, one can convert the radius of curvature into the plane polar co-ordinates, as done below.

Therefore, the co-ordinates $x = R(\alpha)\cos\alpha$ and $y = R(\alpha)\sin\alpha$. The first and second

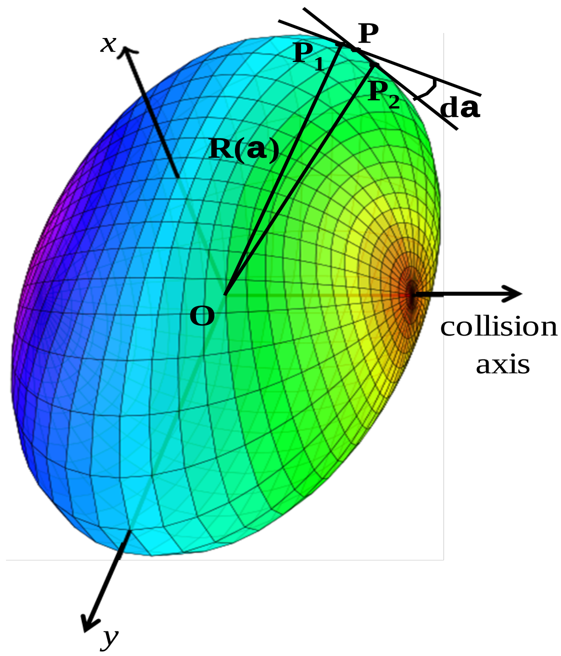

Figure 2.3: Schematic picture of a deformed nucleus representing the radius vector $R(\alpha)$ pointing at points P_1 and P_2, lying on the surface of the nucleus.

derivatives of these co-ordinates are given as below

$$\begin{aligned}
\frac{dx}{d\alpha} &= R'(\alpha)\cos\alpha - R(\alpha)\sin\alpha, \\
\frac{d^2x}{d\alpha^2} &= R''(\alpha)\sin\alpha - 2R'(\alpha)\sin\alpha - R(\alpha)\cos\alpha, \\
\frac{dy}{d\alpha} &= R'(\alpha)\sin\alpha + R(\alpha)\cos\alpha, \\
\frac{d^2x}{d\alpha^2} &= R''(\alpha)\sin\alpha + 2R'(\alpha)\cos\alpha - R(\alpha)\sin\alpha. \qquad (2.62)
\end{aligned}$$

Substitute Eq.(2.62) in Eq.(2.61), we get

$$R_{\|} = \frac{[(R'(\alpha))^2 + (R(\alpha))^2]^{3/2}}{[(R(\alpha))^2 + 2(R'(\alpha))^2 - R(\alpha)R''(\alpha)]}.$$

Replace $R_{\|}$ by $R_{i1}(\alpha_i)$, $R(\alpha)$ by $R_i(\alpha_i)$, $R'(\alpha)$ by $R_i^{'}(\alpha_i)$ and $R''(\alpha)$ by $R_i^{''}(\alpha_i)$. In results, one gets

$$R_{i1}(\alpha_i) = \frac{[(R_i^{'}(\alpha_i))^2 + (R_i(\alpha_i))^2]^{3/2}}{[(R_i(\alpha_i))^2 + 2(R_i^{'}(\alpha_i))^2 - R_i(\alpha_i)R_i^{''}(\alpha_i)]}. \qquad (2.63)$$

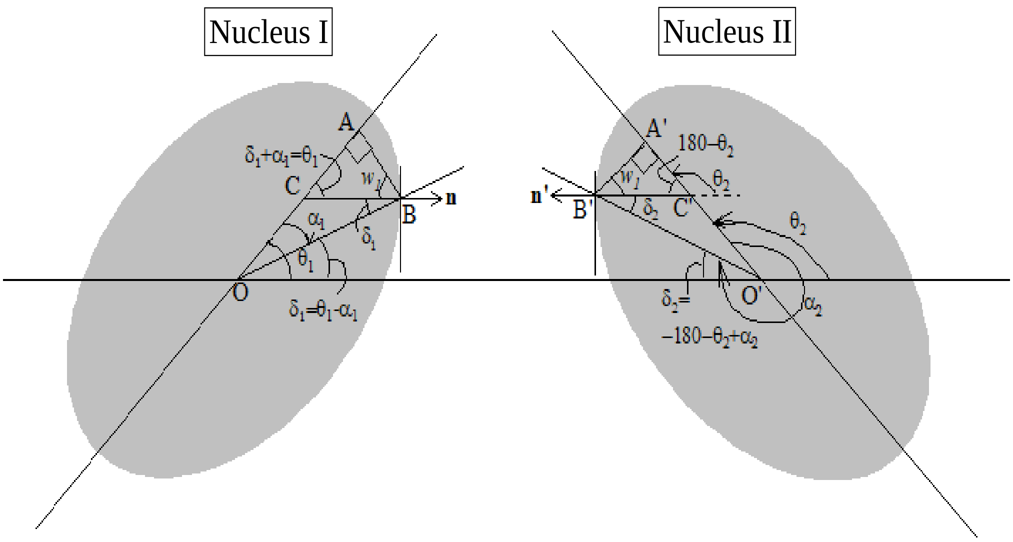

Figure 2.4: Geometry of deformed Nucleus I and II colliding in xy-plane.

APPENDIX B

Derivation of curvature radius perpendicular to the tangent of curve

In this section, the radii of curvature $R_\perp$ or R_{i2} are to be derived and the corresponding geometry is shown in Figs. 2.4 and 2.5.

According to the geometry of Nucleus I, we have the detail of angles as given below:

In triangle **OAB** ($\triangle OAB$),

$$\angle O = \alpha_1$$
$$\angle A = 90^o$$
$$\angle B = w_1 + \delta_1 = 90^o - \alpha_1,$$

here, $w_1 = 90 - \theta_1$ and $\delta_1 = \theta_1 - \alpha_1$. The length OB defines the radius vector $R_1(\alpha_1)$ of Nucleus I. Corresponding to $\angle O$, the length OA becomes $R_1(\alpha_1)\cos\alpha_1$ and corresponding to $\angle B$, the length AB becomes $R_1(\alpha_1)\cos(90 - \alpha_1)$. Further, in triangle **ABC** ($\triangle ABC$), $\angle B$ or w_1 = 90-θ_1.

Therefore, the radius of curvature $R_{12}(\alpha_1)$ in terms of radius vector $R_1(\alpha_1)$ is written as

$\Rightarrow R_{12}(\alpha_1)\cos w_1 = R_1(\alpha_1)\cos(90 - \alpha_1)$

$$R_{12}(\alpha_1) = \frac{R_1(\alpha_1)\cos(90 - \alpha_1)}{\cos w_1}. \tag{2.64}$$

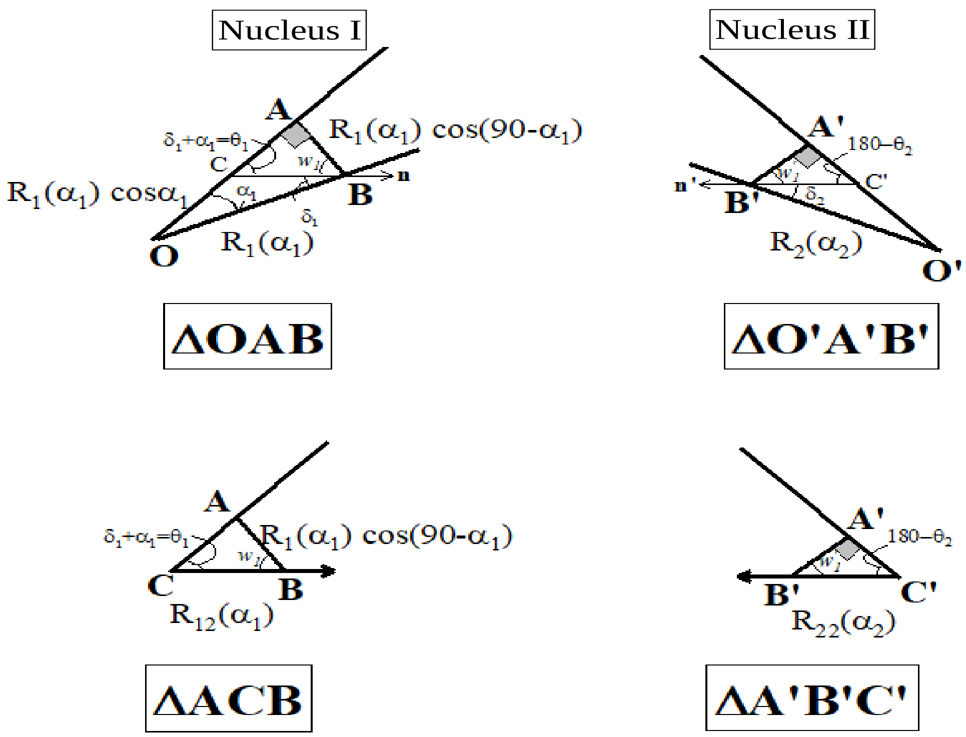

Figure 2.5: A clear visualization of Nuclear radius vectors $R_i(\alpha_i)$, principal radius of curvature $R_{i2}(\alpha_i)$ and corresponding angles.

According to the geometry of Nucleus II, we have the detail of angles as given below:
In triangle $\mathbf{O}'\mathbf{A}'\mathbf{B}'$ $(\triangle O'A'B')$,

$$\angle O' = 360^o - \alpha_2$$
$$\angle A' = 90^o$$
$$\angle B' = w_1' + \delta_2 = -270^o + \alpha_2,$$

here, $w_1' = \theta_2 - 90^o$ and $\delta_2 = -180^o - \theta_2 + \alpha_2$. The length $O'B'$ defines the radius vector $R_2(\alpha_2)$ of Nucleus II. Corresponding to $\angle O'$, the length $O'A'$ becomes $R_2(\alpha_2)\cos(2\pi - \alpha_2)$ and corresponding to $\angle B'$, the length $A'B'$ becomes $R_2(\alpha_2)\cos(-270 + \alpha_2)$. Further, in triangle $\mathbf{A}'\mathbf{B}'\mathbf{C}'$ $(\triangle A'B'C')$, $\angle B'$ or $w_1' = \theta_2 - 90^o$.
Therefore, the radius of curvature $R_{22}(\alpha_2)$ in terms of radius vector $R_2(\alpha_2)$ is written as
$\Rightarrow R_{22}(\alpha_2)\cos w_1' = R_2(\alpha_2)\cos(90 - \alpha_2)$,

$$R_{22}(\alpha_2) = \frac{R_2(\alpha_2)\sin\alpha_2}{\cos(90 - \theta_2)}. \tag{2.65}$$

Bibliography

[1] W. Kohn and L. J. Sham, Phys. Rev. Vol. **137** No. 6A (1965).

[2] M. K. Sharma, R. K. Puri and R. K. Gupta, Z. Physik A **359**, 141 (1997).

[3] Li Guo-Qiang, J. Phys. G: Nucl. Part. Phys. **17**, 1-34 (1991).

[4] V. Yu. Denisov and W. Norenberg, Eur. Phys. J. A **15**, 375-388 (2002).

[5] T. Ichikawa, K. Hagino and A. Iwasmoto, Phys. Rev. Lett. **103**, 202701 (2009).

[6] R. Kumar, M. K. Sharma and R. K. Gupta, Nucl. Phys. A **870-871**, 42-57 (2011).

[7] T. Ichikawa, Phys. Rev. C **92**, 064604 (2015).

[8] S. Jain. R. Kumar and M. K. Sharma, Eur. Phys. J. A **54**, 203 (2018).

[9] V. Yu. Denisov, Phys. Rev. C **91**, 024603 (2015).

[10] S. Jain, M. K. Sharma and R. Kumar, Nucl. Phys. A **997**, 121699 (2020).

[11] C. Y. Wong, Phys. Rev. Lett. **31**, 766 (1973).

[12] R. Kumar *et al*, Phys. Rev. C **80**, 034618 (2009).

[13] J. Maruhn and W. Greiner, Phys. Rev. Lett. **32**, 548 (1974).

[14] R. K. Gupta, W. Scheid and W. Greiner, Phys. Rev. Lett. **35**, 353 (1975).

[15] R. K. Gupta, W. Scheid, and W. Greiner, Phys. Rev. Lett. **35**, 353 (1975).

[16] N. J. Davidson *et al*, Nucl. Phys. A **570**, 61c (1994).

[17] P. A. Seeger, Nucl. Phys. **25**, 1 (1961).

[18] S. DeBenedetti, Nuclear Interactions (New York: book Published by Wiley Sons) (1964).

[19] W. Myers and W. J. Swiatecki, Nucl. Phys. **81**, 1 (1966).

[20] J. Blocki *et al*, Ann. Phys. **105**, 427-462 (1977).

[21] R. Dutt, A. Khare, and U. P. Sukhatme, Am. J. Phys. **59**, 723 (1991).

[22] L.R.B. Elton, Nuclear Sizes, Oxford University Press, London, 1961.

[23] A. Bohr, Mat. Fys. Medd. Dan. Vid. Selsk, Vol. **26**, No. 14 (1952).

[24] A. Bohr and B. R. Mottelson, Mat. Fys. Medd. Dan. Vid. Selsk, Vol. **27**, No. 16 (1953).

[25] D. A. Varshalovich, A. N. Moskalev and V. K. Khersonskii, Quantum Theory of Angular Momentum (World Scientific, Singapore, 1988).

[26] P. Möller *et al*, At. Data and Nucl. Data Tables **109-110**, 1-204 (2016).

[27] B. Hahn, D. G. Ravenhall and R. Hofstadter, Phys. Rev. **101**, 1131 (1956).

[28] H. De Vries, *et al*, At. Data Nucl. Data Tables **36**, 495–536 (1987).

[29] R. K. Gupta *et al*, Phys. Rev. C **75**, 024603 (2007).

[30] S. Jain, M. K. Sharma and R. Kumar, Phys. Rev. C **101**, 051601(R) (2020).

[31] S. Jain, R. Kumar and M. K. Sharma, Chin. Phys. C Vol. **46**, No. 1, 014102 (2022).

[32] S. Jain, R. Kumar, S. K. Patra and M. K. Shamra, Phys. Rev. C **105**, 034605 (2022).

[33] G. A. Leander and Y. S. Chen, Phys. Rev. C **37**, 2744 (1988).

[34] S. Raman *et al*, At. Data and Nucl. Data Tables **78**, 1-128 (2001).

[35] P. A. Butler, J. Phys. G: Nucl. Part. Phys. **43**, 073002 (2016).

[36] A. Bharti and S. K. Khosa, Phys. Rev. C**53**, 2528 (1996).

[37] M. Seiwert *et al*, Phys. Rev. C **29**, 2 (1984).

[38] R. K. Gupta *et al*, Phys. Rev. C **70**, 034608 (2004).

[39] V. Yu. Denisov and N. A. Pilipenko, Phys. Rev. C **76**, 014602 (2007).

[40] W. D. Myers and W. J. Swiatecki, Ark. Fys. **36**, 343 (1967).

[41] W. D. Myers and W. J. Swiatecki, Phys. Rev. C **62**, 044610 (2000).

[42] R. Bass, Phys. Lett. B **47**, 139 (1973).

[43] R. Bass, Nucl. Phys. A **231**, 45 (1974).

[44] R. Bass, Phys. Rev. Lett. **39**, 265 (1977).

[45] P. R. Christensen and A. Winther, Phys. Lett. B **65**, 19 (1976).

[46] V. Y. Denisov, Phys. Lett. B **526**, 315 (2002).

[47] C. Ngô *et al*, Nucl. Phys. A **252**, 237 (1975).

[48] P. Möller and J. R. Nix, Nucl. Phys. A **361**, 117 (1981).

[49] P. Möller *et al*, At. Data Nucl. Data Tables **59**, 185 (1995).

[50] W. Reisdeof, J. Phys. G: Nucl. Part. Phys. **20**, 1297 (1994).

[51] D. Vautherin and D. M. Brink, Phys. Rev. C **5**, 626 (1972).

[52] D. Vautherin, Phys. Rev. C **7**, 1 (1973).

[53] M. Beiner *et al*, Nucl. Phys. A **238**, 29 (1975).

[54] E. Chabanat *et al*, Nucl. Phys. A **635**, 231 (1998).

[55] B. K. Agarwal, S. Shlomo and V. Kim Au, Phys. Rev. C **72**, 014310 (2005).

[56] B. K. Agarwal, S. K. Dhiman and R. Kumar, Phys. Rev. C **73**, 034319 (2006).

[57] Lie-Wen Chen *et al*, Phys. Rev. C **82**, 024321 (2010).

[58] M. Dutra *et al*, Phys. Rev. C **85**, 035201 (2012).

[59] Zhen Zhang and Lie-Wen Chen, Phys. Rev. C **94**, 064326 (2016).

[60] D. Jain, R. Kumar and M. K. Sharma, Phys. Rev. C **85**, 024615 (2012).

[61] I. Sharma, M. S. Gautam and M. K. Sharma, Int. J. Mod. Phys. E Vol. **26**, No. 11, 1750077 (2017).

[62] B. Grammaticos and A. Voros, Ann. Phys. **123**, 359-380 (1979).

[63] B. Grammaticos and A. Voros, Ann. Phys. **129**, 153-171 (1980).

[64] J. Bartel and K. Bencheikh, Eur. Phys. J. A **14**, 179-190 (2002).

[65] P. Bonche, H. Flocard, P.H. Heenen, Nucl. Phys. A **467**, 115 (1987).

[66] L.R.B. Elton, Proc. Phys. Soc. Lond. A **63**, 1115 (1950).

[67] H. De Vries *et al*, At. Data Nucl. Data Tables **36**, 495–536 (1987).

[68] K. Alder and A. Winther, Nucl. Phys. A **132**, 14 (1969).

[69] B. V. Carlson, L. C. Chamon and L. R. Gasques, Phys. Rev. C **70**, 057602 (2004).

[70] N. Takigawa, T. Rumin, and N. Ihara, Phys. Rev. C **61**, 044607 (2000).

[71] C. Amsler, *Nuclear and Particle Physics*, IOP Publishing (2015).

[72] D. L. Hill and J. A. Wheeler, Phys. Rev. **89**, 1102 (1953).

[73] M. Beckerman *et al*, Phys. Rev. C **23**, 4 (1981).

[74] H. Kroger and W. Scheid, J. Phys. G **6**, L85 (1980).

[75] H. S. Khosla and S. S. Malik, Nucl. Phys. **A513**, 115-124 (1990).

[76] S. Kumar and R. K. Gupta, Phys. Rev. C **55**, 1 (1997).

[77] R. K. Gupta, S. Kumar and W. Scheid, Int. J Mod. Phys. E, Vol. **6**, No. 2, 259-274 (1997).

[78] S. J. Sanders *et al*, Phys. Rev. C **40**, 2091 (1989).

[79] S. Sander, Phys. Rev. C **44**, 2676 (1991).

[80] T. Matsuse, Phys. Rev. C **55**, 1380 (1997).

[81] R. Dutt, A. Khare and U. P. Sukhatme, Americal Journal of Physics **59**, 723 (1991).

[82] M. Balasubraniam *et al*, J. Phys. G **29**, 2703 (2003).

[83] R. K. Gupta *et al*, Phys. Rev. C **68**, 014610 (2003).

[84] K. J. LeCouteur and D. W. Lang, Nucl. Phys. **13**, 32 (1959).

[85] S. Shlomo and J. B. Natowitz, Phys. Rev. C **44**, 2878 (1991).

[86] Erwing Kreyszig, "*Advanced Engineering Mathematics*", John Wiley Sons, Inc. 8$^{\text{th}}$ Ed. (1999).

Chapter 3

Implication of different density approximations in fusion dynamics of ^{58}Ni-based reactions

3.1 Introduction

In the low energy heavy-ion collisions, the study of fusion reactions in terms of fusion barrier, which is comprised of nuclear and Coulomb potentials, has been of central interest. Unlike the established theory in deriving the Coulomb potential, different theoretical models have been adopted to derive the nucleus-nucleus interaction potential [1–7]. In the present chapter, the semiclassical approach of Skyrme Energy Density Formalism (SEDF) [8] has been used to derive the effective nuclear potential for heavy-ion induced reactions. Within the framework of SEDF, the effect of different nuclear density approximations has been analyzed for a variety of compound nuclear systems, formed via ^{58}Ni-based reactions. The derived nuclear potential under the influence of SEDF can be classified by two physical assumptions of adding the nuclear densities of colliding nuclear partners: sudden and adiabatic density approximations [9,10]. The present work explores the significance of sudden density approximation which defines the fast collision process in terms of the fusion barrier characteristics (i.e. barrier position R_B, barrier height V_B and barrier curvature $\hbar\omega_B$) and fusion cross-sections. Using this approximation, the total kinetic energy density $\tau(\rho)$ and spin-orbit density $\vec{J}(\rho)$ terms of compound nuclear system are expressed as the function of nucleon density (ρ_q; $q = n$ or p) of CN (see Eq.(2.21)) [7,9]. On the other hand, there is an alternate way of accumulating the nucleon densities of colliding nuclei, see Eq.(2.22), known as frozen density approximation [9]. In Ref. [9], the densities are added under sudden and frozen density approximations to derive the nucleus-nucleus interaction potential for the medium, and heavy-mass systems. For the formation of heavy-mass compound nuclear systems, the pocket of interaction potential disappears under sudden approximation. In view of this, in this chapter, the realistic barrier parameters using the sudden density approximation are obtained by modifying the central density term ($\rho_{0i} = \frac{3A_i}{4\pi R_i^3}$), which is an independent of surface diffuseness factor 'a' [11], and termed it as modified sudden density approximation. In addition to the above, in [12], the relaxed-density approximation was used to calculate the interaction potential of two colliding nuclei in the framework of Extended Thomas-Fermi approach. Using this relaxed-density approach for light and medium mass nuclear systems, the corresponding barrier heights become closer to the empirical data [12]. However, the same formalism has the limitation for the heavy-mass systems. To overcome this, the phenomenological relaxed-density approximation based potential in the Woods-Saxon form has been proposed. Due to the additional correction term in the minimized function, used for obtaining the parameters of the phenomenological potential, the empirical barrier heights are duly addressed. Hence, the phenomenological relaxed-density approach is opted in the present analysis.

This way, in the present calculations, a comparative analysis of frozen, sudden, modified sudden and relaxed density approximations has been done for ^{58}Ni+^{58}Ni reaction [13]. In order to extend this idea, the effect of different density approximations has also been analyzed for the lighter and heavier mass compound nuclear systems, formed via ^{58}Ni-based reactions. The above analysis has been discussed in terms of the fusion barrier characteristics (V_B, R_B and $\hbar\omega_B$) and subsequently in the calculation of fusion cross-sections (σ_{fus}). The σ_{fus} are estimated to address the above barrier anomalies via the extended ℓ-summed Wong model [14] and the below barrier dynamics is explored in view of different density approximations, as discussed above. The related results are discussed in the following section.

3.2 Calculations and results

Here, we have studied the role of different density approximations employed within the SEDF in terms of the fusion barrier characteristics and fusion cross-sections for different compound nuclei formed via ^{58}Ni-based reactions, i.e. ^{18}O, ^{40}Ca, ^{58}Ni and ^{132}Sn+^{58}Ni. Note that, for deriving the nucleus-nucleus interaction potential using SEDF approach, the SLy4 Skyrme force parameters [15] has been utilized. The parameters of this force are reliable to reproduce several properties of nuclear matter, neutron stars, and finite nuclei belonging to the region of stable and unstable nuclei [12, 15].

Firstly, for ^{58}Ni+^{58}Ni reaction, the total interaction potential obtained with the effect of various density approximations is shown in Fig. 3.1 as a function of separation distance R. From this figure, one can observe that the potential based on frozen approximation possesses the lowest barrier height (V_B) and largest barrier position (R_B). However, V_B of relaxed-density approximation (phenomenological Woods-Saxon) based potential is the largest value followed by sudden and modified sudden density approximations. In other words, the densities added in frozen way offer a larger reaction time as compared to the rest of the density approximations. Such situation may give a larger possibility of fusion between two colliding nuclei. On the other hand, due to the sudden density approximation, one gets a vanished pocket of the potential. In view of this, an attempt has been made within the sudden density approximation by considering central density $\rho_{0i} = \frac{3A_i}{4\pi R_i^3}$ [11] (independent of surface diffuseness factor a), instead of ρ_{0i} [Eq.(2.28)] depending on a factor. Henceforth, the respective barrier characteristics can be observed for the modified sudden density approximation. Apart from this, the penetration area of the relaxed-density potential is found to be larger than others, which in turn, may resist the formation of compound nucleus. From the above discussion, it is relevant to note that the total interaction potential exhibits different results depending on the choice of density approximations.

Further, the collective effect of barrier characteristics obtained due to considered choices of density approximations has been explored in terms of fusion cross-sections, σ_{fus}. The fusion cross-sections calculated for ^{58}Ni+^{58}Ni reaction using the Wong formula [16] and extended version [14] are shown in panels (a) and (b) of Fig. 3.2, respectively, as a function of the center of mass energy $E_{c.m.}$, varying across the Coulomb barrier. The theoretically calculated cross-sections based on the Wong formula are compared with the available experimental data [13]. One may observe from panel (a) of Fig. 3.2 that, the fusion cross-sections obtained due to frozen density approximation is relatively larger than that of the modified sudden density approach. Also, the obtained values of σ_{fus} from these two approximations overestimate the experimental data [13] across the Coulomb barrier. On the contrary, for the relaxed-density approach, the result shows fusion hindrance at the below barrier energies which is possibly due to a larger area under the curve of inverted Harmonic oscillator of the corresponding interaction potential. Consequently, using Wong formula, any of the approximations are not matching with the experimental data. Since within the Wong formula, the ℓ-values related to the partial waves are taken up to ∞. In view of this, the Wong formula

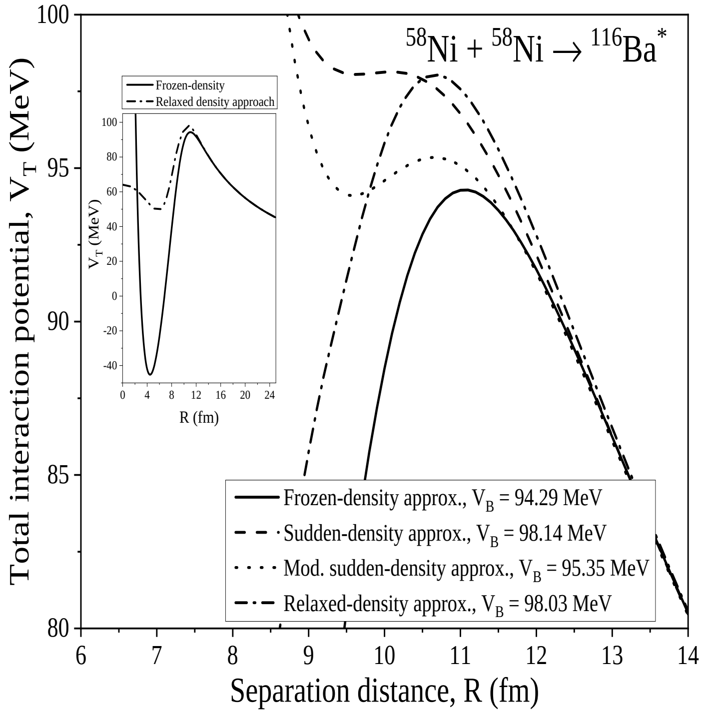

Figure 3.1: The comparison of different total interaction potentials, due to various density approximations, as a function of separation distance *R (fm)* between two colliding spherical nuclei of ^{58}Ni+^{58}Ni [13]. The deep well potentials of frozen and relaxed-density approaches shown in the inset.

has been extended by Gupta and his collaborators [14] via taking the ℓ-summation explicitly for better addressal of experimental results.

In view of above, with the use of extended ℓ-summed Wong model, the fusion cross-sections obtained using frozen- and modified sudden-density approximations address the experimental data, see in panel (b) of Fig. 3.2, especially at the below barrier region. At the highest-barrier energies, the Compound nucleus possesses higher ℓ-values, for which the pocket of modified sudden density approximation gets diminished and hence the fusion cross-sections get suppressed from the data of higher energies. Moreover, the barrier parameters associated with the relaxed-density approximation used within the extended ℓ-summed Wong model again shows fusion hindrance at the below barrier region. Also, the details of calculated and experimentally obtained fusion cross-sections for ^{58}Ni+^{58}Ni reaction forming ^{116}Ba* compound nucleus are displayed in Table 3.1, with center of mass energy $E_{c.m.}$ (MeV) and corresponding values of $\ell_{max}(\hbar)$ obtained for different density approximations. Note that, the obtained ℓ_{max}-values under different choices of density approximations are in match with ℓ-values provided in [13] for the above barrier energies. For below- and near-barrier energies, the frozen and modified sudden density approximations show smooth variation in

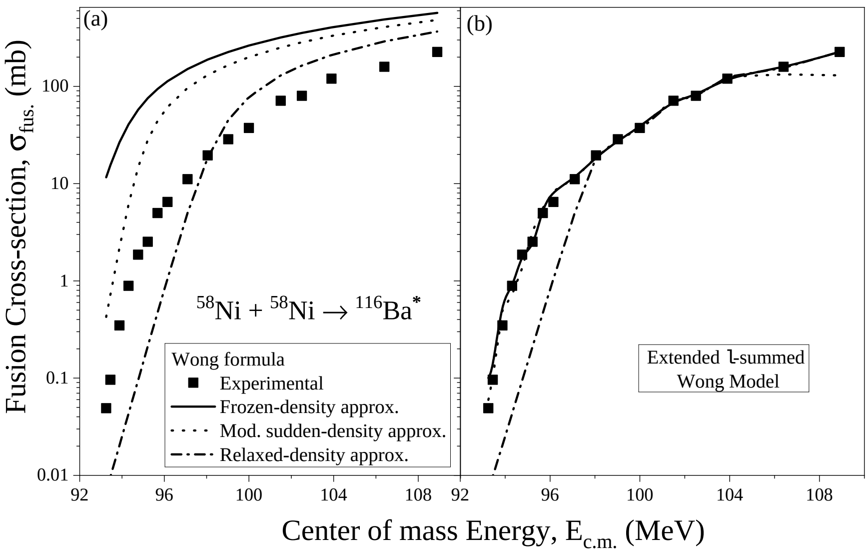

Figure 3.2: The fusion cross-sections calculated using frozen, modified sudden, and relaxed-density approaches within (a) Wong formula [16], and (b) extended ℓ-summed Wong model [14] compared with the available experimental data [13].

ℓ_{max}-values, from that of relaxed-density approximation.

Furthermore, the effect of different density approximations has also been analyzed for lighter- and heavier-mass projectiles of ^{58}Ni-based reactions, i.e. ^{18}O, ^{40}Ca and ^{132}Sn+^{58}Ni reactions, in the perspective of total interaction potential varying as a function of separation distance R (fm). For these reactions, one can analyze from the panels (a)-(d) of Fig. 3.3 that, the barrier height of relaxed-density approximation becomes lower than the frozen density approximation for ^{132}Sn+^{58}Ni reaction, which is otherwise higher for lighter mass projectiles, i.e. ^{18}O, ^{40}Ca and ^{58}Ni. Unlike sudden, the V_B obtained due to the modified sudden density approximation seems similar to that of frozen-density approximation for the above considered choices of nuclear partners, except for ^{132}Sn+^{58}Ni case. In the lower panels (e)-(h) of Fig. 3.3, one can understand the reason behind the switching behavior of frozen and relaxed density approximations for ^{132}Sn+^{58}Ni nuclear reaction. With a precise observation, one may notice that, the frozen approximation seems more attractive than that of relaxed-density approach for ^{18}O, ^{40}Ca and ^{58}Ni-induced reactions. However, for ^{132}Sn+^{58}Ni reaction, the relaxed-density approximation based potential is found more attractive than frozen approximation based potential. Because the nuclear radius polynomial (Eq.(2.29)) used within the SEDF starts to make large difference from the radius (Eq.(2.25)) used in the relaxed-density approach, as one goes towards higher-mass number of projectile nucleus, as shown in the inset of Fig. 3.3(h). In other words, the larger value of nuclear radius lowers

Table 3.1: Calculated fusion cross-sections within extended ℓ-summed Wong model computed using frozen, modified sudden, and relaxed-density approaches for $^{58}Ni+^{58}Ni$ [13] reaction, at different center of mass energies, $E_{c.m.}$. The corresponding ℓ-values are given and compared with ℓ-values provided in [13] for above barrier energies.

$E_{c.m.}$ (MeV)	T (MeV)	Expt.	Frozen-density		Mod. sudden-density		Relaxed-density approach		Expt. [13]
		$\sigma_{fus.}$ (mb)	$\sigma_{fus.}$ (mb)	ℓ_{max} ($\hbar$)	$\sigma_{fus.}$ (mb)	ℓ_{max} ($\hbar$)	$\sigma_{fus.}$ (mb)	ℓ_{max} ($\hbar$)	ℓ_{max}† ($\hbar$)
93.45	1.794	0.096	0.123	0	0.101	2	0.0098	19	-
93.88	1.804	0.348	0.171	0	0.293	2	0.0204	21	-
94.31	1.813	0.888	0.813	1	0.723	2	0.0433	23	-
94.76	1.823	1.860	1.996	2	1.358	2	0.0948	25	-
95.22	1.833	2.520	2.075	2	3.234	3	0.211	26	-
95.68	1.843	4.980	5.832	4	5.609	4	0.469	27	-
96.15	1.853	6.470	8.425	5	8.337	5	1.049	29	-
97.10	1.873	11.10	11.411	6	11.406	6	5.002	31	-
98.05	1.893	19.50	18.692	8	18.692	8	18.464	34	-
99.02	1.914	28.60	27.648	10	27.648	10	28.638	12	-
100.0	1.934	37.30	38.245	12	38.245	12	35.886	12	-
101.5	1.964	71.20	72.252	17	72.252	17	71.138	17	17±1
102.5	1.984	79.90	79.709	18	79.709	18	79.409	18	18±1
103.9	2.012	120.0	125.453	23	125.453	23	125.453	23	22±1
106.4	2.060	159.0	155.058	26	132.937	24	155.058	26	26±1
108.9	2.108	226.0	226.294	32	129.875	24	226.294	32	32±1

† The ℓ_{max}-values given in Ref. [13] are available for above barrier energies.

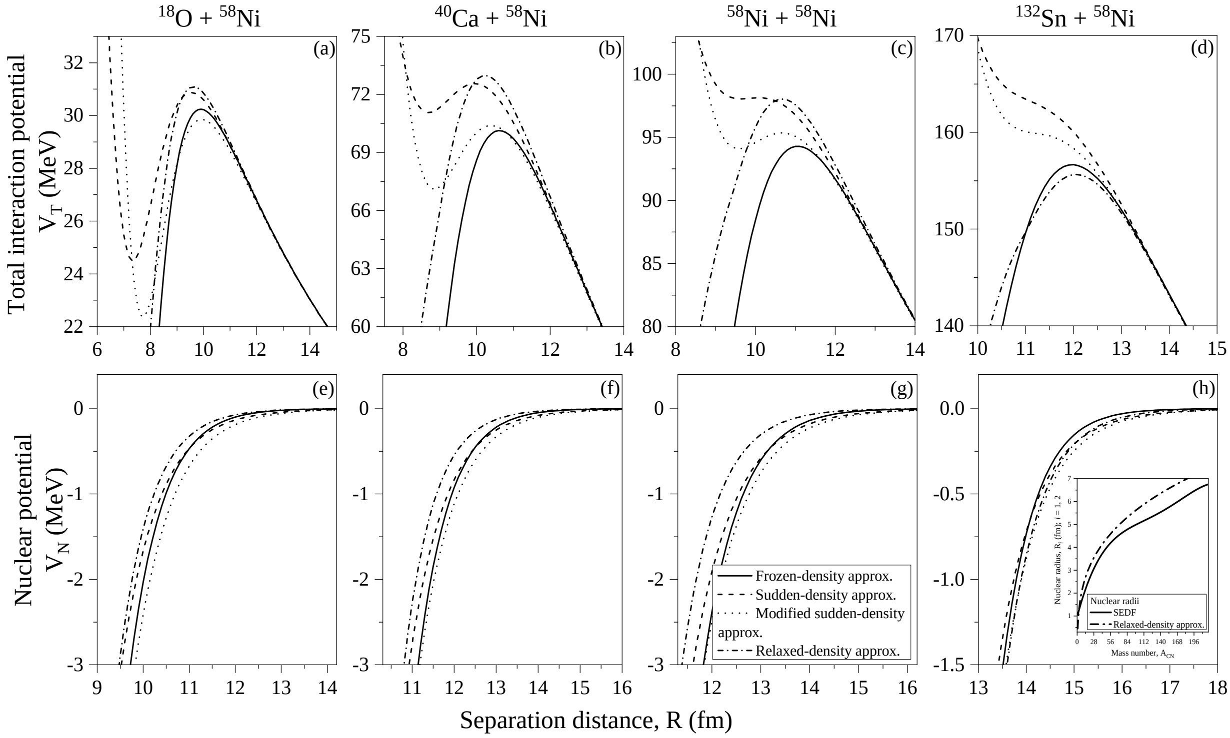

Figure 3.3: A comparative analysis of frozen, sudden, modified sudden, and relaxed-density approximations for ^{18}O, ^{40}Ca, ^{58}Ni and ^{132}Sn+^{58}Ni reactions, in terms of (a)-(d) total interaction potentials, and (e)-(h) corresponding nuclear potentials with the variation of separation distance R (fm).

the barrier height.

In addition to the above, the modification observed in the barrier characteristics due to the sudden and modified density approximations based potentials has also been elaborated through the density profiles of projectile and target nuclei, as shown in Fig. 3.4 for (a) ^{18}O+^{58}Ni, (b) ^{40}Ca+^{58}Ni, (c) ^{58}Ni+^{58}Ni and (d) ^{132}Sn+^{58}Ni reactions. Within the sudden and modified density approximations, the central density term ρ_{0i} used as input term is dependent and independent of surface diffuseness factor 'a', respectively. It is clear from Fig. 3.4 that, the region of interaction of projectile (ρ_1) and target (ρ_2) nuclear densities obtained using ρ_{0i} independent of a (within modified sudden approximation) is comparatively larger than that of obtained from ρ_{0i} dependent of a (within sudden approximation). Thus, it can be said that, in the case of modified sudden density approximation, the overlapping region of colliding nuclear densities is of relatively larger area from that of sudden density approximation. Consequently, one can obtain relevant detail of fusion barrier characteristics using the modified sudden approximation for lighter and intermediate mass compound nuclear systems, i.e. ^{76}Kr*, ^{98}Cd* and ^{116}Ba* formed via ^{18}O, ^{40}Ca and ^{58}Ni+^{58}Ni reactions,

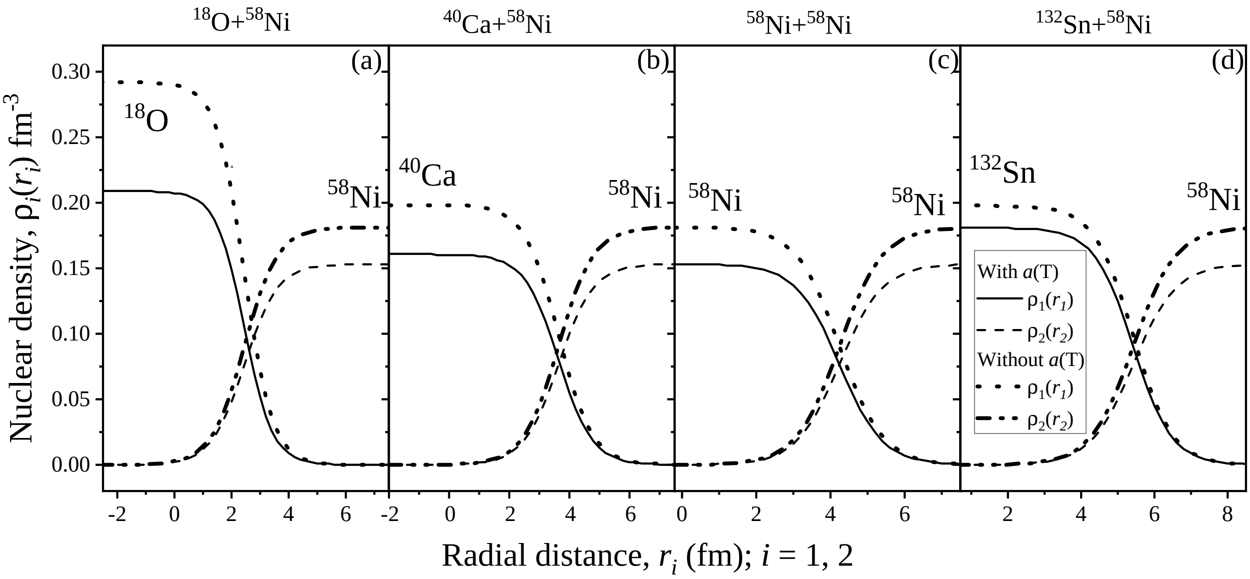

Figure 3.4: The solid and dash lines represent the density profile of projectiles and target nuclei, respectively, which include the surface thickness factor, *a(T)*, compared with dotted and dash-dotted density profiles excluding *a(T)* factor for all chosen nuclear reactions.

respectively. In the above discussion, the role of various nuclear density approximations has been interpreted for considered choices of ^{58}Ni-based reactions in terms of fusion barrier characteristics extracted from the corresponding total interaction potential. In further calculations, the collective effect of V_B, R_B and $\hbar\omega_B$ has been explored in determining the fusion cross-sections with the use of Wong formula and extended ℓ-summed Wong model. In Fig. 3.5(a) for ^{18}O+^{58}Ni reaction, the calculated fusion cross-sections (σ_{fus}) using the Wong formula under frozen and modified sudden density approximations are found to overestimate the experimental data [17]. On the other hand, the fusion hindrance is shown due to sudden and relaxed-density approaches. The overestimation has been taken care of by adopting the extended ℓ-summed Wong model, which give appropriate results for frozen and modified sudden density approximations across the Coulomb barrier energies, as shown in Fig. 3.5(b). Furthermore, for ^{40}Ca+^{58}Ni reaction, the panels (c) and (d) of Fig. 3.5 show similar results for all considered density approximations, as observed in panels (a) and (b) of this figure, respectively. Here, it is important to note that, at highest $E_{c.m.}$, the large ℓ-values cease to give appropriate barrier characteristics as the pocket disappears for the sudden and modified sudden density approximations. Moving ahead, the fusion cross-sections of ^{132}Sn+^{58}Ni reaction are calculated using the Wong formula and its extended version only for frozen and relaxed-density approaches, as the barrier characteristics

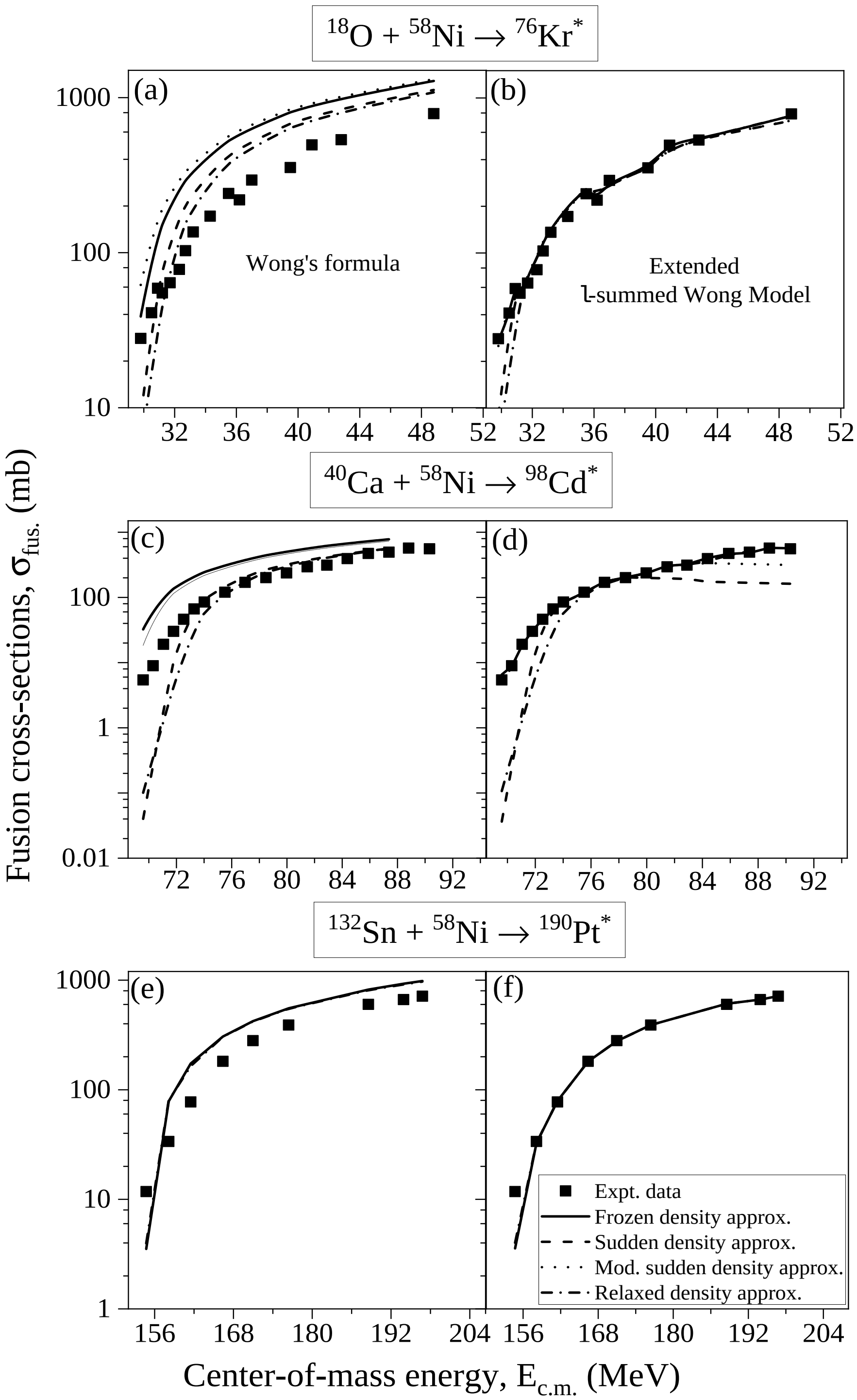

Figure 3.5: Comparison of fusion cross-sections, σ_{fus}, calculated using Wong's formula and its extended version, with the available experimental data for (a), (b) $^{18}O+^{58}Ni$ [17], (c), (d) $^{40}Ca+^{58}Ni$ [18], and (e), (f) $^{132}Sn+^{58}Ni$ [19] reactions over a wide range of center of mass energies, $E_{c.m.}$ (MeV), across the Coulomb barrier.

of sudden and modified sudden density approximations get vanished for this reaction, for reference see Fig. 3.3. One can see clearly from Fig. 3.5(e) that, σ_{fus} calculated using the Wong formula for the frozen and relaxed density approximations overlap each other, since the difference between their barrier heights is about 0.7 MeV for ^{132}Sn+^{58}Ni case. Also, the calculated σ_{fus} exceeds the data across the barrier, except at the lowest energy. On the other hand, in Fig. 3.5(f), the ℓ-dependent barrier characteristics of frozen and relaxed-density approaches based potentials employed within the extended version of Wong formula adjust the overestimated cross-sections for the above mentioned reaction. From Fig. 3.5, it can be said that, the hindrance is observed mainly due to the sudden fusion of two nuclei, at the sub-barrier region. On the other hand, with the use of frozen density approximation, the deep pocket and relevant barrier characteristics of interaction potential found to perform better for all the considered choices of nuclear reactions, except at the lowest energy in the case of ^{132}Sn+^{58}Ni reaction. From the above results and discussions, it is also noteworthy that, the barrier characteristics can be easily extracted due to the frozen and relaxed-density approximations, with the increase in the mass of composite systems, however, the barriers obtained due to sudden and modified sudden density approximations get diminished.

3.3 Conclusion

In this chapter, the frozen, sudden and modified sudden density approximations have been employed within the Extended Thomas-Fermi approach of the Skyrme Energy Density Formalism, which in turn, show corresponding effect on the fusion barrier characteristics and fusion cross-sections. The above analysis has been compared with that of relaxed-density approximation based Woods-Saxon potential. In order to explore the relative role of different density approximations in the fusion dynamics, the ^{58}Ni-based reactions which involve projectiles (^{18}O, ^{40}Ca, ^{58}Ni and ^{132}Sn) from different mass-regions have been taken into consideration. For the lighter and medium mass compound systems ^{76}Kr*, ^{98}Cd* and ^{116}Ba* formed via ^{18}O, ^{40}Ca and ^{58}Ni+^{58}Ni reactions, respectively, the calculated fusion cross-sections using the extended ℓ-summed Wong model for frozen and modified sudden density approximations are found to address the available experimental data especially at sub-barrier energies. However, the sudden and relaxed-density approaches show fusion hindrance for the above mentioned compound nuclear systems. For heavy-mass compound nucleus (^{190}Pt*) formed from ^{132}Sn+^{58}Ni reaction, the pocket of the interaction potential corresponding to the sudden and modified sudden approximations gets diminished. For this system, the relaxed-density approximation behaves like frozen-density approximation and address the available experimental data. In brief, it can be said that, the frozen density approximation seems to be a better choice especially for the ^{58}Ni-based reactions involving projectile nuclei from different mass-regions.

On the basis of above results, the effect of various density approximations employed within the phenomenological (relaxed-density approximation) and SEDF (sudden, modified-sudden and frozen density approximations) based potentials has been explored in order to understand the amalgamation of nuclear densities of colliding nuclei for the formation of compound nuclear systems formed via ^{58}Ni-based reactions. This work has also been published [20]. For the considered choices of projectile-target combinations, the frozen-density approximation approximation is found to give better agreement with the experimental results across the Coulomb barrier energies. Further, in the continuity of present chapter, we intend to study the nuclear density distribution of mass-symmetric and asymmetric choices of projectile-target combinations with the use of two- and three-parameter density functions. For this analysis, the significance of above said density functions which are employed within the semiclassical approach of SEDF, using frozen-density approximation, is going to be discussed in terms of fusion barrier characteristics and subsequently the fusion cross-sections for ^{58}Ni-based reactions.

Bibliography

[1] T. H. R. Skyrme, Phil. Mag. **1** 1043(1956).

[2] T. H. R. Skyrme, Nucl. Phys. **9** 615 (1959).

[3] K. A. Brueckner, J. R. Buchler, M. Kelley, Phys. Rev. **173** 944 (1968).

[4] D. Vautherin, D. M. Brink, Phys. Rev. C **5** 626 (1972).

[5] Fl. Stancu, D. M. Brink, Nucl. Phys. A **270** 236 (1976).

[6] I. Dutt, R. K. Puri, Phys. Rev. C **81** 044615 (2010).

[7] R. Kumar, M. K. Sharma, R. K. Gupta, Nucl. Phys. A **870-871** 42-57 (2011).

[8] M. Brack, C. Guet and H.-B. Hakansson, Phys. Rep. **123**, 275 (1985).

[9] Li Guo-Qiang, J. Phys. G: Nucl. Part. Phys. **17**, 1-34 (1991).

[10] T. Ichikawa, Phys. Rev. C **92**, 064604 (2015).

[11] V. M. Strutinsky, A. G. Magner, V. Yu. Denisov, Z. Phys. A - Atoms and Nuclei **322**, 149-156 (1985).

[12] V. Yu. Denisov, Phys. Rev. C **91**, 024603 (2015).

[13] M. Beckerman *et al*, Phys. Rev. C **23**, 4 (1981).

[14] R. Kumar, M. Bansal, S. K. Arun and R. K. Gupta, Phys. Rev. C **80**, 034618 (2009).

[15] E. Chabanat *et. al.*, Nucl. Phys. A **635**, 231-258 (1998).

[16] C. Y. Wong, Phys. Rev. Lett. **31**, 12 (1973).

[17] A. M. Borges *et al*, Phys. Rev. C **46**, 6 (1992).

[18] D. Bourgin *et al*, Phys. Rev. C **90**, 044610 (2014).

[19] Z. Kohley *et al*, Phys. Rev. Lett. **107**, 202701 (2011).

[20] S. Jain, R. Kumar and M. K. Sharma, Eur. Phys. J. A **54**, 203 (2018).

Chapter 4

Relevance of 2pF, 3pF and 3pG density distributions on fusion barrier characteristics

4.1 Introduction

As it is known that, the closest approach of alpha-particle from Gold target in Rutherford's α-scattering experiment provides an evidence regarding the existence of nucleus and its probable size/radius. However, this experiment was based on the Coulomb's force of repulsion between two positively charged nucleons and hence could not provide the desired understanding of the distribution of nucleons inside the nucleus. Thereafter, the electron scattering experiments were performed to obtain the charged-density distribution within the nucleus, which was used to measure the nuclear radius and related parameters of shape configuration [1,2]. At the initial stages of theoretical observations, the data was described by considering homogeneous distribution of nucleons inside the nucleus, which does not come out to be adequate for explaining the nuclear behavior [3]. To overcome this problem, the data of electron scattering experiment was described by the two parameter Fermi (2pF) model [4–6]. Also, the other versions of 2pF, i.e. the three-parameter Fermi (3pF) and three-parameter Gaussian (3pG), which possess an additional wine-bottle parameter have been employed to address the electronic scattering data. Therefore, the density parameters i.e. half-density radius 'R_0', surface thickness 'a' and wine-bottle parameter 'w' of the above mentioned Fermi and Gaussian density functions are further used to analyze the corresponding variations in the behavior of nuclear density.

In literature [7–9], the nuclear density as an input is utilized to calculate the nucleus-nucleus interaction potential within the Extended Thomas-Fermi approach of SEDF. To study the heavy-ion collisions in the low energy region, it is important to have a comprehensive knowledge of the total interaction potential, which is in general comprised of the Coulomb potential (V_C), nuclear potential (V_N) and centrifugal potential (V_ℓ). The addition of only V_C and V_N

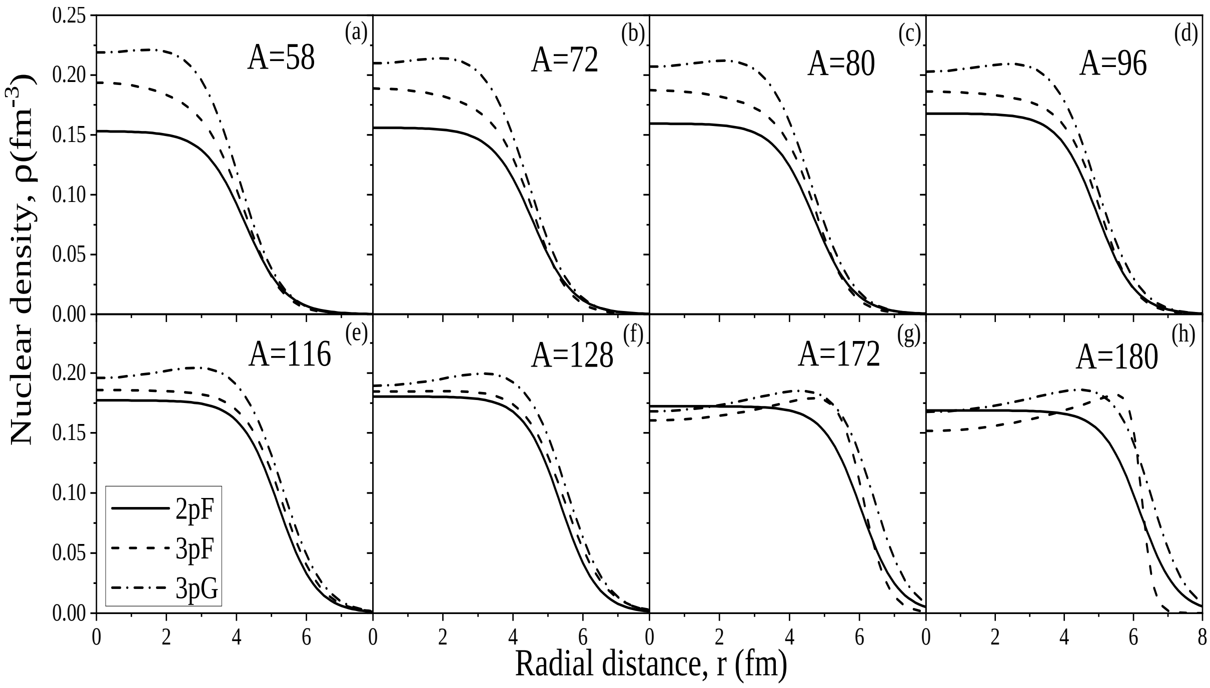

Figure 4.1: Comparison of 2pF, 3pF and 3pG nuclear density functions for the nuclei from different mass region of the periodic table.

potentials gives rise to the fusion barrier characteristics (barrier height V_B, and corresponding position R_B and barrier curvature $\hbar\omega_B$), which serve as crucial inputs to govern the nuclear fusion dynamics. In the present chapter, the above mentioned density distribution functions have been adopted to analyze the corresponding variations on the fusion barrier characteristics. In the three-parameterized density functions, the w-parameter has negative and positive values, respectively, for 3pF and 3pG density functions in the light-mass region. However, for heavy-mass region ($A > 120$), this parameter always has positive value for both the 3pF and 3pG density functions. The authors of [10] had analyzed that, for w>0, the nuclear density shows central depression for heavy-mass nuclei. For an illustration, the density profiles of 3pF and 3pG density functions are shown in Fig. 4.1 for nuclei lying in different mass-region. From this figure, it is clear that, the 3pF and 3pG density functions start to give central depression as one moves from lighter mass nuclei to the heavier ones. Also one can notice that, an additional 'w' or wine-bottle parameter involved in three-parameter density functions modifies the density profile mainly in the tail region of heavy-mass nuclei from that of two-parameter density function. The variations in the tail region due to different density functions influence the barrier characteristics. Thus, in the present chapter, a detailed comprehensive analysis of two (2pF) and three parameter (3pF and 3pG) density functions, employed within the semiclassical SEDF, has been illustrated in terms of the barrier characteristics, i.e barrier position R_B, barrier height V_B and barrier curvature $\hbar\omega_B$. This analysis is done for a variety of nuclear reactions with mass-asymmetry η_A varying from 0 to 0.8. Here, the nuclei are considered to be spherical.

Further, the collective effect of V_B, R_B and $\hbar\omega_B$ obtained using different choices of density functions has been explored in the calculation of fusion cross-sections (σ_{fus}) across the Coulomb barrier energies. Generally, it has been analyzed at the below-barrier region that, the theoretical calculations of σ_{fus} using one-dimensional penetration model shows an abrupt decrease with respect to the experimental data [11–13]. Such phenomena is termed as fusion hindrance, which is explored in the theoretical [14–18] as well as experimental studies [11–13]. In view of this, to investigate the significance of two- and three-parameterized density functions at the below barrier region, the ^{58}Ni-based reactions (i.e. ^{8}B, ^{18}O, ^{58}Ni and ^{132}Sn+^{58}Ni) [16, 19–21] are taken into consideration, which are known to show fusion hindrance phenomena [22]. For the above considered nuclear reactions, it has been observed in this chapter and [23] that, for symmetric reactions, the nuclear density distributions of two-parameter Fermi (2pF) is showing difference in the tail and its surrounding region, due to its larger value of half-density radius, as compared to that of the three-parameter Fermi/Gaussian density functions (3pF/3pG). This leads to lower the barrier height due to 2pF from that of 3pF and 3pG density functions. On the other hand, for mass-asymmetric choices of ^{58}Ni-based reactions, the 3pF and 3pG density functions, because of relatively larger value of half-density radius, give lower value of V_B from that of 2pF density function. On the basis of above observation, a detailed discussion of different density functions and corresponding effect on barrier characteristics and cross-sections are provided in the upcoming section. It is important to mention that, the analysis done for the symmetric and asymmetric kinds of nuclear reactions using two- and three-parameter density functions has been exercised using SLy4 Skyrme force parameters [24] and frozen density approximation [25–27] within the SEDF approach to derive the nucleus-nucleus interaction potential. Further, for the calculation of fusion cross-sections, the extended ℓ-summed Wong model [28] has been utilized and ℓ-values are obtained using the sharp cut-off model [19] for the above barrier energies and extrapolated for the below-barrier region. In the following sections, the calculations and results related to the topic of this Chapter are discussed in detail.

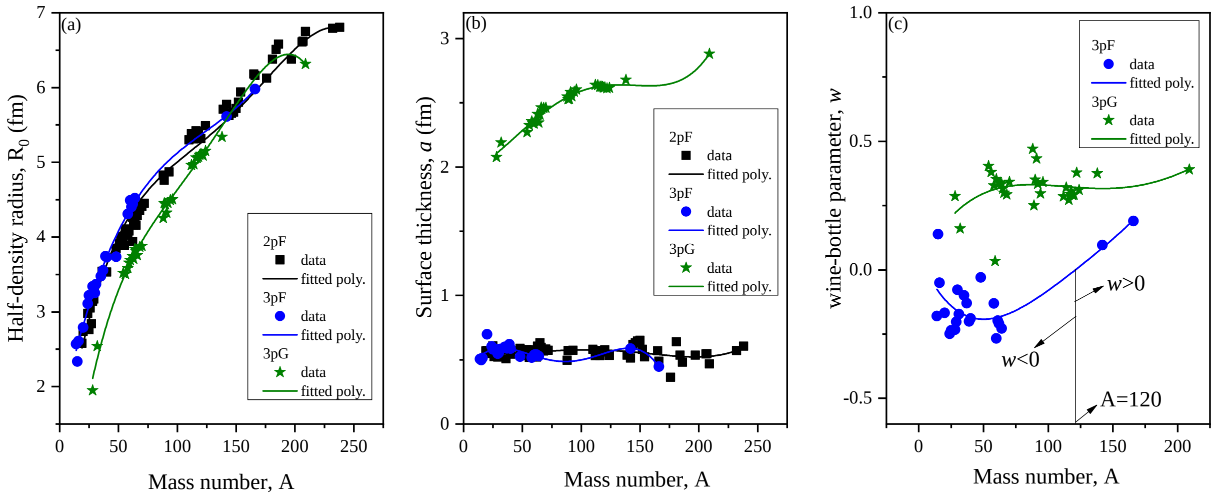

Figure 4.2: The polynomials of (a) half-density radius R_0 (fm), (b) surface thickness a (fm) and (c) wine-bottle parameter w (dimensionless quantity) plotted as a function of mass number A varying from (4-238) for 2pF, (14-166) for 3pF and (28-209) for 3pG density functions.

4.2 Calculations and results

Different density functions that is, two-parameter Fermi 2pF, three-parameter Fermi 3pF and three-parameter Gaussian 3pG, which are used within the semiclassical approach of the Skyrme Energy Density Formalism (SEDF), lead to the modifications in the barrier characteristics (V_B and R_B) of the interaction potential. Further, the collective effect of V_B and R_B obtained from different choices of nuclear density functions has been analyzed in terms of fusion cross-sections calculated using the extended ℓ-summed Wong model. The results are compared with the available experimental data for ^{8}B, ^{18}O, ^{58}Ni and ^{132}Sn+^{58}Ni reactions across the Coulomb barrier energies [16, 19–21]. The mass-asymmetry (η_A) value of the selected choices of nuclear partners covers a wide range and varies from 0 to 0.8.

The data of nuclear density parameters (i.e. half-density radius 'R_0', surface thickness 'a' and wine-bottle parameter 'w') are taken from Refs. [5, 6] for mass-regions A = 4-238, 14-166 and 28-209, respectively, for the 2pF, 3pF and 3pG density functions. However, the data for few nuclei is missing within the given mass regions. Thus, in the present chapter and in [23], the values of R_0, a and w for missing nuclei have been extracted by the polynomials, which are fitted to the available data, of density parameters. Also, the plot of these polynomials as a function of mass number A are shown in Fig.4.2 for 2pF, 3pF and 3pG density functions along with respective data [5,6]. In Table 4.1, a comparison has been

Table 4.1: Comparison of available data [5,6] and calculated values from fitted polynomials of nuclear density parameters, i.e. Half-density radius 'R_0' (fm), surface thickness 'a' (fm) and wine-bottle 'w' (Eqs.(2.29), (2.32) and (2.35)), of different density functions.

Density functions	Mass Number A	Density Parameters					
		Half-density Radius 'R_0'		surface thickness 'a'		wine-bottle 'w'	
		Data	Poly.	Data	Poly.	Data	Poly.
2pF	20	2.740	2.584	0.572	0.501	0.0	0.0
3pF	20	2.791	2.823	0.698	0.564	-0.168	-0.115
3pG	28	1.950	2.112	2.076	2.106	0.286	0.221
2pF	40	3.530	3.637	0.542	0.562	0.0	0.0
3pF	40	3.730	3.733	0.620	0.583	-0.190	-0.584
3pG	54	3.518	3.444	2.270	2.316	0.403	0.305
2pF	62	4.262	4.346	0.521	0.579	0.0	0.0
3pF	62	4.443	4.425	0.539	0.525	-0.209	-0.184
3pG	90	4.434	4.421	2.528	2.552	0.350	0.331
2pF	120	5.315	5.262	0.576	0.534	0.0	0.0
3pF	142	5.614	5.626	0.587	0.589	0.096	0.087
3pG	138	5.338	5.490	2.678	2.638	0.375	0.316
2pF	238	6.805	6.797	0.605	0.554	0.0	0.0
3pF	166	5.980	5.975	0.446	0.445	0.190	0.198
3pG	209	6.315	6.318	2.881	2.882	0.390	0.391

shown between the available data and the calculated values obtained from the polynomials of density parameters. It is evident from the table that, the calculated values are close to the corresponding data for the lighter, intermediate and heavier mass nuclei, selected randomly from Ref. [6]. The results are consistent for all the considered nuclear density functions. Further, the nuclear densities ($\rho(r)$) profile with the variation of radial distance r (fm) obtained with the values of parameters provided in [5,6] are compared with the $\rho(r)$ obtained from the polynomials fitted to the data, as shown in Fig. 4.3. From this figure, it has been observed that, there are nominal difference in the tail and nearby region of $\rho(r)$ obtained from the available data [5,6] and fitted polynomials. Thus, one can use these polynomials for obtaining the values of density parameters of the nuclei for which the data is not available in the literature [6]. Furthermore, in Fig. 4.4 for symmetric and mass-asymmetric target-projectile combinations, the behavior of 2pF, 3pF and 3pG density functions has been investigated in terms of the density distribution of colliding nuclei at touching configuration ($R_t = R_{01}+R_{02}$), for ^{64}Ni-, ^{58}Ni- and ^{48}Ca-based reactions. In the panels (a)-(c) of Fig. 4.4, it has been observed that for the symmetric reactions, projectile density ($\rho_1(r_1)$) of 2pF shows

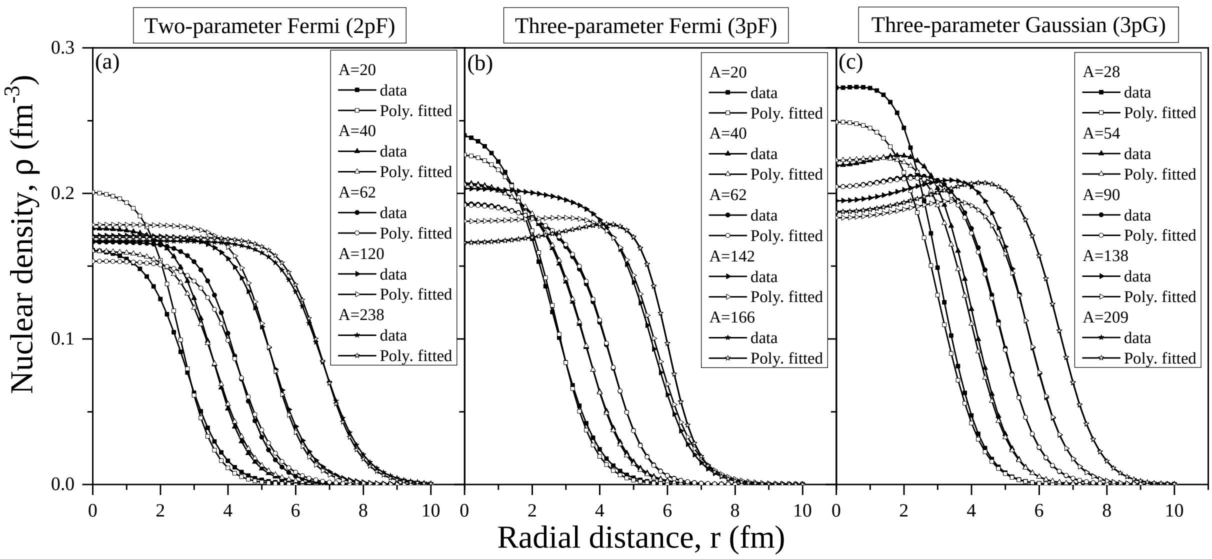

Figure 4.3: Comparison of nuclear density profile, ρ (fm^{-3}), obtained for nuclei belonging to different mass-region using available data [5,6] and fitted polynomials Eqs.(2.29), (2.32) and (2.35), respectively, for (a) 2pF, (b) 3pF and (c) 3pG density functions.

difference in the vicinity of tail region from that of the three parameter density functions (3pF and 3pG), due to larger value of half-density radius of 2pF (R_0^{2pF}) as compared to the radii of 3pF and 3pG density functions (R_0^{3pF} and R_0^{3pG}). On the other hand, from the panels (d)-(l) of Fig. 4.4, it is clear that for mass-asymmetric reactions, $\rho_1(r_1)$ of 3pF and 3pG is higher in the tail and neighborhood region, because of the larger value of R_0^{3pF} and R_0^{3pG} than R_0^{2pF}. It is important to mention here that, the data of 3pG density parameters is not available for the ^{8}B case.

Furthermore, Fig. 4.5 shows the comparison of total interaction potential V_T obtained using 2pF, 3pF and 3pG density functions for ^{58}Ni-based symmetric (^{58}Ni+^{58}Ni) and asymmetric (^{132}Sn, ^{18}O and ^{8}B+^{58}Ni) choices of projectile-target combinations. It has been analyzed for ^{58}Ni+^{58}Ni reaction that, 2pF lowers the barrier height (V_B) due to its larger value of R_0^{2pF} than R_0^{3pF} and R_0^{3pG}. Whereas, for mass-asymmetric reactions, the magnitude of R_0^{3pF} and R_0^{3pG} is larger and the corresponding barrier height V_B is lowered from that of the 2pF case. In order to analyze the effect of different density functions around the Coulomb barrier energy, the fusion cross-sections have been calculated using the extended ℓ-summed Wong model for ^{58}Ni-based mass-symmetric and asymmetric reactions and are compared with the respective experimental data [16,19–21], as shown in Fig. 4.6. It has been analyzed that using the SLy4 Skyrme force parameters, the two parameter density function

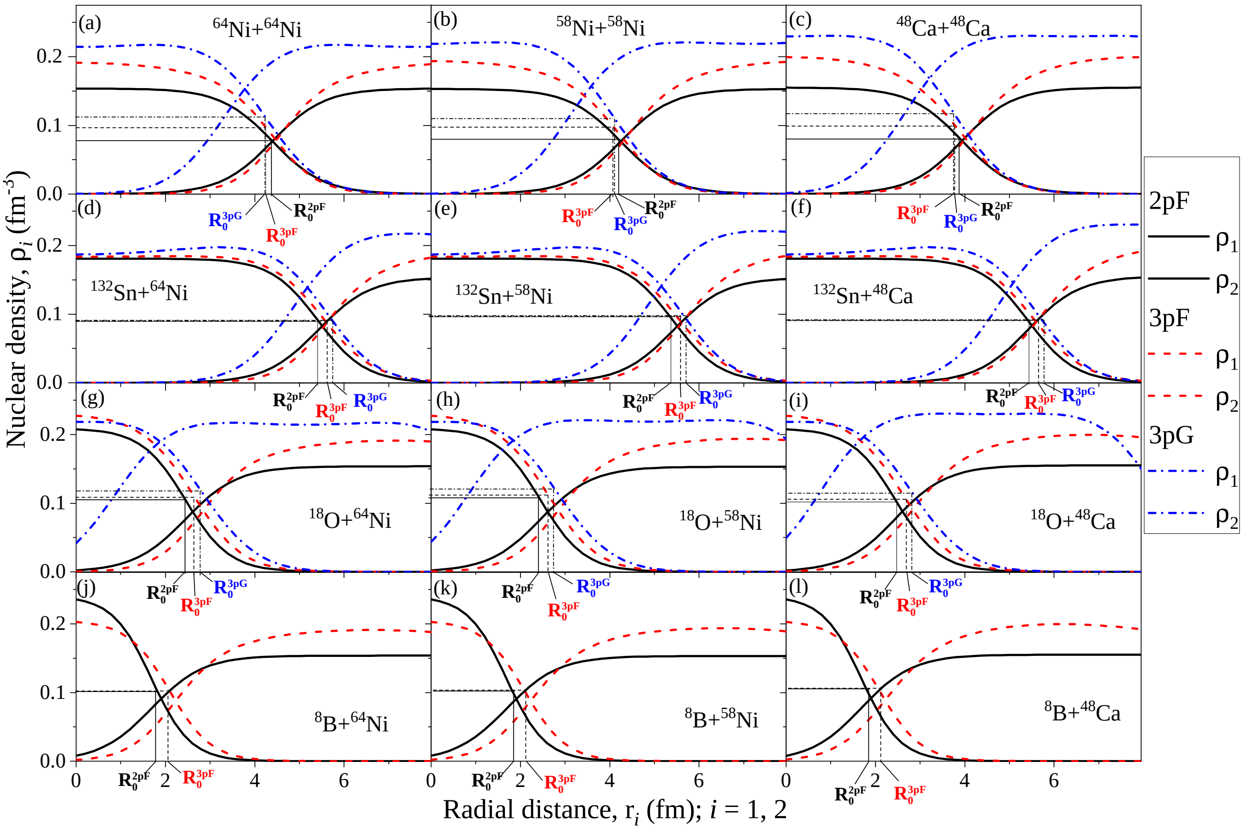

Figure 4.4: The nuclear density profiles (ρ_i (fm^{-3})) using 2pF, 3pF and 3pG functions for (a)-(c) symmetric and (d)-(l) mass-asymmetric ^{64}Ni-, ^{58}Ni- and ^{48}Ca-based reactions, with the variation of radial distance r_i fm.

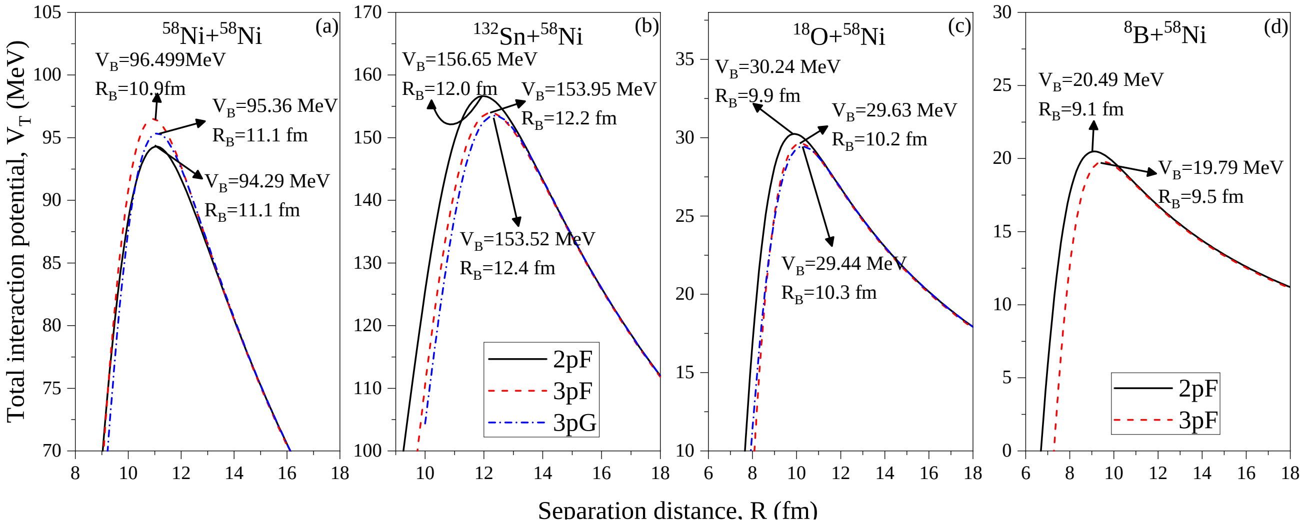

Figure 4.5: The total interaction potential, V_T (MeV) is plotted with respect to separation distance, R (fm) for 2pF, 3pF and 3pG density functions for (a) ^{58}Ni+^{58}Ni, (b) ^{132}Sn+^{58}Ni, (c) ^{18}O+^{58}Ni and ^{8}B+^{58}Ni.

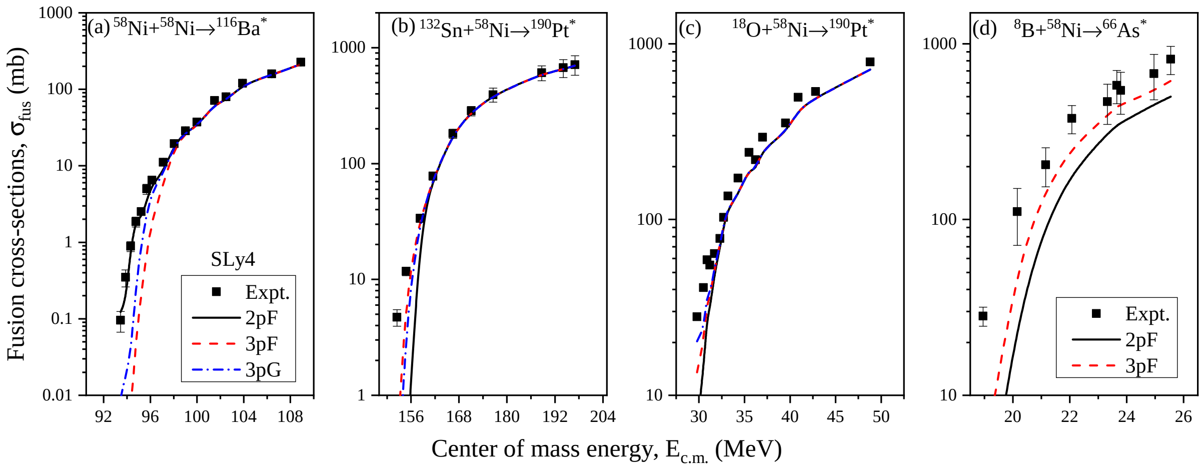

Figure 4.6: The fusion cross-sections, σ_{fus}(mb), calculated within the extended ℓ-summed Wong model using different density functions are compared with the experimental data for (a) ^{58}Ni+^{58}Ni [19], (b) ^{132}Sn+^{58}Ni [16], (c) ^{18}O+^{58}Ni [20] and (d) ^{8}B+^{58}Ni [21].

shows better results at the below-barrier energies for symmetric reaction (^{58}Ni+^{58}Ni, η_A=0), whereas others show fusion hindrance. For the mass-asymmetric reactions i.e. ^{132}Sn, ^{18}O and ^{8}B+^{58}Ni, the three-parameter density functions (3pF and 3pG) seem to perform better in comparison to the 2pF due to the reason explained in the discussion of Fig. 4.5.

4.3 Conclusion

The two-parameter (2pF) and three parameter (3pF and 3pG) density functions used within the semiclassical Skyrme Energy Density Formalism show corresponding effect on the barrier characteristics (barrier position R_B and barrier height V_B), due to relative change in the tail region of nuclear densities. Further, the collective effect of barrier characteristics has been analyzed in the calculation of fusion cross-sections for mass-symmetric and asymmetric kinds of ^{58}Ni-based reactions, which are known to show fusion hindrance below the Coulomb barrier. For the symmetric reaction (^{58}Ni+^{58}Ni), it is observed that, the density profile of 2pF density function is different in the vicinity of tail region from that of the three parameter density functions (3pF and 3pG), which is incepted due to its larger value of half-density radius (or equivalently lower barrier height) as compared to the three parameter density distributions. Consequently, the two parameter Fermi density function reduces the fusion hindrance for ^{58}Ni+^{58}Ni with the use of SLy4. On the other hand, for the case of mass-asymmetric nuclear reaction partners, the 3pF and 3pG density functions has larger half-density radial distance, which in turn, lowers the barrier height in comparison to 2pF case. Hence, the three parameter density functions are found to give better comparison of fusion cross-sections with data, for ^{132}Sn, ^{18}O and ^{8}B+^{58}Ni reactions especially at the below barrier energies. It is worth mentioning here that the tail and nearby region of the density distributions play important role in heavy-ion induced reactions.

Important to mention that, from the results discussed in the Chapters 3 and 4, one can have a comprehensive knowledge over the densities amalgamation processes and nuclear density distributions, and their relevance in the fusion dynamics of considered spherical choices of projectile-target combinations. In the upcoming Chapters, with the use of SEDF approach and different choices of Skyrme forces, we are interested to explore the role of deformations (of different order) and orientations degrees of freedom in nuclear fusion as well as decay mechanisms, at the low-energy regime of heavy-ion induced reactions. In the whole-mass table, there are large variety of nuclei, which possess different shapes like spherical, deformed shapes of axial- and reflection-symmetry (quadrupole, hexadecapole deformed nuclei) and symmetry-breaking pear shapes (octupole deformed nuclei), etc. So, we are interested to explore the significance of symmetry-breaking nuclear shapes of octupole deformed nuclei for the formation of new nuclear entity. The obtained results are going to be discussed in reference to the quadrupole deformed and spherical nuclei.

Bibliography

[1] T. de Forest and J. D. Walecka, Adv. Phys. **15**, 1 (1966).

[2] R. Hofstadter, Ann. Rev. Nucl. Sci. **7**, 231 (1957).

[3] A. -M. Martensson-Pendrill and M. G. H. Gustavsson, in Handbook of Molecular Physics and Quantum Chemistry, edited by Stephen Wilson (Vol.1, Part 6, Chapter 30, pp 477-484, 2003).

[4] L. R. B. Elton, Nuclear sizes (Oxford University Press, London, 1961).

[5] L. R. B. Elton, Proc. Phys. Soc. (London) **A63**, 1115 (1950).

[6] H. De Vries *et al*, Atomic data and Nuclear data tables **36**, 495-536 (1987).

[7] R. Kumar *et al*, Nucl. Phys. A **870-871**, 42-57 (2011).

[8] D. Jain *et al*, Phys Rev. C **85**, 024615 (2012).

[9] D. Jain *et al*, Eur. Phys. J. A **50**, 155 (2014).

[10] I. Sick, Nucl. Phys. A **218**, 509-541 (1974).

[11] C. L. Jiang *et al*, Phys. Rev. Lett. **93**, 012701 (2004).

[12] C. L. Jiang *et al*, Phys. Rev. C **71**, 044613 (2005).

[13] C. L. Jiang *et al*, Phys. Rev. C **82**, 041601 (R) (2010).

[14] K. Hagino, N. Rowley and M. Dasgupta, Phys. Rev. C **67**, 054603 (2003).

[15] S. Misicu and H. Esbensen, Phys. Rev. Lett. **96**, 112701 (2006).

[16] Z. Kohley *et al*, Phys. Rev. Lett. **107**, 202701 (2011).

[17] V. V. Sarsgyan *et al*, Eur. Phys. J. A **49**, 19 (2013).

[18] D. Jain *et al*, Nucl. Phys. A **915**, 106-124 (2013).

[19] M. Beckerman *et al*, Phys. Rev. C **23**, 4 (1981).

[20] A. M. Borges *et al*, Phys. Rev. C **46**, 6 (1992).

[21] E. F. Aguilera *et al*, Phys. Rev. Lett. **107**, 092701 (2011).

[22] M. Bhuyan and R. Kumar, Phys. Rev. C **98**, 054610 (2018).

[23] S. Jain, M. K. Sharma and R. Kumar, Nucl. Phys. A **997**, 121699 (2020).

[24] E. Chabanat *et al*, Nucl. Phys. A **635**, 231-256 (1998).

[25] Li Guo-Qiang, J. Phys. G: Nucl. Part. Phys. **17** 1-34 (1991).

[26] R. Kumar, M. K. Sharma, R. K. Gupta, Nucl. Phys. A **870-871** 42-57 (2011).

[27] S. Jain, R. Kumar and M. K. Sharma, Eur. Phys. J. A **54**, 203 (2018).

[28] R. Kumar *et al*, Phys Rev. C **80**, 034618 (2009).

Chapter 5

Optimum fusion configurations of pear shape nuclei

5.1 Introduction

The shape of an atomic nucleus in its ground state can be spherical or deformed. As the nucleons (either neutron or proton) are added beyond the magic numbers, it causes a long-range correlation and the nuclear shape starts deviating from spherical configuration. The Coulomb excitation is used as a tool to measure the electric transition probabilities of quadrupole (β_2) and octupole (β_3) deformed nuclei [1–4]. The β_2-deformed nuclei, having axial and reflection symmetries, are the most commonly observed deformed nuclei [5–10]. Unlike quadrupole deformed nuclei, it is difficult to observe the effect of the reflection-asymmetry or symmetry-breaking shapes in octupole deformed nuclei. In literature [3, 11–16], there are very few experimentally observed octupole nuclei, and limited cases are reported for proton numbers (Z) = 34, 56, 86, and 88, and neutron numbers (N) = 34, 56, 88, 134, and 136. The presence of octupole deformation in a nucleus enhances the nuclear Schiff moments, which in turn, influences the electric dipole moment. Thus, the octupole deformed nuclei are important in search for permanent electric dipole moments (EDMs) [3, 17]. Also, in the nuclear fusion process, the nonzero EDMs in one of the fusing partners (i.e. ^{16}O+^{224}Ra) show remarkable impact on the fusion barrier and sub-barrier cross-sections [4]. In the present Chapter, we intend to investigate the effect of octupole deformation (up to β_3) in nuclear fusion reaction, which involve β_3-deformed nuclei either as a projectile or target or both, by obtaining the optimum or uniquely fixed orientations for the 'elongated or cold' and 'compact or hot' fusion configurations of the colliding partners. At these fixed orientations, the significance of higher-order deformation (up to β_3) can be explored in the synthesis of heavy and superheavy elements.

As an illustrative case for the graphical representation of deformed nuclei, the deduced β_2-

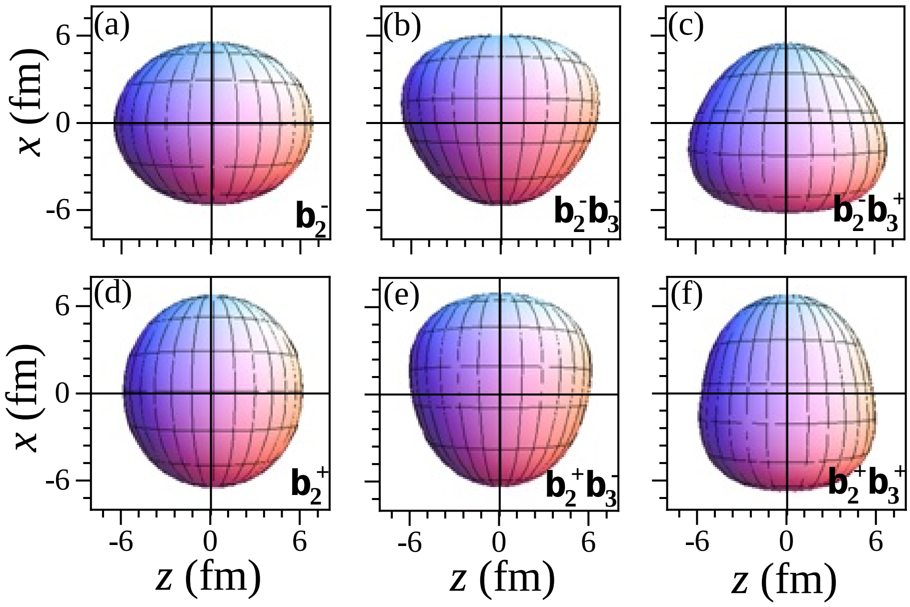

Figure 5.1: The graphical representation of quadrupole [(a) β_2^- and (d) β_2^+] and octupole deformed shapes [(b) $\beta_2^-\beta_3^-$, (c) $\beta_2^-\beta_3^+$, (e) $\beta_2^+\beta_3^-$ & (f) $\beta_2^+\beta_3^+$] of $^{224}_{88}$Ra$_{136}$. Here, $\beta_2^\pm = \pm 0.143$ and $\beta_3^\pm = \pm 0.139$. Horizontal and vertical axes represent the reflection [z (fm)] and axial [x (fm)] axes, respectively.

and β_3-deformed shapes of $^{224}_{88}$Ra$_{136}$ nucleus from the following relation:

$$R_i(\alpha_i) = R_{0i}\left[1 + \sum_{\lambda=2,3} \beta_{\lambda i} Y_\lambda^{(0)}(\alpha_i)\right], \tag{5.1}$$

are represented in Fig. 5.1 for '+' and '-' signs of β_λ; $\lambda = 2, 3$ correspond to quadrupole and octupole deformed shapes, respectively. The quadrupole deformed nuclei, with $\beta_2 < 0$ called oblate - a discus like shape [Fig. 5.1(a)] and $\beta_2 > 0$ called prolate - a rugby ball like shape [Fig. 5.1(d)], have symmetry around the axial and reflection axes. On the other hand, the four possible shapes of octupole deformed nuclei ($\beta_2^-\beta_3^-$, $\beta_2^-\beta_3^+$, $\beta_2^+\beta_3^-$ and $\beta_2^+\beta_3^+$) break symmetry around the reflection axis, as shown in panels (b), (c), (e) and (f) of Fig. 5.1. The axial and reflection-symmetric nuclear shapes are found to play a very important role in the synthesis of heavy and superheavy nuclei [18–26]. Further, in the work of Vitturi *et al* [4], the effect of symmetry-breaking shapes has been tested on the fusion barrier distributions. The sensitivity of barrier distributions to octupole deformed targets, such as ^{144}Ba and ^{224}Ra, was tested using ^{16}O-induced reactions and the corresponding impact on the sub-barrier fusion cross-sections was analyzed. However, the impact of symmetry-breaking pear shapes has not been understood much in the context of fusion dynamics. In the present chapter, the initial step taken in reference to analyze the significance of pear-shape nuclei (belonging to different mass-region of the Periodic Table) on the fusion barriers at the optimized orientations has been discussed in detail. For the formation of a compound nucleus either via cold or hot fusion process, the orientation of a deformed nucleus is fixed or optimized in two ways: (i) the elongated configuration which occurs due to the lowest barrier and largest interaction radius between the centers of two nuclei, and (ii) the most-compact configuration that happens at the highest barrier and smallest interaction radius. The steps (i) and (ii) correspond to the 'optimum cold' and 'optimum hot' fusion configurations, respectively. R. K. Gupta and his collaborators have given the optimum orientations corresponding to the elongated and compact configurations of quadrupole deformed nuclei [21]. In the present Chapter, the effect of octupole deformations along with their +/- signs has been analyzed to optimize the orientations in reference to their elongated and compact fusion configurations. Note that, the nuclei with small and strong octupole deformations are termed as soft- and rigid-pear shaped nuclei, respectively. The hot and cold optimum orientations (θ_{opt}) examined in terms of the barrier position R_B and barrier height V_B with the inclusion of deformations (up to β_3) are discussed below in detail.

5.2 Calculations and results

To examine θ_{opt} with the inclusion of deformations (up to β_3) and orientations effects, we have considered different pairs of projectile-target combinations: spherical-plus-octupole, quadrupole-plus-octupole and octupole-plus-octupole. Here, the projectiles taken into account are spherical (^{16}O, ^{48}Ca and ^{208}Pb) and quadrupole deformed (^{48}Ar, ^{62}Fe and ^{62}Ni) nuclei, and over 700 octupole deformed nuclei belonging to 8$\leq Z \leq$118 are taken as targets of above said P-T combinations. The static quadrupole ($\beta_2^{\pm}$) and octupole deformations ($\beta_3^{\pm}$) of considered deformed nuclei are referred from the recent Nuclear Data Table of Möller *et al* [27]. In Fig. 5.2, the atomic and neutron numbers are shown for nuclei having deformations $\beta_2^{+}\beta_3^{-}$ and $\beta_2^{-}\beta_3^{-}$, which correspond to two different shapes of octupole-deformed nucleus, for convenience see Fig. 5.1. The magnitude of $\beta_3^{\pm}$-deformation possessed by octupole deformed nucleus is either larger or smaller than that of its quadrupole deformation ($|\beta_2^{\pm}|$). Also, in Fig. 1.5(b) of introduction chapter, we have shown the difference in $|\beta_2^{\pm}|$ and $|\beta_3^{\pm}|$ with the variation in the nucleon number. Therefore, the nuclei with (i) larger

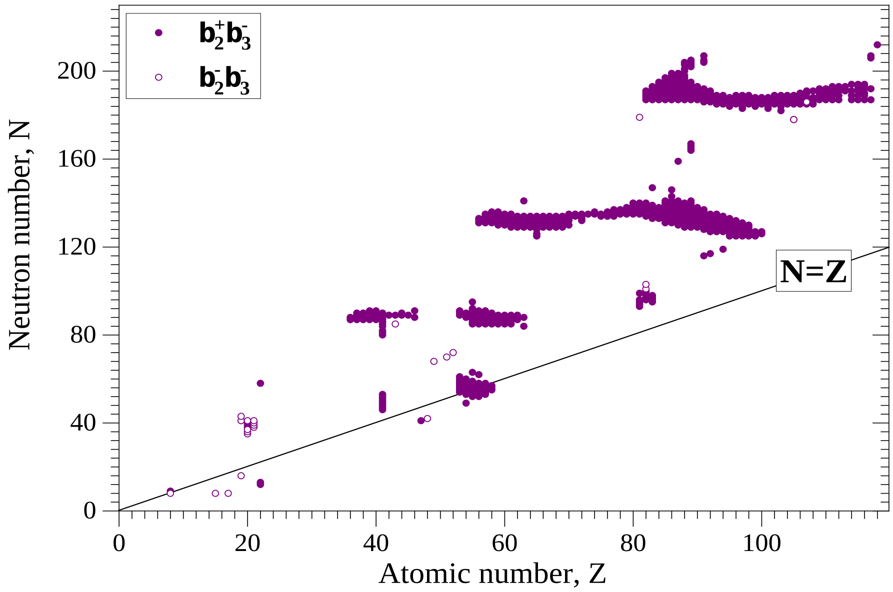

Figure 5.2: The octupole deformed nuclei of $\beta_2^+\beta_3^-$ and $\beta_2^-\beta_3^-$ shapes belonging to different mass-region of Periodic Table. The deformations of more than 700 octupole nuclei are taken from the Data Table of Möller *et al* [27].

value of $|\beta_2^{\pm}|$ than $|\beta_3^{\pm}|$ are called as soft-pear shapes and (ii) smaller value of $|\beta_2^{\pm}|$ than $|\beta_3^{\pm}|$ are defined as rigid-pear shapes. In view of this, the present chapter discusses about the hot and cold optimum orientations of soft and rigid pear-shape nuclei for spherical-octupole and deformed-octupole colliding nuclear partners. For the above analysis, the semiclassical Skyrme Energy Density Formalism and phenomenological model based proximity potentials have been taken into account, to derive nucleus-nucleus interaction potential, which contributes in determining the fusion barrier characteristics (barrier position R_B and barrier height V_B).

To have an explicit role of octupole deformations in heavy-ion induced reactions, initially, the spherical-plus-octupole deformed combination (i.e. ^{48}Ca+^{144}Ba reaction) is considered and analyzed the corresponding effect of β_3 on V_B and R_B obtained using Proximity potential of Blocki *et al* [28], as illustrated in Fig. 5.3. From this figure, one can observe that, the influence of octupole deformation has been observed initially by considering spherical and then quadrupole and at last the octupole deformed shape of ^{144}Ba target nucleus. In Fig. 5.3, the barrier height V_B and barrier position R_B are shown with respect to the orientation (θ_2) of target nucleus. The magnitude of V_B and R_B remains same over all the orientations of spherical configuration of target nucleus. Further, with the inclusion of only quadrupole deformation ($\beta_{22} = 0.163$) of ^{144}Ba, one can see the modification in V_B and R_B from that of

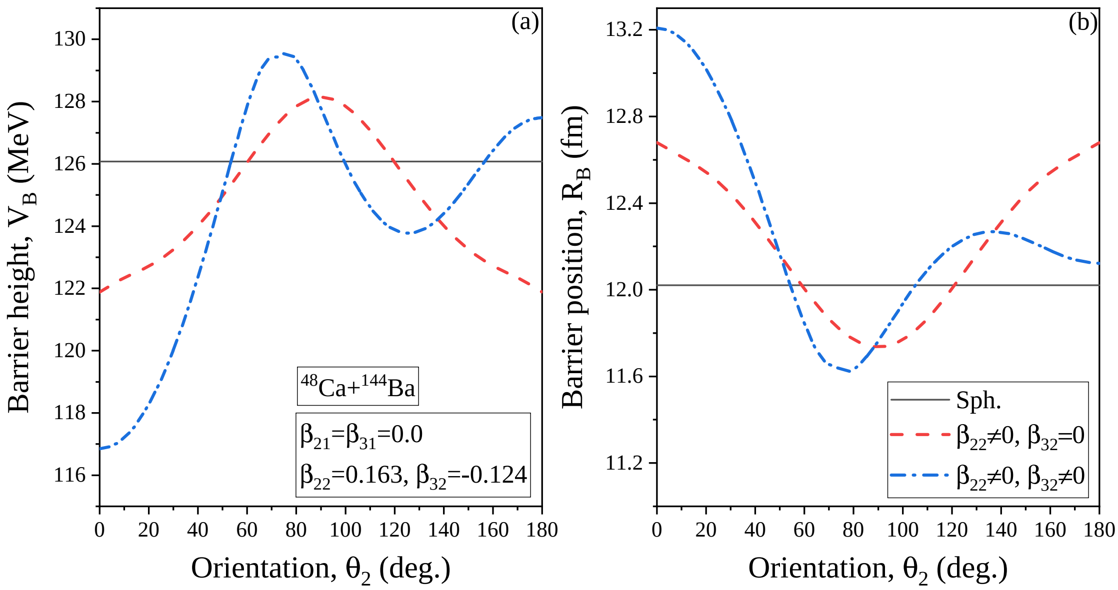

Figure 5.3: The variation of (a) barrier height V_B (MeV) and (b) barrier position R_B (fm) is shown with respect to the orientation of spherical/deformed (up to β_3) target of ^{48}Ca+^{144}Ba reaction.

spherical case, as moving from $\theta_2 = 0^o$ to 180^o. Also note that, due to β_2, there is symmetry in the barrier characteristics around 90^o. Since, the quadrupole deformed nuclear shapes have symmetry around axial (x) and reflection (z) axes, for reference see panels (a) and (d) of Fig. 5.1. On the other hand, the octupole deformed nuclei of pear-shape break symmetry around reflection axis (see Fig. 5.1(b), (c), (e) and (f)). Due to this fact, one can see an asymmetrical behavior of V_B and R_B over all values of θ_2, with the inclusion of deformations up to β_3. Also, note that, due to deformations up to β_{22}, the highest barrier height V_B and corresponding smallest R_B come at θ_2=90^o, which is the case for hot or compact fusion configuration of quadrupole deformed nucleus. For cold or elongated fusion configuration for β_2^- deformed nuclei, the lowest and highest values of V_B and R_B, respectively, come at θ_2=0^o and 180^o. On the other hand, with the consideration of deformations up to β_3, the orientation angles θ_2^{hot} and θ_2^{cold} obtained are 76^o and 0^o, respectively. From this observation, one can say that due to octupole deformation, the uniquely fixed optimum orientations get modified from that obtained for quadrupole deformation.

Further, in Fig. 5.4, a comparative analysis has been observed for phenomenological model based proximity potential derived by Blocki *et al* [28] and Skyrme Energy Density Formalism based potential, which get influenced for different sets of Skyrme force parameters. Here, we have considered some older versions (SIII [29], SkT1 [30], SLy4 [31] and eMSL07 [32]) and

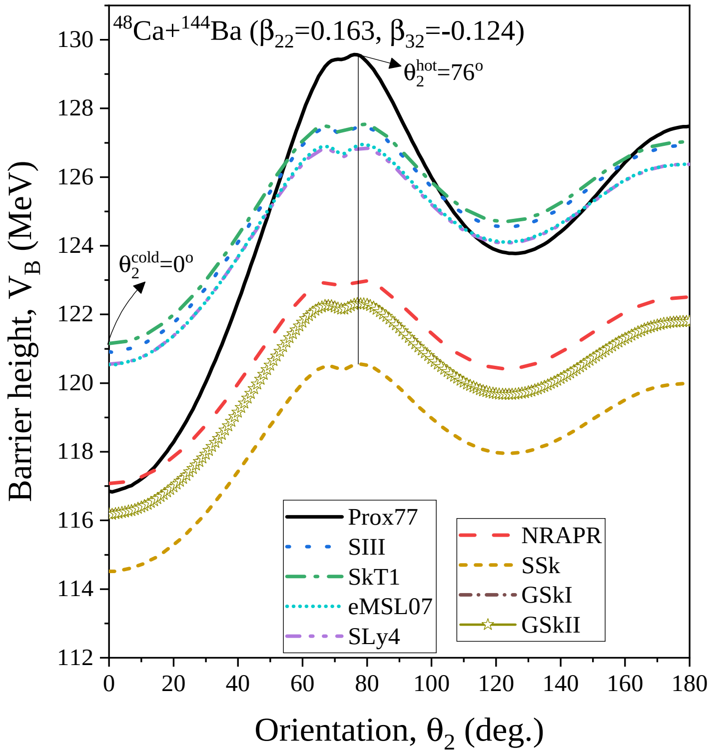

Figure 5.4: A comparison of phenomenological potential (Prox77) and SEDF based potential (SIII, SkT1, eMSL07, SLy4, NRAPR, SSk, GSkI and GSkII) is shown in terms of barrier height V_B (MeV) with respect to the orientation (θ_2) of octupole deformed target of ^{48}Ca+^{144}Ba (β_{22} = 0.163, β_{32} = -0.124) reaction.

modified versions of Skyrme force parameters (NRAPR [33], SSk, GSkI and GSkII [34]). From Fig. 5.4, one can clearly observe the modification in the magnitude of barrier height, due to different choices of nuclear potentials, over all the orientations (θ_2) of octupole deformed target of ^{48}Ca+^{144}Ba reaction. However, with the inclusion of deformations up to β_3, the optimized angles θ_2^{opt} for the hot and cold fusion configurations of β_3-deformed nuclei are independent of the choice of nuclear potential. Therefore, in further calculations, the nuclear potential of Prox77 [28] has been taken into account to analyze the exclusive role of β_3-deformed nuclei on fusion barrier, in reference to β_2-deformed nuclei, by considering different projectile-target combinations, i.e. quadrupole-plus-octupole and octupole-plus-octupole deformed pairs of colliding nuclear partners.

In Fig. 5.5, the color mapping represent the variation of barrier height V_B over all the orientations (θ_1, θ_2) of deformed projectile and target nuclei. For ^{48}Ar (β_{21} = -0.205), ^{62}Fe (β_{21} = 0.152) and ^{144}Ba (β_{21} = 0.163, β_{31} = -0.124)+^{144}Ba (β_{22} = 0.163, β_{32} = -0.124) reactions, the highest and lowest values of V_B come at θ_2^{opt}(hot) = 76^o and θ_2^{opt}(cold) = 0^o, respectively. From this figure, one can observe that, the hot and cold optimum orientations obtained for

octupole deformed target are independent of the choice of projectiles. In further calculations, the octupole deformed nuclei of soft- and rigid-pear shapes have been considered in order to explore the influence of magnitude as well as +/- sign of β_3-deformation on θ_{opt}.
In Figs. 5.6 and 5.7, the variation of V_B and R_B is shown with respect to the orientation θ_2 of deformed target of ^{48}Ca+soft-pear (^{110,111,148}La, ^{224,226,232}Rn) and rigid-pear shape (^{274,276,280}Rn, ^{276,278,280}Ac) combinations. For spherical projectile ^{48}Ca, the orientation angle θ_1 remains fixed and can be taken either as 0^o or 180^o. In these figures, the elongated configuration of colliding nuclei corresponds to the lowest barrier height and largest interaction radius or barrier position, which refers to the cold optimum orientation. For the case of compact configuration, the highest barrier and smallest interaction radius stand for the hot optimum orientation. It is worth noting that, in Data Table [27], β_3 deformations are given for $\beta_2^-\beta_3^-$ and $\beta_2^+\beta_3^-$ shapes. The optimum orientations for the rest shapes of octupole deformed nuclei ($\beta_2^-\beta_3^+$ and $\beta_2^+\beta_3^+$) are predicted and reported in Table 5.1 by changing the signs of available data for β_3^-. The table presents the optimum orientations (θ_{opt}) for octupole deformed nucleus of soft- (with small value of β_3) and rigid-pear shape (with large value of β_3). In Table 5.1, θ_{opt} for the cold and hot configurations of oblate shape (quadrupole; β_2^-) are 90^o and 0^o (or 180^o), respectively. Note that, the spherical-symmetric shapes (quadrupole deformed nucleus) have the same configurations at 0^o and 180^o, however, the symmetry-breaking (octupole deformed) nuclei have different shapes at these angles. Due to this fact, the angular separation between $\theta_{opt}|_{\beta_2}$ and $\theta_{opt}|_{\beta_3}$ depends on the strength and sign of octupole deformation. For the case of the soft-pear shape (i.e. $|\beta_2| > |\beta_3|$), θ_{opt} for the elongated configuration of β_2^- changes with a maximum of 20^o, whereas the rigid-pear shape ($|\beta_2| \leq |\beta_3|$) shifts it by 90^o. Similar results are observed for the β_2^+ case, but for the compact configuration. Depending on the magnitude of β_3 of soft-pear shapes, $\theta_{opt}|_{\beta_3}$ comes with an addition or subtraction of 2^o.
It is important to note that the optimum angles change significantly with the magnitude of deformation of soft-pear shape nuclei. So, the deviations observed in the cold and hot optimum cases for β_2^- and β_2^+, respectively, are categorized in three regions, which show difference between the magnitude of β_2 and β_3, as (1) $|\beta_2|-|\beta_3| \geq 0.2$, (2) $0.1 \leq |\beta_2|-|\beta_3| < 0.2$, and (3) $0 < |\beta_2| - |\beta_3| < 0.1$. These regions have also been exercised for spherical-deformed and deformed-deformed colliding nuclear partners, which involve deformations up to β_3 (see Table 5.1 and Fig. 2.1 for more details). The considered pear-shapes belong to different

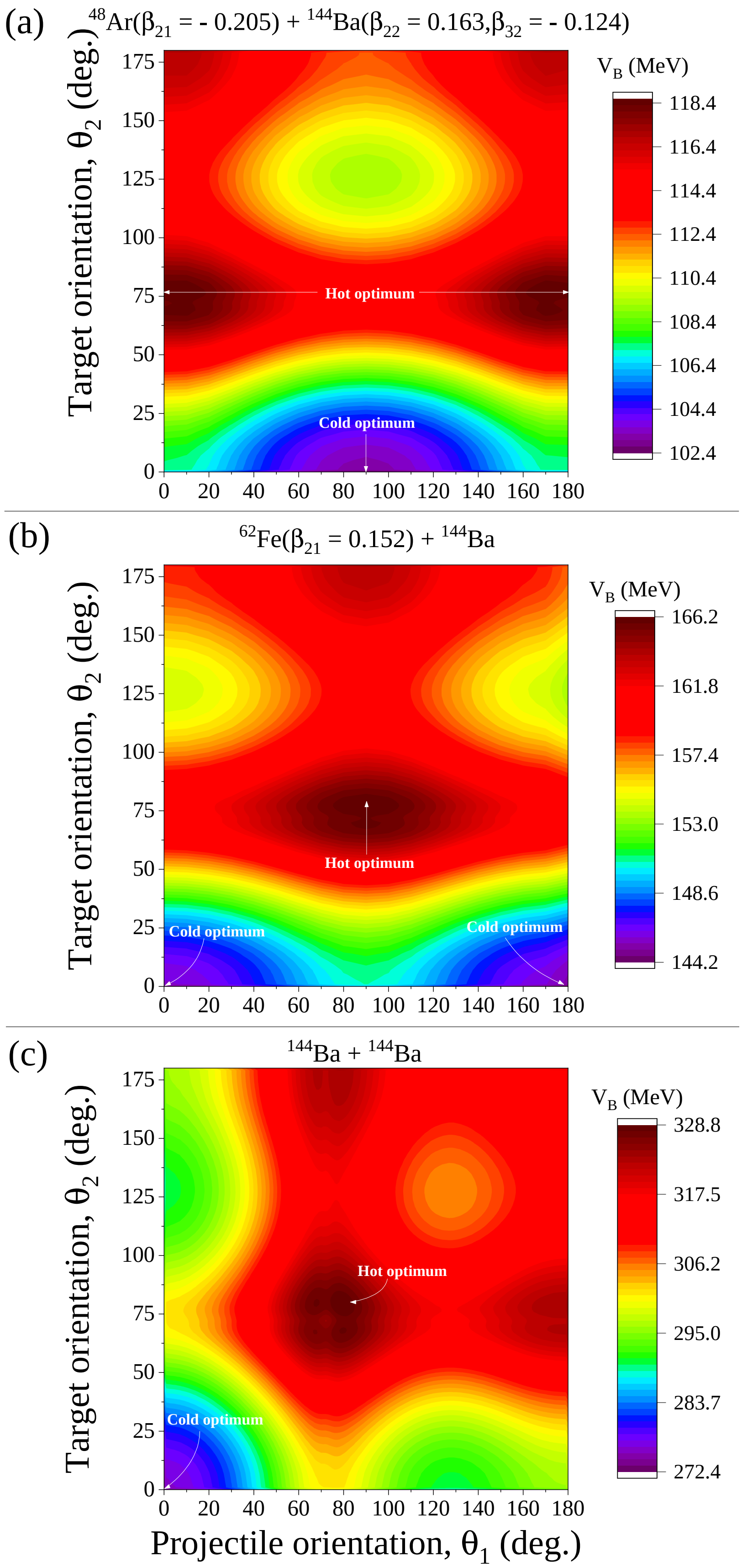

Figure 5.5: The color mapping represent the variation in barrier height V_B (MeV) over the relative orientations (θ_1, θ_2) of deformed projectile-target combinations: (a) ^{48}Ar (β_{21} = -0.205), (b)^{62}Fe (β_{21} = 0.152) and (c)^{144}Ba (β_{21} = 0.163, β_{31} = -0.124)+^{144}Ba (β_{22} = 0.163, β_{32} = -0.124) combinations.

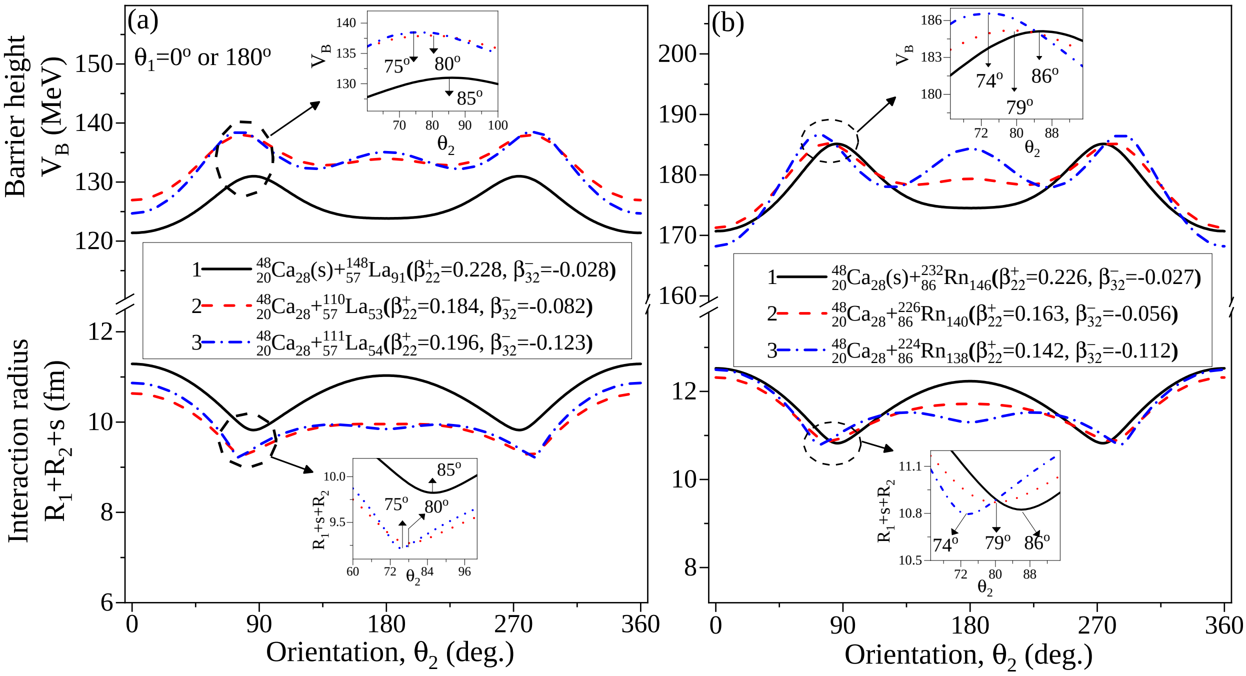

Figure 5.6: The variation of barrier height V_B and interaction radius $(R_1 + R_2{+}s)$ with respect to the orientation (θ_2) of soft-pear shape nuclei in ^{48}Ca (sph.) + (a) ^{110,111,148}La and (b) ^{224,226,232}Rn reactions. The difference between the magnitude of β_2 and β_3 is categorized as: (1) $|\beta_2| - |\beta_3| \geq 0.2$, (2) $0.1 \leq |\beta_2| - |\beta_3| < 0.2$ and (3) $0 < |\beta_2| - |\beta_3| < 0.1$.

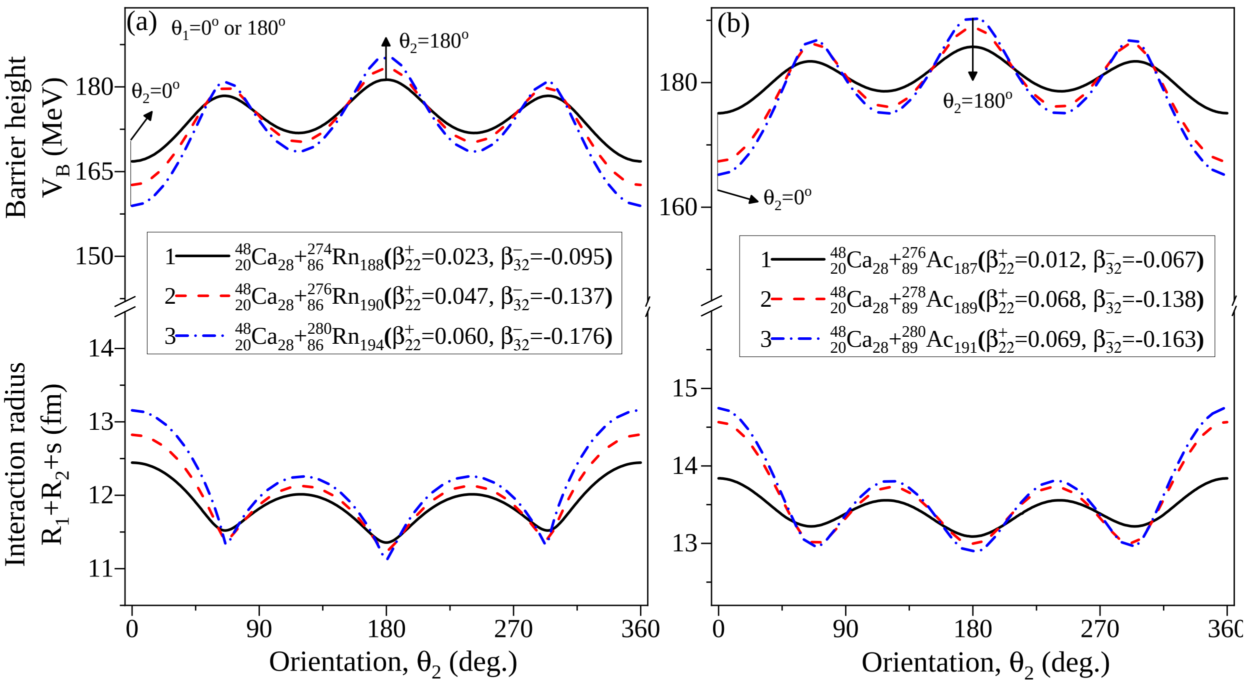

Figure 5.7: Same as Fig.5.6, but for rigid-pear shape nuclei (as target) in ^{48}Ca (sph.) + (a) ^{274,276,280}Rn and (b) ^{276,278,280}Ac reactions.

Table 5.1: Optimum orientations (θ_{opt}) for octupole deformed nuclei, of soft- and rigid-pear shape nuclei, leading to 'cold or elongated' and 'hot or compact' configurations.

shape	deformation		Optimum configuration $\theta_2^{opt.}$(deg.)	
			'elongated or cold'	'compact or hot'
oblate	β_2^-		90^o	0^o or 180^o
$\lvert\beta_2\rvert > \lvert\beta_3\rvert$ soft-pear shape	$\beta_2^-\beta_3^-$	$\lvert\beta_2^-\rvert - \lvert\beta_3^-\rvert \geq 0.2$	$100^o \pm 2^o$†	180^o
		$0.1 \leq \lvert\beta_2^-\rvert - \lvert\beta_3^-\rvert < 0.2$	$105^o \pm 2^o$	180^o
		$0 < \lvert\beta_2^-\rvert - \lvert\beta_3^-\rvert < 0.1$	$110^o \pm 2^o$	180^o
	$\beta_2^-\beta_3^+$	$\lvert\beta_2^-\rvert - \lvert\beta_3^+\rvert \geq 0.2$	$85^o \pm 2^o$	0^o
		$0.1 \leq \lvert\beta_2^-\rvert - \lvert\beta_3^+\rvert < 0.2$	$80^o \pm 2^o$	0^o
		$0 < \lvert\beta_2^-\rvert - \lvert\beta_3^+\rvert < 0.1$	$75^o \pm 2^o$	0^o
rigid-pear shape $\lvert\beta_2\rvert \leq \lvert\beta_3\rvert$	$\beta_2^-\beta_3^-$		0^o	180^o
	$\beta_2^-\beta_3^+$		180^o	0^o
prolate	β_2^+		0^o or 180^o	90^o
$\lvert\beta_2\rvert > \lvert\beta_3\rvert$ soft-pear shape	$\beta_2^+\beta_3^-$	$\lvert\beta_2^+\rvert - \lvert\beta_3^-\rvert \geq 0.2$	0^o	$85^o \pm 2^o$
		$0.1 \leq \lvert\beta_2^+\rvert - \lvert\beta_3^-\rvert < 0.2$	0^o	$80^o \pm 2^o$
		$0 < \lvert\beta_2^+\rvert - \lvert\beta_3^-\rvert < 0.1$	0^o	$75^o \pm 2^o$
	$\beta_2^+\beta_3^+$	$\lvert\beta_2^+\rvert - \lvert\beta_3^+\rvert \geq 0.2$	180^o	$100^o \pm 2^o$
		$0.1 \leq \lvert\beta_2^+\rvert - \lvert\beta_3^+\rvert < 0.2$	180^o	$105^o \pm 2^o$
		$\lvert\beta_2^+\rvert - \lvert\beta_3^+\rvert < 0.1$	180^o	$110^o \pm 2^o$
rigid-pear shape $\lvert\beta_2\rvert \leq \lvert\beta_3\rvert$	$\beta_2^+\beta_3^-$		0^o	180^o
	$\beta_2^+\beta_3^+$		180^o	0^o

† The values of optimum orientations for soft-pear shape nuclei come within the range of $\theta_2^{opt.} \pm 2^o$.
Note: The optimum orientations obtained for octupole deformed nuclei are developed on the basis of proximity theorem based nuclear potential (see Eq.(2.10)), but is valid for any type of nuclear interaction.

mass regions of the Periodic Table.

This Chapter shows the effect of the sign and magnitude of β_3 deformation for both the compact and noncompact fusion configurations of two colliding nuclei. Unlike quadrupole deformed nuclei, there are less numbers of experimentally observed octupole nuclei [3,11–16]. That is why the importance of pear-shape nuclei has not been exposed much so far in the field of nuclear reactions. On the basis of our theoretical work, an application of optimized orientations for octupole deformed nuclei is made in the calculation of fusion cross-sections (σ_{fus}) using the Wong formula [35] for the reaction ^{48}Ca+^{220}Rn (β_2 = 0.110, β_3 = -0.125), forming a superheavy compound nucleus ^{268}Sg*, as a function of excitation energies E^*_{CN} (or center of mass energy $E_{c.m.}$). The relevant details are provided in Table 5.2. Since the experimental data of this reaction involving the octupole deformed nuclei are not available,

Table 5.2: The calculated fusion cross-sections $\sigma_{fus.}$(mb) using Wong formula [35] are given as a function of excitation energy E^*_{CN} (and corresponding center of mass energy $E_{c.m.}$(MeV)) of an excited compound nucleus ^{268}Sg* [36] formed from ^{48}Ca (sph.)+^{220}Rn ($\beta_2 = 0.110$ and $\beta_3 = -0.125$) reaction.

E^*_{CN} (MeV)	$E_{c.m.}$ (MeV)	Fusion cross-sections ($\sigma_{fus.}$(mb))				
		sph.	β_2		β_2, β_3	
			cold	hot	cold	hot
34.67	182.06	14.821	138.132	0.831	472.519	0.129
38.67	186.06	113.204	225.469	49.567	595.856	19.751
43.67	191.06	245.612	395.265	177.279	742.765	144.819
48.67	196.06	371.322	527.931	299.821	882.181	272.095
53.67	201.06	490.780	653.998	416.269	1014.662	393.049
58.67	206.06	604.441	773.947	527.067	1140.714	508.135
63.67	211.06	712.717	888.214	632.615	1260.794	617.767
68.67	216.06	815.981	997.191	733.277	1375.316	722.325
78.67	226.06	1008.805	1200.684	921.244	1589.163	917.566

so for the sake of comparison, the calculated fusion cross section is compared with the experimental data [36] of the ^{30}Si+^{238}U reaction, which forms the same compound nucleus, i.e., ^{268}Sg*. It is found that the $\sigma_{fus.}$(mb) obtained for the hot configuration of β_3-deformed nuclei (^{220}Rn) seems to be comparable with the experimental data [36]. In addition to this, the calculations have also been done for the formation of a heavy compound nucleus, i.e. ^{190}Ir* formed from ^{48}Ca (sph)+^{142}La($\beta_2 = 0.108$ and $\beta_3 = -0.083$) reaction, and the fusion cross-sections obtained with the inclusion of β_3 are comparable with the data of ^{9}Be+^{181}Ta [37] reaction, which forms the same compound nucleus i.e. ^{190}Ir*. The results obtained for the synthesis of heavy and super-heavy elements from the octupole-based reactions can be verified in the future experiments. Also, the importance of optimized orientations for different combinations of colliding partners will be explored in the upcoming chapter.

5.3 Conclusions

The octupole deformation (up to β_3) distorts the spherically symmetric or quadrupole deformed (β_2) nuclei into a pear shape. In this chapter, the optimum (or uniquely fixed) orientations obtained for the 'elongated' and 'compact' fusion configurations of octupole β_3-deformed nuclei have been obtained which are different from the ones reported for the quadrupole deformed nuclei. The soft-pear shape nuclei with small β_3 deformations (i.e. $|\beta_2| > |\beta_3|$) show a maximum deviation of 20^o in the elongated and compact configurations of oblate and prolate cases, respectively, whereas for rigid-pear shape nuclei with strong β_3 deformation ($|\beta_2| \leq |\beta_3|$), the deviation observed is 90^o. The optimum orientations obtained are also dependent on the '+' and '-' signs of β_3-deformation. Thus, the octupole deformations significantly modify the optimum orientations for the cold and hot fusion configurations and hence leads to modification of the barrier characteristics. In addition to this, the effects of β_3 have also been observed in the calculation of fusion cross section for the formation of heavy (^{190}Ir*) and superheavy (^{268}Sg*) elements formed from the octupole-based reactions, i.e., ^{48}Ca(sph.)+^{142}La (β_2 = 0.108, β_3 = -0.083) and ^{220}Ra (β_2 = 0.110, β_3 = -0.125), respectively.

On the basis of above results, it would be interesting to explore the significance of octupole deformation and related optimum orientations on the fusion barrier characteristics and subsequently on the fusion cross-sections over a wide range of beam energies. To carry forward with the above idea, in the next Chapter, the fusion dynamics of a large variety spherical-plus-octupole deformed pairs of colliding nuclei would be analyzed and discussed in detail.

Bibliography

[1] H. Wollersheim *et al*, Nucl. Phys. A **556**, 261 (1993).

[2] ZHU Sheng-Jiang *et al*, Chin. Phys. Lett. **14**, 569 (1997).

[3] L. P. Gaffney *et al*, Nature **497**, 199 (2013).

[4] R. Kumar, J. A. Lay and A. Vitturi, Phys. Rev. C **92**, 054604 (2015).

[5] D. R. Bès and Z. Szymanski, Nucl. Physics **28**, 42-62 (1961).

[6] C. W. Towsley *et al*, Nucl. Phys. A **204**, 574-592 (1973).

[7] R. W. Ibbotson *et al*, Phys. Rev. Lett. **80**, 10 (1998).

[8] E. Nacher *et al*, Phys. Rev. Lett. **92**, 23 (2004).

[9] A. Gorgen and W. Korten, J. Phys. G: Nucl. Part. Phys. **43**, 024002 (2016).

[10] N. T. Jarallah, Energy Procedia **157**, 276-282 (2019).

[11] W. Nazarewicz, P. Olanders and I. Ragnarsson, Nucl. Phys. A **429**, 269-295 (1984).

[12] I. Ahmad and P. A. Butler, Annu. Rev. Nucl. Part. Sci. **43**, 71-116 (1993).

[13] P. A. Butler and W. Nazarewicz, Rev. Mod. Phys. **68**, 349-421 (1996).

[14] P. A. Butler, J. Phys. G: Nucl. Part. Phys. **43**, 073002 (2016).

[15] B. Bucher *et al*, Phys. Rev. Lett. **116**, 112503 (2016).

[16] S. J. Zhu *et al*, Phys. Rev. Lett. **124**, 032501 (2020).

[17] W. Urban *et al*, Nucl. Phys. A **613**, 107-131 (1997).

[18] R. K. Gupta, A. Sandulescu and W. Greiner, Z. Naturforsch **32a**, 704 (1973).

[19] A. Sandulescu *et al*, Phys. Rev. Lett. B **60**, 225 (1976).

[20] K. Morita *et al*, J. Phys. Soc. Japan **73**, 2593 (2004).

[21] R. K. Gupta *et al*, J. Phys. G: Nucl. Part. Phys. **31**, 631-644 (2005).

[22] M. Manhas *et al*, Phys. Rev. C **74**, 034603 (2006).

[23] R. K. Gupta, M. Manhas and W. Greiner, Phys. Rev. C **73**, 054307 (2006).

[24] M. Ismail *et al*, Can. J. Phys. **92**, 1411-1418 (2014).

[25] S. Chopra *et al*, Phys. Rev. C **98**, 041603 (R) (2018).

[26] G. Kaur, K. Hagino and N. Rowley, Phys. Rev. C **97**, 064606 (2018).

[27] P. Möller *et al*, At. Data and Nucl. Data Tables **109-110**, 1-204 (2016).

[28] J. Blocki *et al*, Ann. Phys., NY **105**, 427 (1977).

[29] M. Beiner *et al*, Nucl. Phys. A **238**, 29 (1975).

[30] F. Tondeur *et al*, Nucl. Phys. A **420**, 297 (1984).

[31] E. Chabanat *et al*, Nucl. Phys. A **635**, 231 (1998).

[32] Z. Zhang and Lie-Wen Chen, Phys. Rev. C **94**, 064326 (2016).

[33] A. W. Steiner *et al*, Phys. Rep. **411**, 325 (2005).

[34] B. K. Agrawal, S. K. Dhiman and R. Kumar, Phys. Rev. C **73**, 034319 (2006).

[35] C. Y. Wong, Phys. Rev. C **31**, 766 (1973).

[36] K. Nishio *et al*, Phys. Rev. C **82**, 044604 (2010).

[37] N. T. Zhang *et al*, Phys. Rev. C **90**, 024621 (2014).

Chapter 6

Impact of octupole deformations and related orientations in fusion process

6.1 Introduction

In Chapter 5, we have proposed a new set of optimum or uniquely fixed orientations, which are different from the values reported for the quadrupole β_2 deformed nuclei, with the consideration of deformations up to β_3 [1]. In the above analysis, it has been observed that, the soft-pear shape of octupole deformed nucleus with small β_3 deformations shows a maximum deviation of 20^o in the elongated and compact configurations of oblate and prolate cases, respectively. On the other hand, for the rigid-pear shape nuclei with strong β_3 deformation, the deviation observed in θ_{opt} is 90^o. In the present chapter, the impact of nuclear deformations (up to β_3) and the related optimum orientation degrees of freedom has been analyzed in terms of barrier characteristics and subsequently on the fusion cross-sectional area for a large variety of spherical-plus-deformed pairs of colliding nuclei forming new nuclear entities belonging to different mass-regions of the Periodic Table.

For the synthesis of heavy and superheavy elements, either of the two nuclear mechanisms, namely hot and cold fusion processes, are used [2–6]. These fusion phenomena have been described successfully when either one or both the colliding nuclear partners are deformed [7–10]. The theories used to illustrate the concept of hot and cold fusion processes are developed on the uniquely fixed or optimum orientation of quadrupole and octupole deformed nuclei [11–13]. Here, the considered octupole nuclei belonging to different masregions of the Periodic Table are categorized as (i) the nuclei with weak or small octupole deformation compared to quadrupole deformation and (ii) the nuclei with strong octupole deformation. The first type of configuration is called as the soft-pear shape ($|\beta_2| > |\beta_3|$) and the second is called the rigid-pear shape ($|\beta_2| \leq |\beta_3|$). The main objective of the present chapter is to investigate in detail the influence of cold and hot optimum oriented octupole

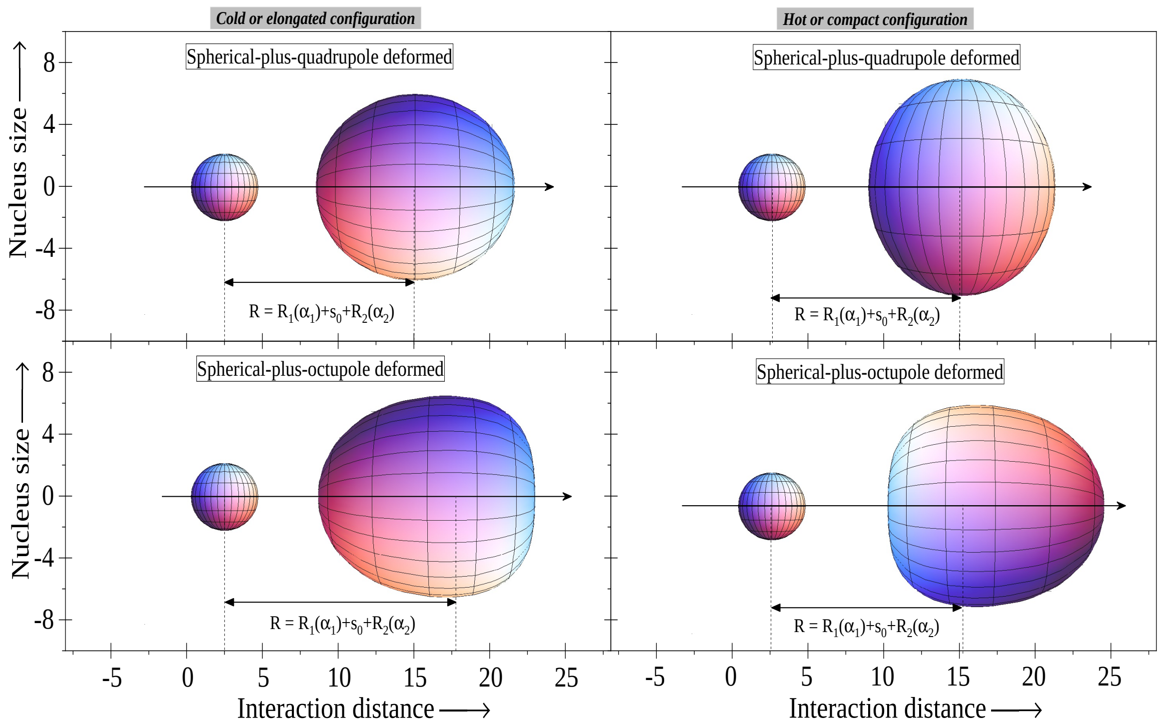

Figure 6.1: The graphical representation of 'cold or elongated' and 'hot or compact' fusion configurations for ^{16}O+^{280}Ra (β_{22} = 0.069, β_{32} = -0.163) reaction. The above panel represents spherical-plus-quadrupole deformed combination, and lower one is for spherical-plus-octupole deformed colliding partners.

deformed nuclei on the fusion barrier characteristics (V_B and R_B) and hence on the fusion cross-sections for energies across the Coulomb barrier.

The deformation and orientation degrees of freedom are introduced in the interaction potential through the spherical harmonic function of nuclear radii terms (Eq.(2.1)). The radius of a nucleus is estimated from the center to the surface region. Unlike quadrupole (β_2) deformed nuclei, the center point of symmetry-breaking pear shape is not situated exactly at the center. One can visualize (in the graphical representation of Fig. 6.1) the change in the interaction distance between the centers of the spherical-octupole pairs of colliding nuclei and that of spherical-quadrupole combination for the cold/noncompact and hot/compact fusion configurations. This point motivates us to observe the corresponding effects on the fusion barrier (V_B and R_B) as well as the fusion cross-sections (σ_{fus}). To extract the exclusive role of deformations up to octupole, the β_3 based results are compared with the corresponding β_2-case [14]. To study the 'cold' and 'hot' optimum cases of octupole deformed nuclei in nuclear fusion reactions, the static deformations are considered [15]. The dynamical effect of quadrupole, octupole, or higher-order deformations will be explored for the fusion-fission mechanisms in the future research.

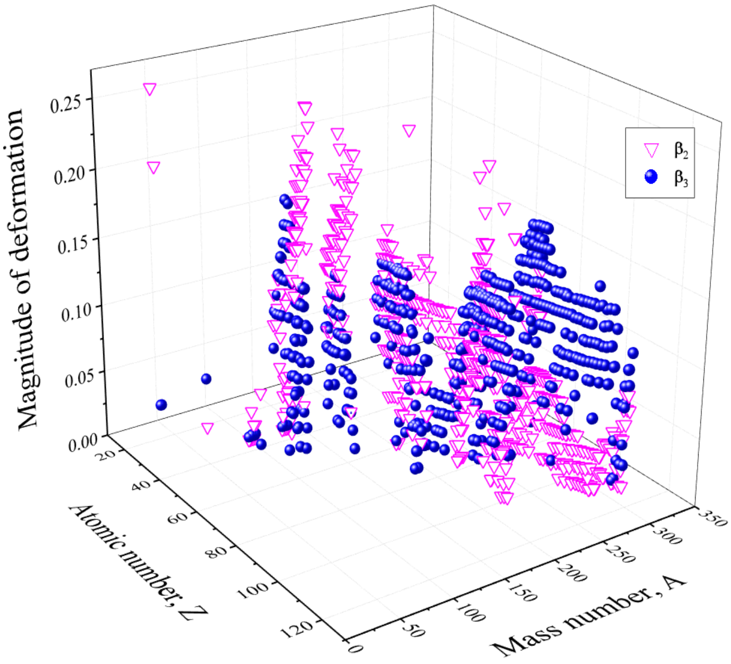

Figure 6.2: The magnitude of deformations, provided in Nuclear Data Table [15], shown here for nuclei belonging to different mass-region of the Periodic Table.

The above study explores the effect of octupole deformation and the related optimum orientations on approximately 200 spherical-octupole pairs of colliding nuclei. For this combination, the doubly magic nuclei ^{16}O and ^{48}Ca are used as projectiles to strike an octupole deformed target. The considered soft- and rigid-pear shapes of octupole belong to different mass-regions of the Periodic Table.

6.2 Calculations and results

There are approximately 700 deformed nuclei that have both the quadrupole β_2 and octupole β_3 deformations [15]. The magnitude of β_2 and β_3 deformations for these 700 nuclei shown in Fig. 6.2 is represented by the open triangle and solid circle symbols, respectively. From this figure, one can identify the nuclei that have a larger β_2 magnitude than β_3 magnitude (also called as soft-pear shapes of octupole deformed nuclei) and nuclei with larger value of $|\beta_3|$ than $|\beta_2|$ (named as rigid-pear shapes of octupole deformed nuclei), also see Fig. 1.5. Most of the soft-pear shapes exist in the regions Z = 53-60 and 76-88 with a mass range A = 103-115, 140-150, 188-195, and 210-230. Its rigid counterparts are found in abundance in the regions Z = 37-40, 59-68, and $>$80 with the masses A = 124-131, 189-196, 215-224,

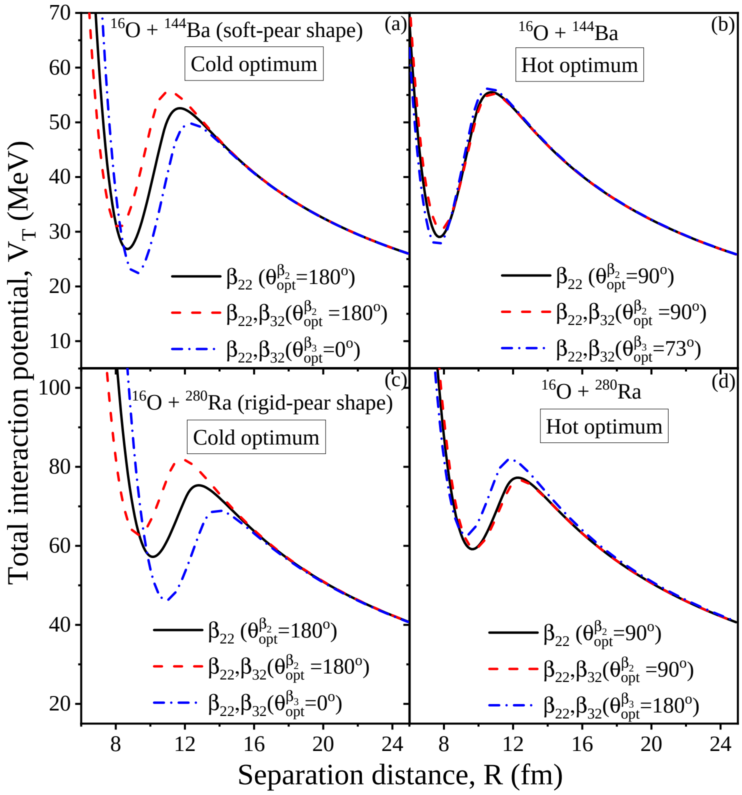

Figure 6.3: The total interaction potential V_T (MeV) as a function of separation distance R (fm) is shown for the cold and hot fusion configurations respectively in panels (a) and (b) for ^{16}O+^{144}Ba (β_{22} = 0.163, β_{32} = -0.124), and in (c) and (d) for ^{16}O+^{280}Ra (β_{22} = 0.069, β_{32} = -0.163) reaction. $\theta_{opt}^{\beta_2}$ and $\theta_{opt}^{\beta_3}$ represent the optimum angles, respectively, for deformations β_2 and up to β_3.

and 272-291. We have considered these pear shapes from their respective regions[1] in further calculations.

Initially, for an illustration, we have plotted the total interaction potential V_T (MeV) as a function of separation distance R (fm) in Fig. 6.3 for ^{16}O+^{144}Ba (soft-pear shape; $|\beta_2| > |\beta_3|$) and ^{280}Ra (rigid-pear shape; $|\beta_2| \leq |\beta_3|$) reactions. For the synthesis of a compound nucleus via cold or hot fusion process, the orientation of a deformed nucleus is fixed or optimized in two ways: (i) the noncompact (or elongated) configuration, which occurs owing to the lowest barrier height and largest interaction distance between the centers of two nuclei and (ii) the most-compact configuration occurs at the highest barrier and shortest interaction distance. The steps (i) and (ii) correspond to the 'optimum cold' and 'optimum hot' fusion configurations, respectively. By considering β_2 in the targets of the above reactions, the cold optimum orientation occurs either at $\theta_{opt}^{\beta_2} = 0^o$ or 180^o. However, by including deformation up

[1]Note that, the calculations done in the present work are for $\beta_2^+\beta_3^-$ shape of octupole deformed nucleus. Since the Nuclear Data Table of ground state deformations for nuclei of different mass-region has the negative value of β_3. The results anticipated for $\beta_2^+\beta_3^+$ are same as that obtained for $\beta_2^+\beta_3^-$, in the coplanar case.

to β_3, the noncompact or cold fusion configuration does not occur at $\theta_{opt}^{\beta_2} = 180^o$, but at $\theta_{opt}^{\beta_3} = 0^o$. Because the pear-shape octupole deformed nucleus does not have the same configuration at angles 0^o and 180^o (see Fig. 6.1). For the hot optimum case, the corresponding θ_{opt} for β_2 comes at 90^o. However, the above situation is justified at angles $\theta_{opt}^{\beta_3}$ =75$\pm$2^o and 180^o due to small β_3 in soft-pear shapes and strong contribution of β_3 in rigid-pear shapes, respectively, for more details see Ref. [1]. The above analysis can also be observed from panels (a)-(d) of Fig. 6.3 and it illustrates that, the change in $\theta_{opt}^{\beta_2}$ due to inclusion of β_3 shows significant influence on fusion barrier characteristics (barrier position R_B and barrier height V_B) as well. For the soft-pear shapes, the remarkable effects can be seen on V_B and R_B mainly for the noncompact fusion configuration, as shown in panels (a) and (b) of Fig. 6.3. On the other hand, by considering rigid-pear shape, a significant impact has been observed on fusion barrier for both the compact as well as noncompact fusion configurations, see panels (c) and (d) of Fig. 6.3. For further calculations, the above analysis is exercised for around 200 pear shapes of octupole deformed nuclei, which are belonging to different mass-regions of Periodic Table.

6.2.1 Impact of deformations up to octupole (β_3) on fusion barrier at cold and hot optimum orientations

The soft-pear shapes belonging to regions Z = 53-60 and 76-88 have different values of β_2 and β_3, and are considered as target of ^{16}O-induced reactions. Further, to observe the impact of above said pear-shape on the fusion barrier at both the hot and cold optimum orientations, we have observed the change in barrier height V_B and barrier position R_B due to inclusion of deformations up to β_3 from that of β_2. Figure 6.4 shows the variation of $V_B(\beta_2) - V_B(\beta_2, \beta_3)$ and $R_B(\beta_2) - R_B(\beta_2, \beta_3)$ for the cold optimum case, respectively in panels (a) and (b), with respect to the difference in magnitude of β_2 and β_3 deformations. The soft-pear shapes have larger magnitude of β_2 than β_3, that is why, the difference $|\beta_2| - |\beta_3|$ is greater than zero. In Fig. 6.4(a), the positive values obtained from $V_B(\beta_2)$-$V_B(\beta_2, \beta_3)$ illustrates the extent with which $V_B(\beta_2, \beta_3)$ gets lowered from $V_B(\beta_2)$. For the soft-pear shapes of mass-regions A = 103-115 (open square) and 140-150 (open circle) belonging to Z = 53-60, the difference goes up to 3.5 MeV, as the magnitude of β_3 becomes comparable to β_2 (i.e. $|\beta_2| - |\beta_3| \rightarrow 0$). On

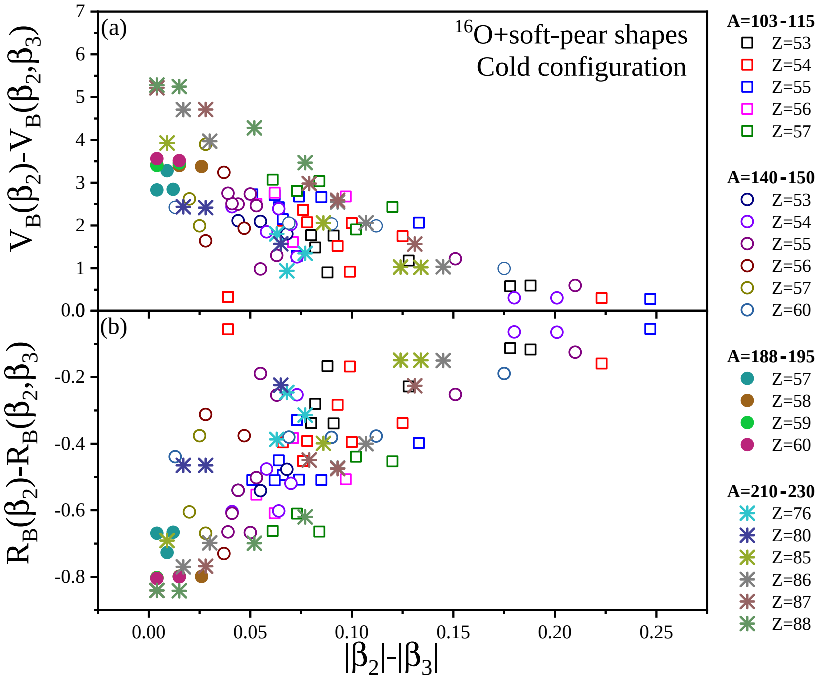

Figure 6.4: The difference in barrier height V_B and barrier position R_B obtained due to deformations up to β_2 and β_3, i.e. (a) $V_B(\beta_2)-V_B(\beta_2,\beta_3)$ and (b) $R_B(\beta_2)-R_B(\beta_2,\beta_3)$, shown with respect to the difference in the magnitude of β_2 and β_3. Note that, the above analysis is done for 'cold or noncompact' fusion configuration of ^{16}O+soft-pear shapes combinations.

the other hand, for heavy-mass regions A = 188-195 (solid circle) and 210-230 (stars) of Z = 76-88, the difference $V_B(\beta_2) - V_B(\beta_2, \beta_3)$ reaches 5.5 MeV for $|\beta_2| - |\beta_3| \to 0$. In the lower panel of Fig. 6.4, the difference of $R_B(\beta_2)$ and $R_B(\beta_2, \beta_3)$ is depicted for the above said fusion configuration and mass-regions. The negative value obtained from $R_B(\beta_2) - R_B(\beta_2, \beta_3)$ states that, the inclusion of β_3 enlarges the interaction distance between the centers of two colliding nuclei, in reference to that of β_2. A large negative value up to 0.8 fm can be seen for $R_B(\beta_2) - R_B(\beta_2, \beta_3)$, as one goes from lighter to the heavier mass systems. From above discussion, it can be clearly said for the cold optimum orientation of heavy-mass soft-pear shapes that, there is significant impact on fusion barrier height V_B and barrier position R_B, particularly when $|\beta_3|$ approaches the $|\beta_2|$-value.

Further, in Fig. 6.5, the negative and positive values obtained respectively for $V_B(\beta_2) - V_B(\beta_2, \beta_3)$ and $R_B(\beta_2) - R_B(\beta_2, \beta_3)$ represent the case of hot optimum orientation of soft-pear shapes. In Fig. 6.5(a), for mass-regions A = 103-115 and 140-150 belonging to Z = 53-60, the change of $V_B(\beta_2, \beta_3)$ from $V_B(\beta_2)$ goes up to 0.75 MeV, as $|\beta_2| - |\beta_3|$ approaches to zero. On the other hand, for A = 188-195 and 210-230, $V_B(\beta_2) - V_B(\beta_2, \beta_3)$ gives a value of about 1.5 MeV. For the case of barrier position, the positive value of $R_B(\beta_2) - R_B(\beta_2, \beta_3)$

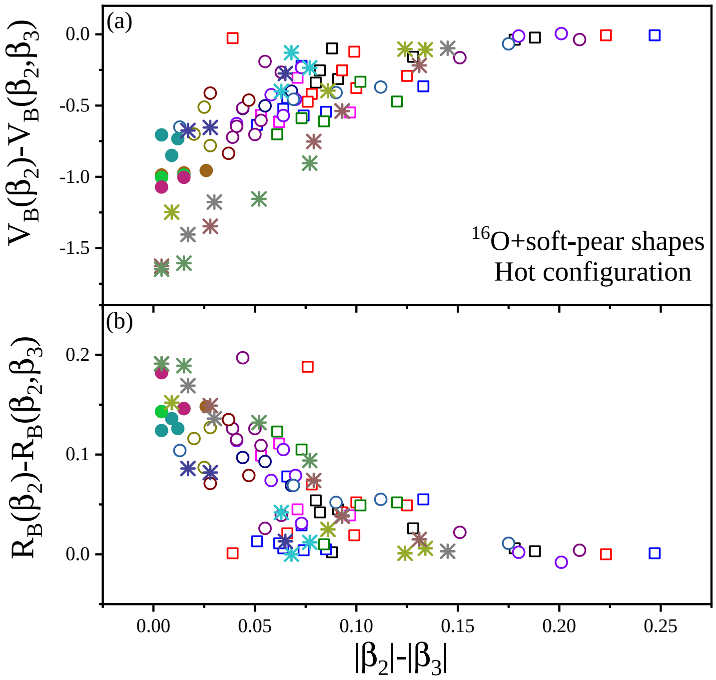

Figure 6.5: Same as Fig.6.4, but for 'hot or compact' fusion configuration.

reaches up to 0.2 fm for the heavy mass systems, which is relatively higher than that of lighter-mass soft-pear nuclei, as shown in Fig. 6.5(b). In the other words, it can be said for the hot or compact configuration that, the interaction distance becomes smaller with the inclusion of deformations up to β_3 than that of β_2, which in turn, increases $V_B(\beta_2, \beta_3)$ from $V_B(\beta_2)$. The results obtained for both the cold and hot fusion configurations of ^{16}O+soft-pear shape combinations in Figs. 6.4 and 6.5 express that, the octupole deformation of soft-pear shape shows significant impact on V_B and R_B mainly for the cold fusion configuration.

Further, we have considered the rigid-pear shapes of octupole deformed nucleus (with stronger value of β_3 than β_2) as target in ^{16}O-induced reactions to observe their corresponding effects on the fusion barrier, in reference to the results obtained for β_2 deformation. The considered choices of rigid-pear shapes belong to mass-regions A = 124-131, 189-196, 215-225 and 272-291 of Z = 37-40, 59-68 and >80, for reference one can see Fig. 6.2. Further, the variation of differences $V_B(\beta_2) - V_B(\beta_2, \beta_3)$ and $R_B(\beta_2) - R_B(\beta_2, \beta_3)$ is shown with respect to $|\beta_2| - |\beta_3|$ for the cold fusion configuration of ^{16}O+rigid-pear shape combination, respectively, in panels (a) and (b) of Fig. 6.6. In rigid-pear shapes, the magnitude of β_3 is greater or equal to that of β_2, so that, the difference $|\beta_2| - |\beta_3|$ is less than zero. For mass-regions A = 124-131 (open square) and 189-196 (open circle) of Z = 37-40 and 59-68,

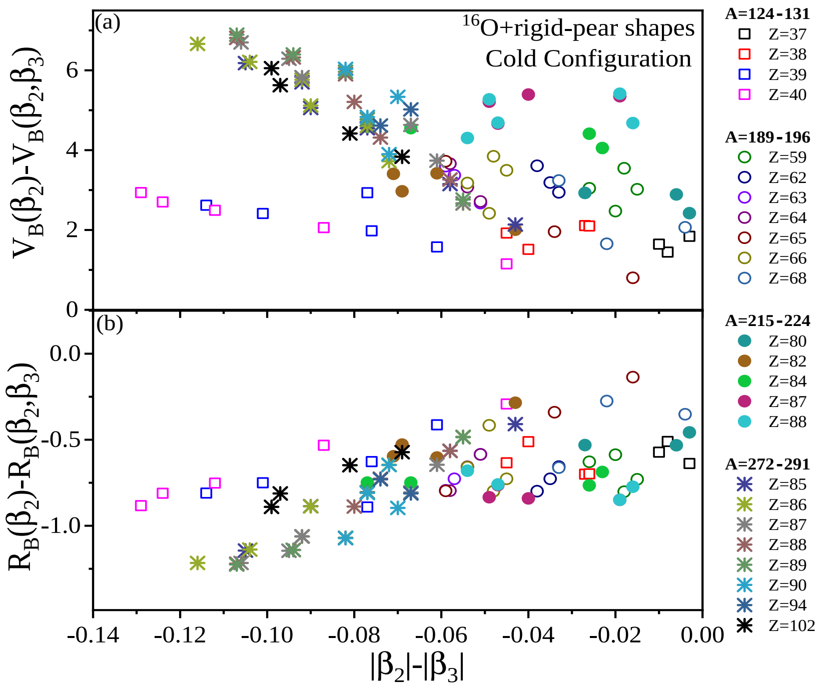

Figure 6.6: Same as Fig.6.4, but for ^{16}O+rigid-pear shapes combinations.

respectively, the positive value of $V_B(\beta_2) - V_B(\beta_2, \beta_3)$ goes up to 4 MeV, irrespective of the choice of $|\beta_2| - |\beta_3|$. On the other hand, for heavy-mass region A = 215-224 (solid circle) and 272-291 (stars) respectively of Z = 80-88 and 85-102, $V_B(\beta_2) - V_B(\beta_2, \beta_3)$ reaches up to 7 MeV, see Fig. 6.6(a). In the case of barrier position, the negative value of difference $R_B(\beta_2) - R_B(\beta_2, \beta_3)$ for the cold optimum case reaches near to 1.5 fm, as one goes from lighter to heavy-mass regions, as shown in Fig. 6.6(b).

For the case of hot or compact fusion configuration, the rigid-pear shapes show a change in $V_B(\beta_2, \beta_3)$ of about 2 MeV from $V_B(\beta_2)$ for the lighter mass-region. For heavy-mass regions, the difference $V_B(\beta_2) - V_B(\beta_2, \beta_3)$ goes up to 6.5 MeV, as shown in Fig. 6.7(a). In the case of barrier position, the negative value of difference $R_B(\beta_2) - R_B(\beta_2, \beta_3)$ reaches near to 0.8 fm with the increase in mass of rigid-pear shape. The results obtained from Figs. 6.4-6.7 for ^{16}O+deformed reactions signify that, irrespective of the choice of $|\beta_2| - |\beta_3|$, the rigid-pear shapes in which $|\beta_3| \geq |\beta_2|$ show relatively stronger influence on fusion barrier for both hot and cold optimum cases, in comparison to that of soft-pear shapes. The above analysis has also been repeated for ^{48}Ca+deformed pairs of colliding nuclei, which involve octupole deformed nucleus of soft- and rigid-pear shapes as target. As a consequence, we have observed almost similar results as that of ^{16}O-induced reactions for both the compact and noncompact fusion configurations.

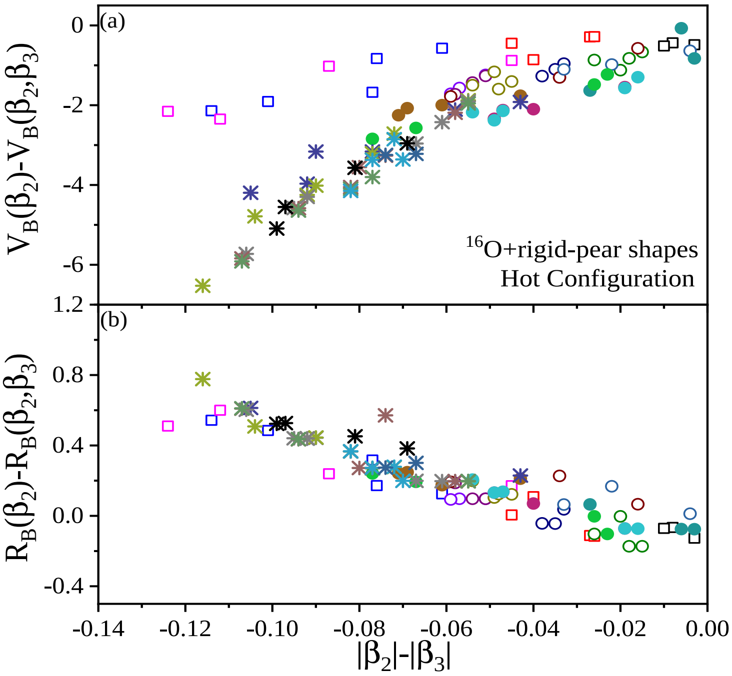

Figure 6.7: Same as Fig. 6.4, but for hot fusion configuration of ^{16}O+rigid-pear shapes combinations.

In addition to the above, we have also depicted the variation of $V_B(\beta_2) - V_B(\beta_2, \beta_3)$ and $R_B(\beta_2) - R_B(\beta_2, \beta_3)$ with respect to the difference in the quadrupole moment, Q_{20}, as a function of (β_2, β_3) and β_2 only, i.e. $Q_{20}(\beta_2, \beta_3) - Q_{20}(\beta_2)$. Here, the term Q_{20} defines the deviation from the spherical balance of the nuclear charge distribution and depends on the deformation parameters β_λ [16, 17]. The above analysis is illustrated for the cold and hot fusion configurations of ^{16}O+soft-pear shapes combinations, as shown in Fig. 6.8. From this figure, it has been observed that, the involvement of higher-order deformation (up to β_3) in quadrupole moment shows a significant variation, with the increase in the magnitude of β_3-deformation, in the barrier height V_B and corresponding barrier position R_B mainly for the cold optimum case. As a consequence, the modification observed in V_B and R_B would influence the fusion cross-sections and give the possibility of production of new heavy/superheavy elements.

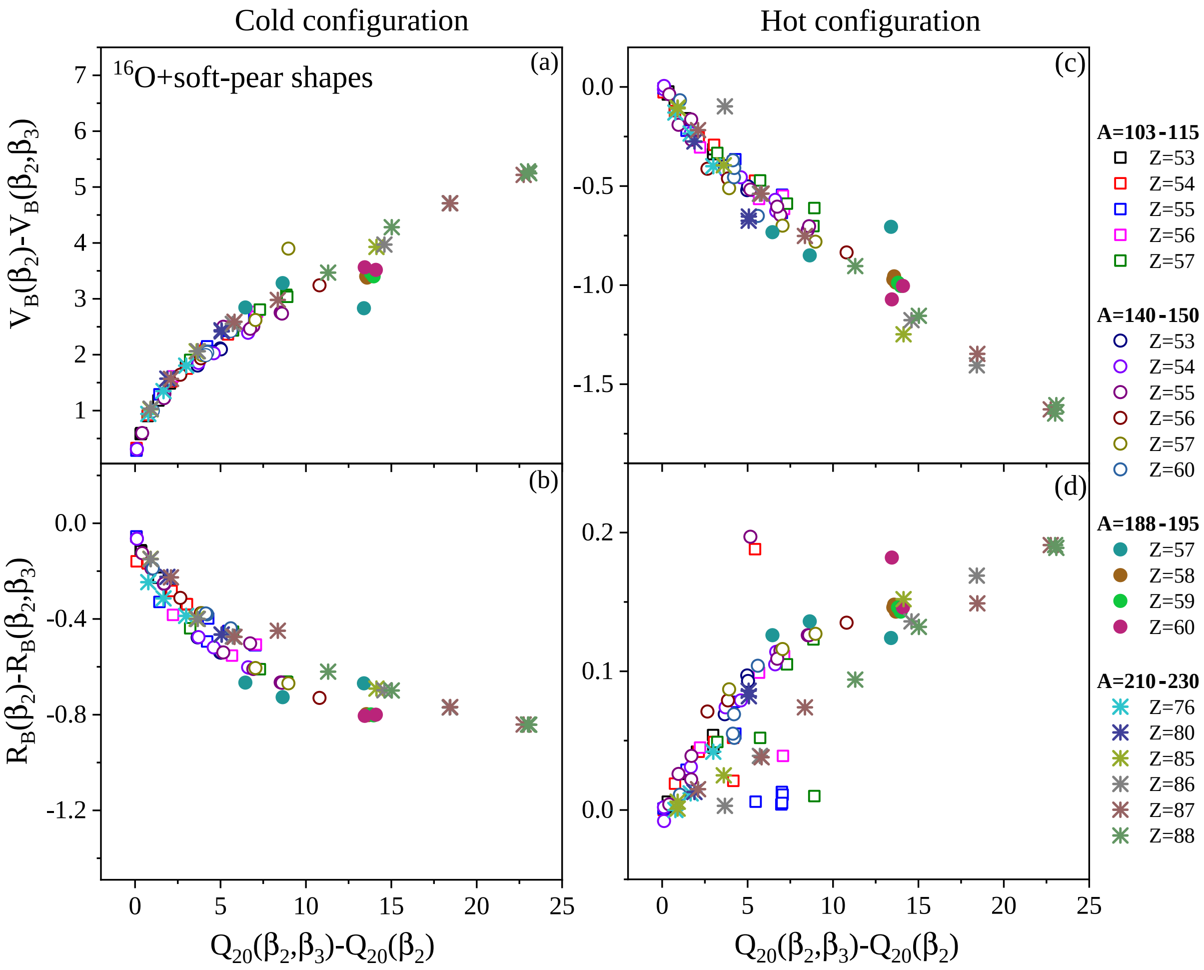

Figure 6.8: The left and right panels are same as Figs. 6.4 and 6.5, respectively, but are shown with the variation in quadrupole moment $Q_{20}(\beta_2, \beta_3)$ with the inclusion of deformations up to β_3 and $Q_{20}(\beta_2)$ due to involvement of β_2-deformation only.

6.2.2 Impression of the octupole deformed target in ^{16}O- and ^{48}Ca-induced fusion reaction cross-sections

So far, the role of octupole deformation (β_3) is analyzed on the fusion barrier characteristics by employing the cold and hot optimum orientations. This analysis tested for ^{16}O, ^{48}Ca+soft- and rigid-pear shape reactions is compared with the results obtained for quadrupole (β_2) deformations. In addition to the above, we have calculated the fusion cross-sections to address the exclusive role of β_3-deformations. For the calculation of fusion cross-section which is function of center of mass energy $E_{c.m.}$ and barrier characteristics (barrier height V_B, barrier position R_B and barrier curvature $\hbar\omega_B$), we have used the Wong formula [18]. As we know, the fusion barrier parameters are sensitive towards the deforma-

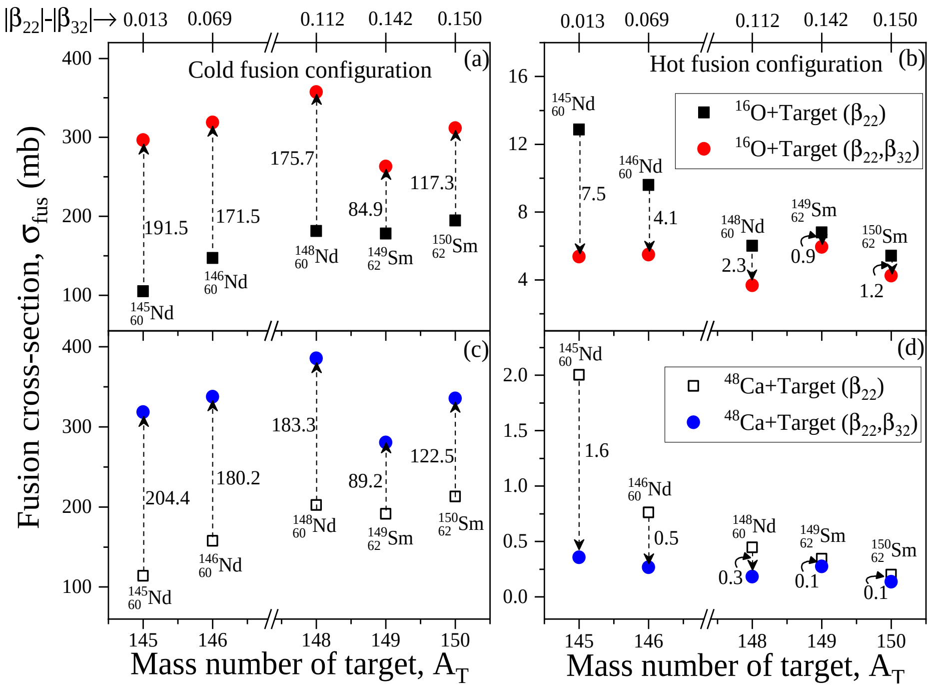

Figure 6.9: The fusion cross-sections calculated using Wong formula [18] for (a), (c) cold and (b), (d) hot fusion configurations of ^{16}O, ^{48}Ca+soft-pear shapes (^{145,146,148}Nd and ^{149,150}Sm) reactions, at $E_{c.m.} = V_B$.

tion and orientation degrees of freedom. So, the fusion cross-sections (σ_{fus}) are illustrated as a collective effect of barrier characteristics for spherical-plus-octupole deformed pairs of colliding nuclei. In view of this, we have plotted σ_{fus} (mb) at $E_{c.m.} = V_B$ for the above mentioned fusion configurations of ^{16}O, ^{48}Ca+octupole deformed nucleus reactions.

In Fig. 6.4, with the consideration of soft-pear shapes as target in ^{16}O- and ^{48}Ca-induced reactions, we find relatively higher impact on the fusion barrier as the magnitude of β_3 becomes comparable to β_2 or $|\beta_2| - |\beta_3| \to 0$. Thus, in the calculation of σ_{fus}, we have considered octupole deformed nuclei ^{145,146,148}Nd and ^{149,150}Sm, which are stable in nature [19] and can also be used for future fusion experiments. For the cold or noncompact fusion configuration shown in panels (a) and (c) of Fig. 6.9, it has been observed that, there is enhancement in σ_{fus} due to β_3 from that of β_2. The change in $\sigma_{fus}(\beta_2, \beta_3)$ from $\sigma_{fus}(\beta_2)$ is relatively higher for the octupole deformed targets (^{145,146,148}Nd), which have small difference in the magnitude of β_2 and β_3-deformations, i.e. $|\beta_{22}| - |\beta_{32}| \leq 0.112$. This analysis holds true for both the ^{16}O- and ^{48}Ca-induced reactions, as shown in panels (a) and (c) of Fig. 6.9. On the other hand, in the case of compact or hot fusion configuration of soft-pear shapes, the change observed on fusion barrier is relatively less. As a consequence, the fusion cross-sections obtained due to weak β_3 of soft-pear shape differ by smaller amount when compared

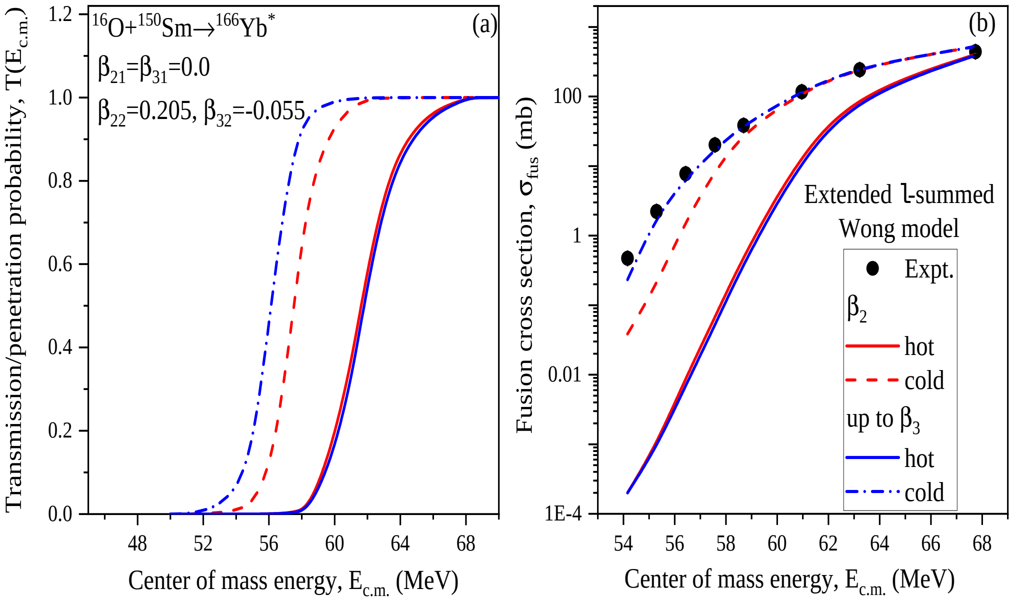

Figure 6.10: (a) The transmission probability $T(E_{c.m.})$ calculated as a function of center of mass energy $E_{c.m.}$(MeV), and (b) fusion cross-sections obtained using the extended ℓ-summed Wong model [20] for ^{16}O+^{150}Sm ($\beta_{22} = 0.205$, $\beta_{32} = -0.055$) reaction [2] at both the hot and cold optimum orientations [1] related to quadrupole and octupole deformations, across the Coulomb barrier energies.

with β_2-case, as shown in panels (b) and (d) of Fig. 6.9. Further, the nuclei ^{147}Eu and ^{223}Ra of rigid-pear shapes with sufficient half-life [19] are considered as target of ^{16}O, ^{48}Ca-induced reactions and studied their corresponding effects on fusion cross-sections. As observed in earlier section, the rigid-pear shapes show relatively higher impact on fusion barrier for both the cold and hot fusion configurations, in comparison to the soft-pear shapes. Consequently, the corresponding impact is observed on the fusion cross-sections as well. The maximum change observed in $\sigma_{fus}(\beta_2, \beta_3)$ from $\sigma_{fus}(\beta_2)$ for the cold and hot fusion configurations is about 400 mb and 15 mb, respectively, which is larger than that of soft-pear shapes. In the future experiments, it would be of interest to use the octupole deformed nuclei (soft- and rigid-pear shapes) in nuclear fusion reactions, for the formation of new nuclei/isotopes.

In [2], the experimentally determined fusion cross-sections are given across the Coulomb barrier energy for ^{16}O+^{150}Sm ($\beta_{22} = 0.205$, $\beta_{32} = -0.055$) reaction, which has octupole deformed target of soft-pear shape. In view of this, we have calculated the fusion cross-sections with the inclusion of higher-order deformation (up to β_3) and compared the results with the experimental one. In the above discussion, the Wong formula is used for the calculation of fusion cross-sections at $E_{c.m.} = V_B$. Since, Wong had taken ℓ-summation under some approximations and given the formula for $\ell = 0$ case. Further, the ℓ-summation is carried out explicitly in [20], which is named as the extended ℓ-summed Wong model. The fusion cross-section determined using this extended version of Wong formula is expressed in terms of quantum-mechanical transmission probability $T(E_{c.m.})$, see Eq.(12) of Ref. [14]. At first, we have analyzed the variation of $T(E_{c.m.})$ with respect to $E_{c.m.}$ for the above mentioned reaction. In Fig. 6.10(a), one can see the behavior of $T(E_{c.m.})$ across the Coulomb barrier energies for hot as well as cold fusion configurations of above mentioned reaction. Across the Coulomb barrier energies, there is relatively larger possibility of penetration due to inclusion of deformations up to β_3. On the other hand, for hot or compact fusion configuration of spherical-deformed combination, there is very nominal value observed for $T(E_{c.m.})$, especially at below and near barrier energies. The above observation is further analyzed in terms of fusion cross-sections (σ_{fus}) using extended ℓ-summed Wong model. The calculation of σ_{fus} done with the inclusion of β_2 and up to β_3-defomrations for both the hot and cold configurations are compared with the available data, as shown in Fig. 6.10(b). In Fig. 6.10, we can see that, the target ^{150}Sm is a soft-pear shape of octupole nucleus, so the results obtained for the hot fusion configuration either with the involvement of β_2 or up to β_3 are almost similar and show hindrance from the data. On the other hand, the σ_{fus} obtained at cold optimum orientation of β_3 shows better results in comparison to that of quadrupole deformation. In other words, the fusion cross-sections calculated for cold or noncompact fusion configuration of octupole deformed target (^{150}Sm) reproduce the experimental data nicely across the Coulomb barrier energies.

Also, we have explored the average effect of β_3 deformation in terms of σ_{fus} for ^{16}O+^{150}Sm reaction, by integrating σ_{fus} over the orientations θ_2, as shown in Fig.6.11. It shows relatively better comparison with the data, as compared to that for β_2-case, see Fig.6.11(a). However, we notice fusion hindrance even after inclusion of β_3-deformation. In this case, an extra energy is required to make such systems to fuse and is called as extra-push energy. In view of this, many authors have implemented this idea and analyzed the the influence of different factors (likewise channel-coupling effects, dynamical deformations, phenomenological model, etc.), which in turn, give extra-push energy at the below barrier region to address the fusion hindrance [21–26]. In our work, the main aim is to find the exclusive role of the optimum orientations (θ_{opt}) related to the static deformations of octupole (β_3) deformed nuclei on the barrier characteristics and subsequently on the fusion cross-sections, in reference to the results obtained with the inclusion of static quadrupole (β_2) deformations and related

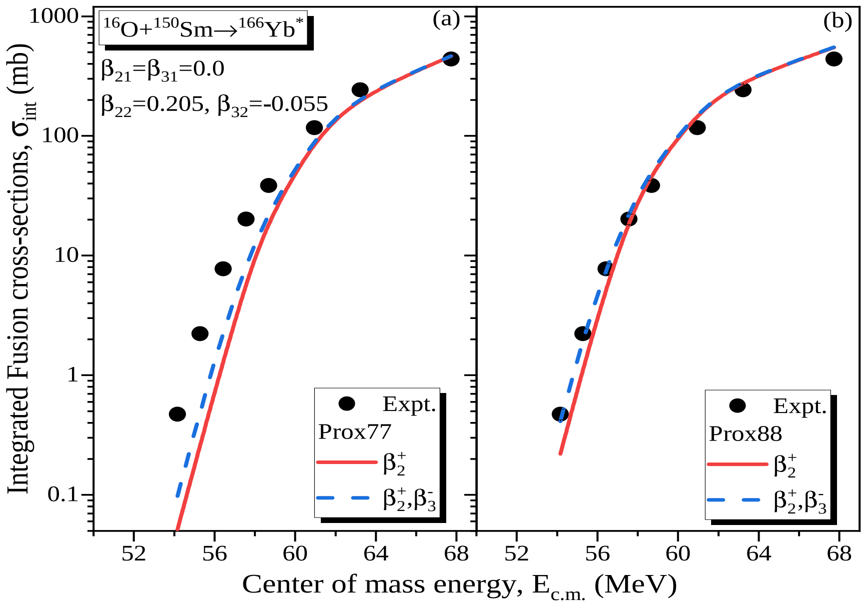

Figure 6.11: The fusion cross-sections integrated (σ_{int}) over orientations θ_2 calculated using (a) Prox77 and (b) Prox88 for ^{16}O+^{150}Sm ($\beta_{22} = 0.205, \beta_{32} = -0.055$) reaction is varied as a function of the center of mass energy $E_{c.m.}$(MeV).

θ_{opt}. In this context, the fusion hindrance is addressed by employing a modified version of Prox77, i.e. Prox88 [27]. Due to different values of coefficient γ_0 and k_s=1.2496 MeV fm^{-2} and 2.3, respectively, used in Prox88, the barrier height V_B decreases and barrier position R_B increases from that of Prox77. Consequently, the integrated fusion cross-sections obtained due to the inclusion of deformations up to β_3 within Prox88 potential give a better fit to the experimental data of ^{16}O+^{150}Sm reaction, see in Fig. 6.11(b), as compared to the β_2-case. It is to be noted here that, the fusion cross-sections shown in Figs. 6.10 and 6.11 represent the case for soft-pear target of ^{16}O-induced reaction, since its experimental data is available. The exclusive role of octupole deformation for rigid-pear shape will be more prominent in reference to β_2-case. However, we have not shown this kind of comparison for rigid-pear nuclei, due to unavailability of experimental data.

6.3 Conclusion

For the synthesis of a compound nucleus either via cold or hot fusion processes, the information on the fusion barrier characteristics (V_B and R_B) is required and extracted from the total interaction potential, which depends on the deformation and orientation degrees of freedom.

The octupole deformation, which distorts the spherical-symmetric quadrupole deformed nucleus into symmetry-breaking pear shape, give different values of optimum orientations (θ_{opt}) for the 'compact or hot' and 'elongated or cold' fusion configurations, in reference to θ_{opt} obtained for β_2. In view of this, this Chapter has shown the influence of higher order deformations up to β_3 and related θ_{opt} on fusion barrier parameters. It has been observed that, the elongated configuration of octupole deformed nucleus shows significant impact on the fusion barrier, in comparison to the most compact case. Similar results have been observed in the estimation of fusion cross-sections (σ_{fus}) for ^{16}O, ^{48}Ca+octupole deformed nuclei (soft-pear shapes $\rightarrow^{145,146,148}$Nd, ^{149,150}Sm, and rigid-pear shapes $\rightarrow^{147}$Eu, ^{223}Ra). Also, the calculation of σ_{fus} with the inclusion of deformations up to β_3 at cold optimum orientation reproduces the experimental data across the Coulomb barrier for ^{16}O+^{150}Sm ($\beta_{22} = 0.205$, $\beta_{32} = -0.055$) reaction using extended ℓ-summed Wong model. In addition to this, we have integrated the fusion cross-sections (σ_{int}) over all orientation, firstly by including β_2 and then β_3-deformation of deformed target of the above mentioned reaction. Even though the inclusion of deformations up to β_3 enhances σ_{int} from that of β_2, we have noticed fusion hindrance at the below-barrier region, where extra-push energy is required to make such systems to fuse. In view of this, a modified version of Prox77, i.e. Prox88, of relatively lower barrier height and larger barrier position is employed. As a consequence, the involvement of β_3-deformation within Prox88 potential gives a better agreement with the experimental data of ^{16}O+^{150}Sm reaction. Thus the nuclear potentials like Prox88, which gives lower barrier height, provide extra-push at below Coulomb barrier energies for accounting the fusion hindrance.

We conclude that, the consideration of octupole deformed nuclei in fusion reactions can be used for the synthesis of new isotopes of heavy/super-heavy nuclei. The β_3-induced optimum orientations play important role to address the behavior of barrier characteristics and associated fusion cross-sections. On the basis of above observation, the influence of deformations up to β_3 would be discussed in the disintegration process of a compound nuclear entity.

Bibliography

[1] S. Jain, M. K. Sharma and R. Kumar, Phys. Rev. C **101**, 051601(R) (2020).

[2] R. G. Stokstad *et al*, Phys. Rev. C **21**, 2427 (1980).

[3] K. Morita *et al*, J. Phys. Soc. Japan **73**, 2593 (2004).

[4] Yu. Ts. Oganessian *et al*, Phys. Rev. C **70**, 064609 (2004).

[5] Yu. Ts. Oganessian *et al*, Phys. Rev. C **74**, 044602 (2006).

[6] K. Morita *et al*, J. Phys. Soc. Japan **76**, 043201 (2007).

[7] A. Sandulescu *et al*, Phys. Lett. B **60**, 225 (1976).

[8] R. K. Gupta, A. Sandulescu and W. Greiner, Phys. Lett. B **67**, 257 (1977).

[9] R. K. Gupta, C. Parvulescu, A. Sandulescu and W. Greiner, Z. Phys. A **283**, 217 (1977).

[10] R. K. Gupta, A. Sandulescu and W. Greiner, Z. *Natureforsch.* **32a**, 704 (1977).

[11] R. K. Gupta *et al*, J. Phys. G: Nucl. Part. Phys. **31**, 631-644 (2005).

[12] N. Wang *et al*, Phys. Rev. C **74**, 044604 (2006).

[13] M. Ismail and W. M. Seif, Phys. Rev. C **81**, 034607 (2010).

[14] S. Jain, M. K. Sharma and R. Kumar, Chin. Phys. C Vol. **46**, No. 1, 014102 (2022).

[15] P. Moller *et al*, At. Data and Nucl. Data Tables **109-110**, 1-204 (2016).

[16] G. A. Leander and Y. S. Chen, Phys. Rev. C **37**, 2744 (1988).

[17] P. A. Butler, J. Phys. G: Nucl. Part. Phys. **43**, 073002 (2016).

[18] C. Y. Wong, Phys. Rev. Lett. **31**, 766 (1973).

[19] International Atomic Energy Agency, Nuclear Data Services, https://www-nds.iaea.org/.

[20] R. Kumar *et al*, Phys. Rev. C **80**, 034618 (2009).

[21] W. J. Swiatecki, Nucl. Phys. A **376**, 275-291 (1982).

[22] H. Gaggeler *et al*, Z. Phys. A – Atoms and Nuclei **361**, 291-307 (1984).

[23] M. Dasgupta *et al*, Annu. Rev. Nucl. Part. Sci. **48**, 401-61 (1998).

[24] C. Simenel, Eur. Phys. J. A **48**, 152 (2012).

[25] K. Sekizawa and K. Yabana, Phys. Rev. C **88**, 014614 (2013).

[26] K. Washiyama, Phys. Rev. C **91**, 064607 (2015).

[27] W. Reisdrof, J. Phys. G: Nucl. Part. Phys. **20**, 1297 (1994).

Chapter 7

Decay dynamics of ^{222,224,226,228,230}Th* compound nuclei using quadrupole and octupole deformations

7.1 Introduction

A comprehensive knowledge is required to understand the complex behavior of the nuclear fragments emitted in variety of decay channels of compound nucleus formed in heavy-ion induced reactions. Such decaying fragments behave as a source of production of new isotopes/elements away from the beta-stability line, which in turn, help to extend the Periodic Table. The newly discovered nuclei are further harvested for the fundamental understanding related to various nuclear properties and the associated applications in diverse areas such as radiation, astro sciences, medical and health sector, etc.

In general, the possible target-projectile combination forms an excited compound nucleus (CN), and subsequently disintegrates into the binary fragments under various conditions, such as excitation energy/temperature, angular momentum, deformations, orientations etc. With the effect of these factors, the de-excitation of the CN may lead to different decay mechanisms, viz., evaporation residues (ERs) or equivalently light-mass fragments (LFs), intermediate-mass fragment (IMF), heavy-mass fragment (HMF) and fission fragments. The dominance of these decay modes varies with the mass and excitation energy of CN. In the present chapter, we will focus on the study of fission process, which is dominant in the heavy-mass region.

The de-excitation of compound nucleus, formed via ^{208}Pb-based (cold fusion process) or ^{48}Ca-induced reactions (hot fusion process), respectively, at the low ($E^*_{CN} \approx$ 10-20 MeV) [1,2] and high excitation energies ($E^*_{CN} \approx$ 35-45 MeV) [3, 4] may lead to the production of new elements. The low and high ranges of E^*_{CN} correspond to the incident energy $E_{c.m.}$, which may spread across the Coulomb barrier [5,6]. In the work of Gupta and his collaborators [7], the fragmentation of excited CN has been discussed by considering quadrupole (β_2) deformations along with the cold and hot optimum orientation effects. In our recent work [8], it has been analyzed that, the octupole deformed nuclei of pear shapes which break symmetry along the reflection axis modifies the value of θ_{opt}, from the ones obtained for β_2-deformed case. Later, in [9] and Chapter 6, it has been realized that, this new set of optimum orientations related to the elongated (or cold) configuration of octupole deformed nuclei shows relatively larger impact on the fusion/Coulomb barrier, as compared to the compact (or hot) configuration case. In view of this, it would be interesting to analyze the possibility of elongated octupole deformed fragment emitting from a compound nucleus, which is formed at the low excitation energies.

In the recent experimental work [10], the fission dynamics of heavy-mass actinides (e.g. ^{230}Th, ^{234,236}U, ^{240}Pu, ^{246}Cm, ^{250}Cf and ^{258}Fm) has been discussed and confirmed non-ambiguously the emission of octupole deformed nuclei/fragment at the low excitation energy. Such analysis has motivated us to study the application of cold optimum orientations of octupole deformed fragments in the fission dynamics of even-even isotopes of Thorium, i.e. $^{222-230}$Th*. This analysis is exercised at the low value of E^*_{CN}, which corresponds to the cold synthesis of element. To carry forward with this idea, we are using the Dynamical Cluster-decay Model (DCM) [11–13], which is applied to probe various decay mechanisms of CN formed in heavy-ion induced reactions. The model has been built on the collective clusterization approach of Quantum Mechanical Fragmentation Theory (QMFT) [14–16].

In the present Chapter, to have an explicit understanding of higher-order deformation (up to β_3) and related cold optimum orientations, the fission of 'Th' isotopes is discussed by a comparative analysis of fission fragment distributions using mass asymmetry (η_A) and charge asymmetry (η_Z) parameters. In the above analysis, the minima of potential observed in the fission helps in determining the peak value of preformation probability for the fission fragments. On the basis of this, the identification of the most probable fission fragments in reference to η_A and η_Z co-ordinates is also done. Note that the neck-length parameter optimized for the ^{224}Th* nucleus in reference to the available experimental data for below-barrier energies [17] has been worked out for the fragmentation analysis of the remaining isotopes of Th. In DCM, the neck-length parameter $\triangle R$, the only parameter, is utilized to fix the first turning point, where the preformed fragments start to penetrate through the interaction potential.

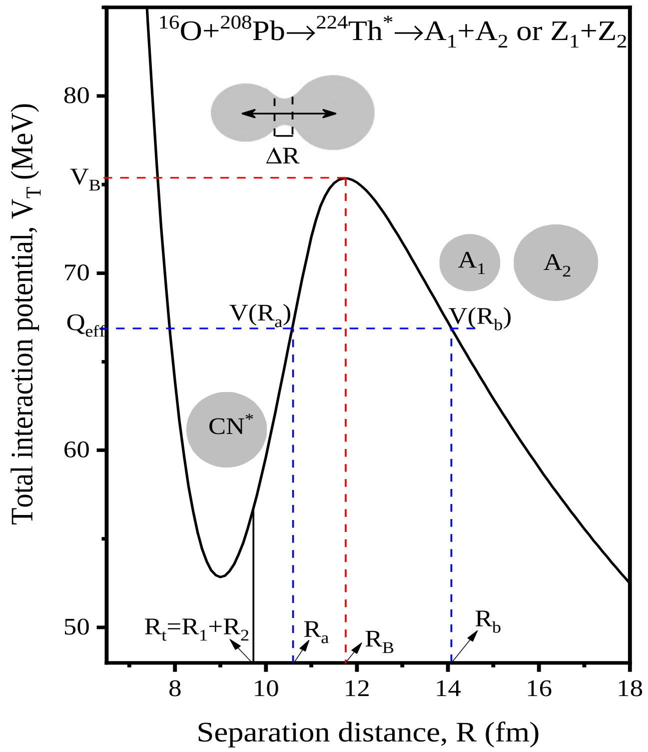

Figure 7.1: The variation of total interaction potential V_T (MeV) as a function of separation distance R (fm) between the colliding nuclear partners is shown for ^{16}O+^{208}Pb→^{224}Th* reaction. Here, $R_a = R_1(\alpha_1, T) + R_2(\alpha_2, T) + \triangle R$ defines the first turning point.

7.2 Calculations and results

In this Chapter, the main purpose is to analyze the influence of the elongated (or cold) configuration of octupole (β_3) deformed nuclei in the fission dynamics of even-even isotopes of thorium, i.e. $^{222-230}$Th*. The calculations are done at the low excitation energy E^*_{CN}, which is relevant for the cold synthesis process. To carry forward with this idea, the deformations (up to β_3) and corresponding cold optimum orientation [8] are included in the framework of the Dynamical Cluster-decay Model (DCM), which is developed on the basis of QMFT. In the notion of QMFT, the probable decaying fragments/clusters are preborn inside the excited compound nucleus (CN) and then they penetrate through the interaction potential. With the use of the neck-length parameter $\triangle R$, which is the only parameter of DCM, one can fix the first turning point of the barrier penetration.

To have the knowledge of the turning points for pre-born fragments of Th* isotopes, the neck-length parameter has to be optimized first, in view of the fission data at the low excitation energies, corresponding to the below-barrier energies. In view of this, the upcoming section discusses about the fission cross-sections calculated by including deformations (up to β_3) and cold optimum orientation effects in DCM for ^{224}Th* compound nucleus and are compared with the available experimental data [17][1]. Further, the decay analysis of ^{222,224,226,228,230}Th* nuclei is illustrated at the same neck-length $\triangle R$, obtained in fitting the data for ^{16}O+^{208}Pb reaction forming ^{224}Th* compound nucleus. This means the preformed cluster/fragment formed inside the potential pocket starts penetrating through the first classical turning point, i.e. $R = R_a = R_1(\alpha_1, T) + R_2(\alpha_2, T) + \triangle R$, and terminates through the second turning point R_b, such that $V(R_a) = V(R_b)$; for more clarity see Fig. 7.1, where the total interaction potential is plotted as a function of separation distance R. The idea of introducing the neck-length parameter $\triangle R$ within the DCM [18–20] is similar to the saddle- [21,22] and scission-point [23] statistical fission models. The permissible value of $\triangle R$ lies in the nuclear proximity range of about 2 fm, since the surface interaction between two fragments can take place around this range of $\triangle R$ to experience the nuclear force. Further, the above analysis is discussed in terms of the fragmentation potential ($V(\eta)$), which is minimized in reference to the mass (A_2) and charge number (Z_2) of decaying fragment. Subsequently, the preformation probability P_0 (showing the inverse trend of $V(\eta)$) as a function of mass- (η_A) and charge-asymmetry (η_Z) coordinates illustrates, respectively, the mass- and charge-dispersion cases.

7.2.1 Fission cross-sections for ^{224}Th* nucleus formed in ^{208}Pb-based reaction

The minimization of fragmentation potential can be done in reference to the mass number A_2 as well as charge number Z_2 of decaying nuclear partner from $^{224}_{90}$Th* and for convenience, can also be understood from Figs. 7.2 and 7.3, respectively. In Fig. 7.2, the mass number A_2 of fragment and its isobars of different charge number Z_2 are shown along the horizontal and vertical axes, respectively. The color-map represents the strength of fragmentation potential $V(\eta)$ for each A_2 and corresponding Z_2. The black spheres in the dark purple region show the lowest or minimum value of $V(\eta)$ for the decay fragments, which helps in choosing Z_2 for corresponding A_2 values. In other words, it is called the minimization of fragmentation

[1]Note that, for below-barrier region, the experimental measurements of fission cross-sections are available only for ^{224}Th* isotope of Thorium.

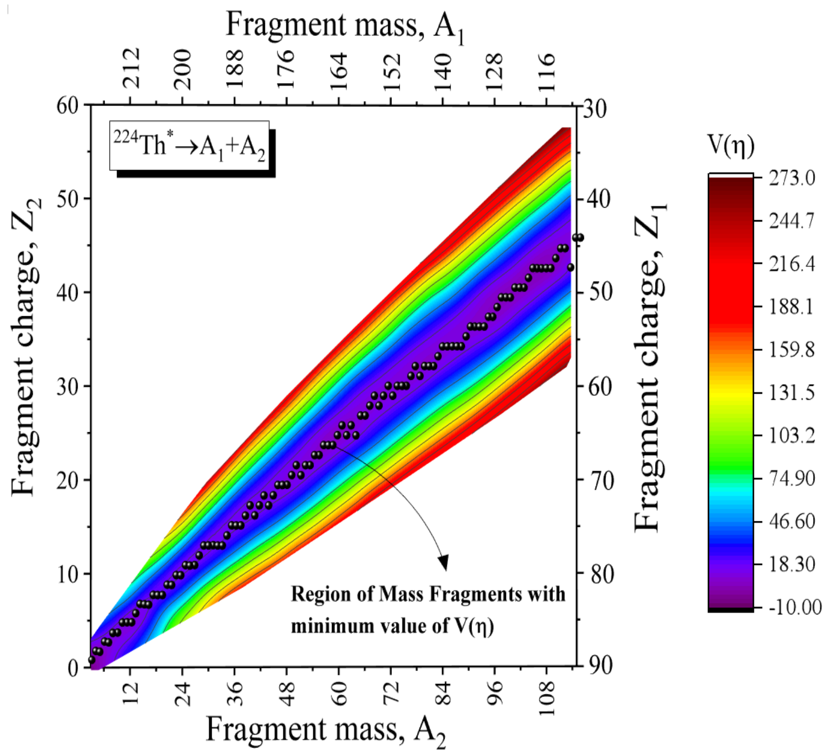

Figure 7.2: The color-map representing the fragmentation potential $V(\eta)$ for $^{224}Th^*$ with respect to the fragment mass number A_2 having isobars (of different charge number Z_2). The mass A_1 and charge number Z_1 of decaying partner are also shown in the top and right axes, respectively.

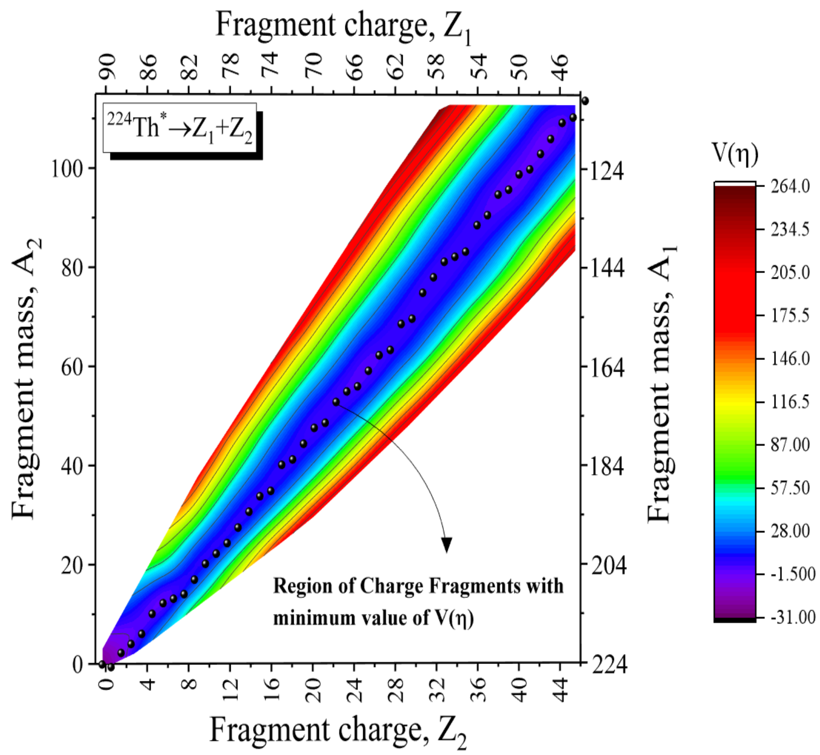

Figure 7.3: The color-map representing $V(\eta)$ for $^{224}Th^*$ with respect to the fragment charge number A_2 having isotopes (of different mass number A_2).

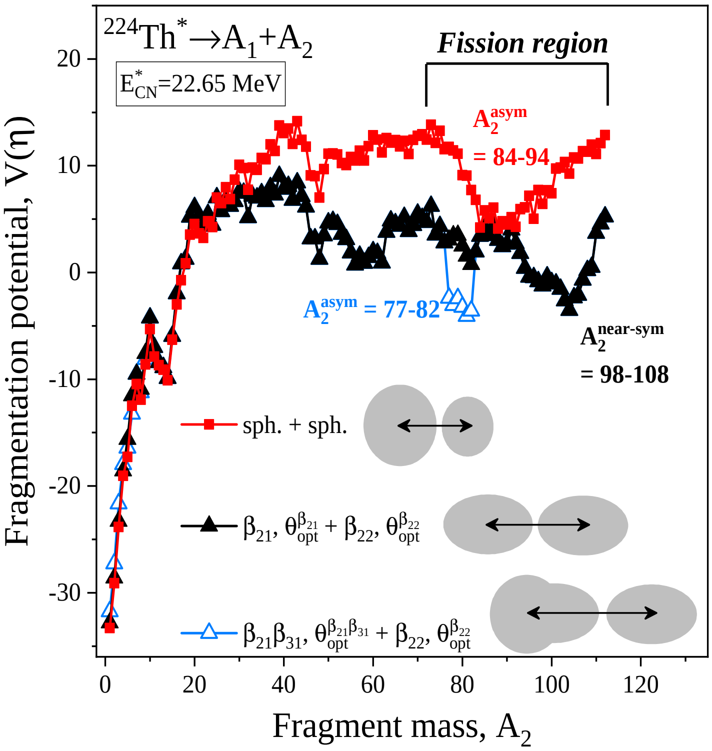

Figure 7.4: The variation of minimized fragmentation potential with respect to the mass number of decaying fragment, firstly for spherical (sph.) and then by including quadrupole (β_{2i}) and octupole (β_{3i}) deformations along with the related cold optimum orientations ($\theta_{opt}^{\beta_{\lambda=2,3}}$). Here, i = 1, 2 refer to binary fragments A_1 and A_2, respectively.

potential in reference to the mass number of CN. Further in Fig. 7.3, for each Z_2 of decay fragment, there are isotopes of different mass number A_2 and the spherical dots present in the dark blue color indicate the minima of $V(\eta)$ for an isotope. This way, one can find the minimization of $V(\eta)$ in reference to the charge number. Note that, the mass and charge numbers of other decay partner are $A_1 = A - A_2$ and $Z_1 = Z - Z_2$, respectively, as shown in the opposite axes of A_2 and Z_2 of Figs. 7.2 and 7.3.

Further, the minimized potential $V(\eta)$ obtained for the disintegration of ^{224}Th* over the fragment mass A_1=1-223 (and A_2 = 223-1) and charge number Z_1 = 0-90 (and Z_2 = 90-0) is discussed to understand the fragmentation structure with the inclusion of deformations (up to β_3) and cold optimum orientation effects. For an illustration, in Fig. 7.4, the role of quadrupole/octupole deformations and associated cold optimum orientation can be analyzed in reference to the spherical configuration of decaying fragments in the fission valley/region (marked in the figure). This region has the mass range of fission fragment A_2 from 72 to 112. It is clearly seen from this figure that, as one goes from spherical (sph.)+sph. to quadrupole

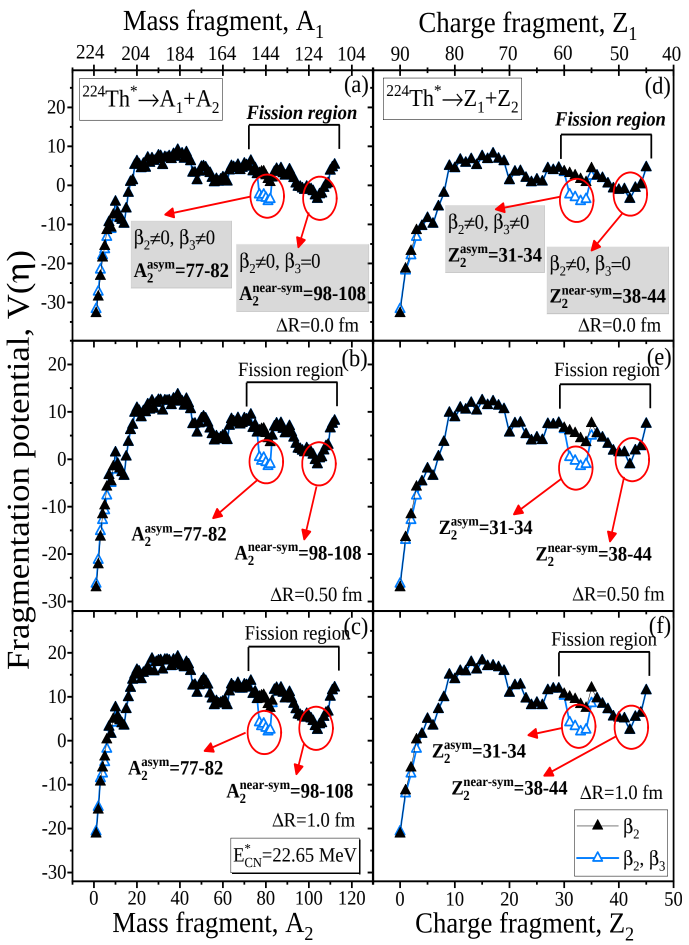

Figure 7.5: The minimized fragmentation potential in reference to the fragment (a)-(c) mass A_2 and (d)-(f) charge number Z_2 of ^{224}Th*, at low excitation energy $E^*_{CN} = 22.65$ MeV and $\ell = 0\hbar$. The analysis is exercised at different values of neck-length parameter, i.e. $\triangle R = 0.0$, 0.5 and 1.0 fm.

(quad.)+quad. and then to quad.+octupole deformed fragments, the interaction distance increases, which in turn, lowers the potential barrier with a larger extent. As a consequence, one can see that, the minimization and structure of fragmentation potential modifies with a significant effect due to incorporation of deformation and orientation degrees of freedom. In the comparative analysis of mass- and charge-dispersion cases, the behavior of $V(\eta)$ has been tested for different values of neck-length parameter $\triangle R$ (= 0.0, 0.5 and 1.0 fm), as shown in Fig. 7.5. The above analysis is exercised at the lowest value of excitation energy, i.e. $E^*_{CN} = 22.35$ MeV, which is referred from the available experimental data of fission cross-sections for ^{16}O+^{208}Pb→^{224}Th* reaction at energies 22.65-25.29 MeV [17]. Since the present work is constrained to study the fission process of above mentioned reaction, so the relevant dips are specified in Fig. 7.5 for fragmentation potential. One can clearly see the dip of $V(\eta)$ near the symmetric region ($\approx \frac{A_{CN}}{2} = 112$ and $\frac{Z_{CN}}{2} = 45$) for quadrupole (β_2) deformed nuclei associated with the cold optimum orientation. Afterwards, the presence of octupole (β_2, β_3) deformed fragments along with the optimum orientation defining its elongated configuration show the minima of $V(\eta)$ in the asymmetric region which competes with that of the near-symmetric region. Also, it is important to note that, the magnitude and structure of potential observed in both the mass and charge distributions of ^{224}Th* is almost similar. The above results obtained due to β_2, β_3-deformations and related cold optimum orientations are consistently true for different choices of $\triangle R$. In the calculation of preformation probability P_0, the mass- and charge-dispersion concepts are introduced through the mass- $\left(\eta_A = \frac{|A_1-A_2|}{A_1+A_2}\right)$ and charge-asymmetry $\left(\eta_Z = \frac{|Z_1-Z_2|}{Z_1+Z_2}\right)$ coordinates, which are treated as the dynamical factors in the collective clusterization approach of DCM. It is known that, the decaying binary fragments with the minimum value of fragmentation potential possess the highest preformation probability P_0. In other words, it can be said that, the term 'P_0' shows an inverse trend from that of $V(\eta)$ observed in Fig. 7.5. The fission fragments observed in the near-symmetric and asymmetric regions in both the mass- and charge-distribution cases are almost similar.

On the basis of above observation, we have calculated the fission cross-sections (σ_{fis}^{DCM}) using DCM for both the mass- and charge-distributions of ^{224}Th*, formed from ^{16}O+^{208}Pb reaction, at energies below the Coulomb barrier. The detail of theoretically and experimentally obtained σ_{fis} for the above mentioned reaction is given in Table 7.1. The calculations have been done initially with the inclusion of β_2-deformation and related cold optimum orientation $(\theta_{opt}^{\beta_2})$. Subsequently, the experimental data has been addressed within the permissible values of $\triangle R$, for incident beam energies $E_{c.m.}$ = 68.69 - 71.33 MeV. In the above calculations, the values of ℓ_{max} are obtained at a point when there is no contribution of light particle. Later, due to involvement of deformations (up to β_3) along with $\theta_{opt}^{\beta_2,\beta_3}$, there is an increment in ℓ_{max} about 10% and the obtained σ_{fis}^{DCM} are found closer to $\sigma_{fis}^{Expt.}$. However, there is a very small change in $\triangle R$. Apart from this, one can also notice from Table 7.1 that, the neck-length parameter reduces significantly, as one moves from the mass-distribution to the charge-distribution criteria. This means, for charge-dispersion case, the interaction among decaying fragments takes place at relatively smaller distance from that of the mass-dispersion/distribution of an excited compound nucleus.

Based on the above observations related to the neck-length parameter and ℓ_{max}-values, the fission dynamics of all considered isotopes of ^{222,224,226,228,230}Th* has been studied using DCM.

Table 7.1: The detail of calculated fission cross-sections σ_{fis}^{DCM} (mb) of ^{16}O+^{208}Pb$\rightarrow$^{224}Th* reaction with the inclusion of deformation up to β_3 and related cold optimum orientation ($\theta_{opt}^{\beta_2}$ and $\theta_{opt}^{\beta_2,\beta_3}$). For comparison, the experimental data [17] of the above mentioned reaction is also given.

E^*_{CN} (MeV)	$E_{c.m.}$ (MeV)	T (MeV)	$\sigma_{fis}^{Expt.}$ (mb)	$\triangle R$ (fm)		$\ell_{max}(\hbar)$		σ_{fis}^{DCM}(mb)	
				β_2	β_2,β_3	β_2	β_2,β_3	β_2	β_2,β_3
			^{224}Th$^* \longrightarrow A_1 + A_2$						
22.65	68.69	0.974	0.00844±0.0035	0.80	0.81	92	104	0.00649	0.00845
23.46	69.49	0.991	0.04624±0.0145	0.81	0.87	95	105	0.0438	0.0431
24.37	70.41	1.009	0.4869±0.137	0.98	1.05	95	105	0.452	0.491
25.29	71.33	1.028	2.1503±0.634	1.00	1.08	98	108	2.201	2.0464
			^{224}Th$^* \longrightarrow Z_1 + Z_2$						
22.65	68.69	0.974	0.00844±0.0035	0.25	0.30	111	123	0.00545	0.00866
23.46	69.49	0.991	0.04624±0.0145	0.28	0.35	116	125	0.0428	0.0361
24.37	70.41	1.009	0.4869±0.137	0.42	0.48	118	126	0.305	0.335
25.29	71.33	1.028	2.1503±0.634	0.55	0.56	120	132	1.504	2.595

There is a very small difference in $\triangle R$ and ℓ_{max}-values, while studying the fission dynamics of isotopes of a compound nucleus [24, 25]. Thus, for decay analysis of even-even isotopes of $^{222-230}$Th* via mass-distribution at E^*_{CN} = 24.37 MeV, we have considered common $\triangle R$ = 1.0 fm and ℓ_{max} = 100 $\hbar$, using the systematic of ^{224}Th compound nucleus. Similarly, for charge-distribution which takes place comparatively at smaller distance, like $\triangle R$ = 0.45 fm and ℓ_{max} = 120 $\hbar$ values can be taken into account.

7.2.2 Mass and charge dispersion of even-even isotopes of $^{222-230}$Th*

The study based on the fusion-fission phenomena is not only for the calculation of fission cross-section, but it also provides the idea of symmetric/asymmetric mass and charge fragments produced during the disintegration of an excited CN. In view of this, the structure of fragmentation potential $V(\eta)$ is shown in Fig. 7.6 with respect to the mass number A_2 of decaying fragment from ^{222,224,226,228,230}Th*. The region of interest that is the fission valley is marked in this figure. Interestingly, two minima are observed in the fragmentation potential for each considered isotopes of Th which belong to near-symmetric and asymmetric mass region. The near mass-symmetric region corresponds to the quadrupole (β_2) deformed fragments of elongated configuration. Whereas, the presence of octupole deformation in one of the decaying nuclear partner minimizes the fragmentation potential in the mass-asymmetric region ($\eta_A \approx 0.3$). Moreover, one can notice in Fig. 7.6(a) for ^{222}Th* that, the near-symmetric fission shows deeper minima in $V(\eta)$ as compared to the asymmetric fission fragments. For ^{224}Th* case represented in Fig. 7.6(b), the minima of $V(\eta)$ observed in the asymmetric fission starts competing with the near-symmetric dip. Moving ahead, a transition is observed for heavy-mass isotopes, i.e. ^{226,228,230}Th*, as shown in panels (c)-(e) of Fig. 7.6. In other words, the minima in $V(\eta)$ becomes relatively deeper for octupole deformed fragments present in the asymmetric region, than that of near-symmetric quadrupole deformed fragments. Similar results have been observed while studying the 'charge-dispersion' of even-even isotopes of $^{222-230}$Th*, as shown in panels (a)-(e) of Fig. 7.7. Note that, from both the mass- and charge-dispersion cases, the fission fragments observed at deep valley location are identical.

In Table 7.2, we have shown the atomic and neutron numbers, respectively at the left and right subscripts, of near-symmetric and asymmetric fission fragments along with their

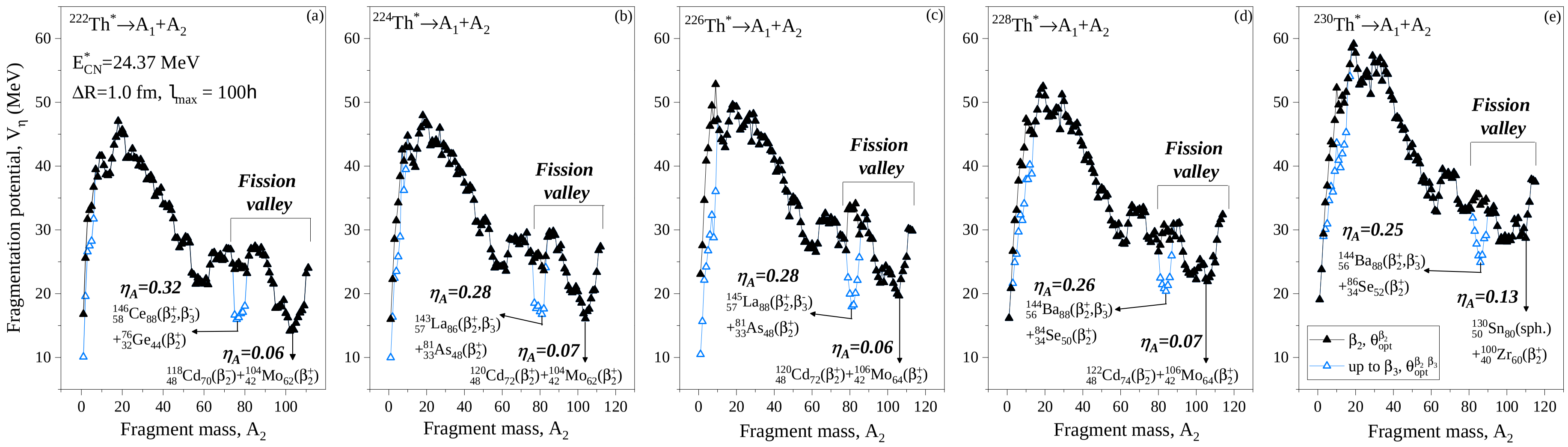

Figure 7.6: The variation of fragmentation potential $V(\eta)$ is plotted as a function of mass number A_2 firstly with the inclusion of quadrupole β_2 deformation (and related cold optimum orientation $\theta_{opt}^{\beta_2}$) and secondly octupole β_3 deformation (and $\theta_{opt}^{\beta_2\beta_3}$) of decaying fragment being involved for the decay analysis of even-even isotopes of $^{222-230}\mathrm{Th}^* \rightarrow A_1 + A_2$, at a common excitation energy $E_{CN}^* = 24.37$ MeV.

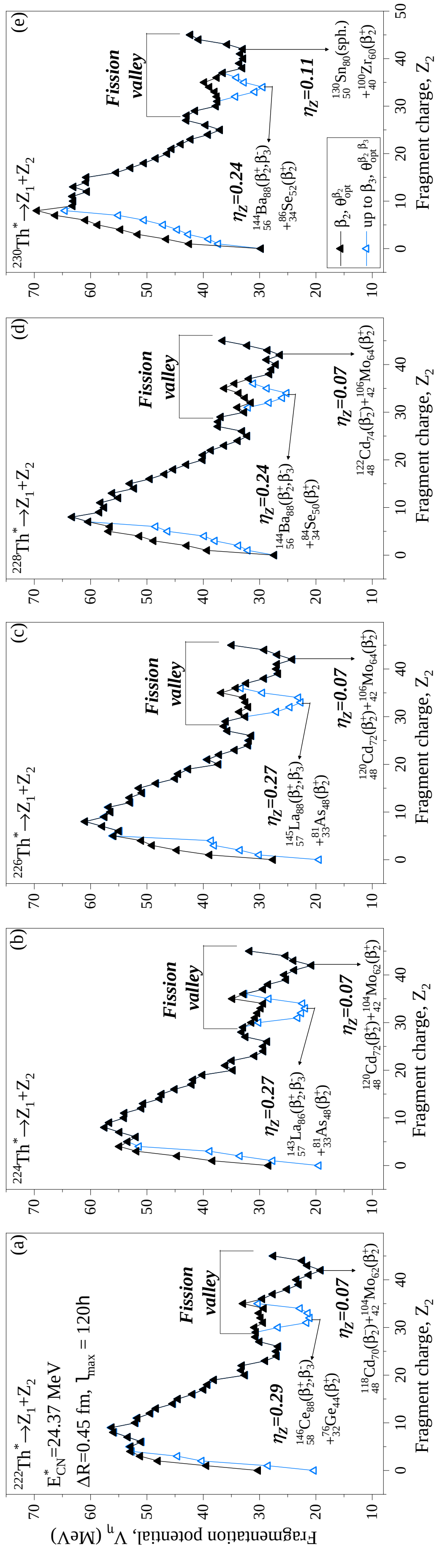

Figure 7.7: Same as Fig.7.6, but the variation of $V(\eta)$ is shown with respect to charge number Z_2 of even-even isotopes of $^{222-230}\mathrm{Th}^* \rightarrow Z_1 + Z_2$.

Table 7.2: The detail of the most probable fission fragments of quadrupole (β_{2i}; here $i = 1, 2$) and octupole deformation (β_{3i}) along with their related cold optimum orientations ($\theta_{opt}^{\beta_2}$ [7] and $\theta_{opt}^{\beta_2\beta_3}$ [8]) found respectively in the near mass/charge-symmetric and asymmetric fission regions of even-even isotopes of $^{222-230}$Th* compound nuclei are listed in the following table.

CN^*	Near mass/charge-symmetric region					Mass/charge-asymmetric region						
	Fission fragments	β_{21}	β_{22}	$\theta_{opt}^{\beta_{21}}$	$\theta_{opt}^{\beta_{22}}$	Fission fragments	β_{21}	β_{31}	β_{22}	β_{32}	$\theta_{opt}^{\beta_{21}\beta_{31}}$	$\theta_{opt}^{\beta_{22}\beta_{32}}$
$^{222}\mathbf{Th}^*$	$^{118}_{48}Cd_{70}+^{104}_{42}Mo_{62}$	-0.238	0.377	90^o	180^o	$^{146}_{58}Ce_{88}+^{76}_{32}Ge_{44}$	0.182	-0.116	0.143	0.0	0^o	180^o
$^{224}\mathbf{Th}^*$	$^{120}_{48}Cd_{72}+^{104}_{42}Mo_{62}$	0.140	0.377	0^o	180^o	$^{143}_{57}La_{86}+^{81}_{33}As_{48}$	0.154	-0.104	0.163	0.0	0^o	180^o
$^{226}\mathbf{Th}^*$	$^{120}_{48}Cd_{72}+^{106}_{42}Mo_{64}$	0.140	0.377	0^o	180^o	$^{145}_{57}La_{88}+^{81}_{33}As_{48}$	0.173	-0.128	0.163	0.0	0^o	180^o
$^{228}\mathbf{Th}^*$	$^{122}_{48}Cd_{74}+^{106}_{42}Mo_{64}$	-0.104	0.354	90^o	180^o	$^{144}_{56}Ba_{88}+^{84}_{34}Se_{50}$	0.164	-0.126	0.053	0.0	0^o	180^o
$^{230}\mathbf{Th}^*$	$^{130}_{50}Sn_{80}+^{100}_{40}Zr_{60}$	0.00	0.364	0^o	180^o	$^{144}_{56}Ba_{88}+^{86}_{34}Se_{52}$	0.164	-0.126	0.125	0.0	0^o	180^o

quadrupole (β_{2i}), octupole (β_{3i}) deformations and related cold optimum orientations ($\theta_{opt}^{\beta_2}$ and $\theta_{opt}^{\beta_2\beta_3}$). It is known that, the minimization in fragmentation potential occurs due to shell stabilization, which generally comes for magic number of nucleons, either in one or both the fission fragments. On the basis of this fact, it has been analyzed in the near-symmetric region that, the fission fragments are quadrupole deformed and one of them in decaying from light mass isotopes of Th (^{222,224}Th*) has neutron number equal to 62, which is a deformed magic number and provides shell stabilization [26]. On the other hand, in the asymmetric fission region of heavy-mass isotopes (^{226,228,230}Th*), the decaying fragment of upto octupole deformation has atomic number close or equal to 56. In the recent experimental works [10,27,28], it has been shown that, the nucleus of atomic number 56 (of ^{156}Ba element) or close to it possessing octupole deformation gives extra stability. Due to these facts, one can see minimization in $V(\eta)$ with prominent effect. In addition to the above, one can also notice from Table 7.2 that, in near-symmetric region, the magnitude of β_{21} for fragment A_1 is decreasing and becomes zero, as one goes from ^{224}Th* to ^{230}Th* case. On the other hand, in the asymmetric region, one of decay fragments is octupole deformed and another is quadrupole deformed. Here, the magnitude of β_{31} is relatively larger for fragment A_1 of heavy-mass isotopes of Th (^{226,228,230}Th*), as compared to that of light-mass isotopes. In our recent work [9], it has been said that, for larger magnitude of β_3, the elongated configuration of octupole deformed nuclei enlarges the interaction distance with a large extent and gives relatively lower barrier height. As a consequence, one can notice the corresponding effects in the fragmentation potential. From above analysis, one can notice that, the presence of deformations as well as shell-stabilization (due to magicity in nucleon number) play a significant role in the fission valley of Th.

Further, the role of deformation and orientation effect has been explored in the calculation of preformation probability P_0 as a function of mass and charge number of fission fragments preformed inside the even-even isotopes of $^{222-230}$Th*, at a common excitation energy E^*_{CN}=24.37 MeV. It is known that, the fragments for which the fragmentation potential gets minimized have the highest preformation probability. In a recent work [29], a transition of symmetric to asymmetric fission has been shown, as one moves from ^{222}Th to ^{230}Th compound nuclei. Additionally, in Ref. [30], the charge distribution of ^{222,224}Th isotopes shows a rise in the asymmetric region, but lower than symmetric fission, for excitation energy more than 11 MeV. Our calculations are in agreement with these observations. To show this,

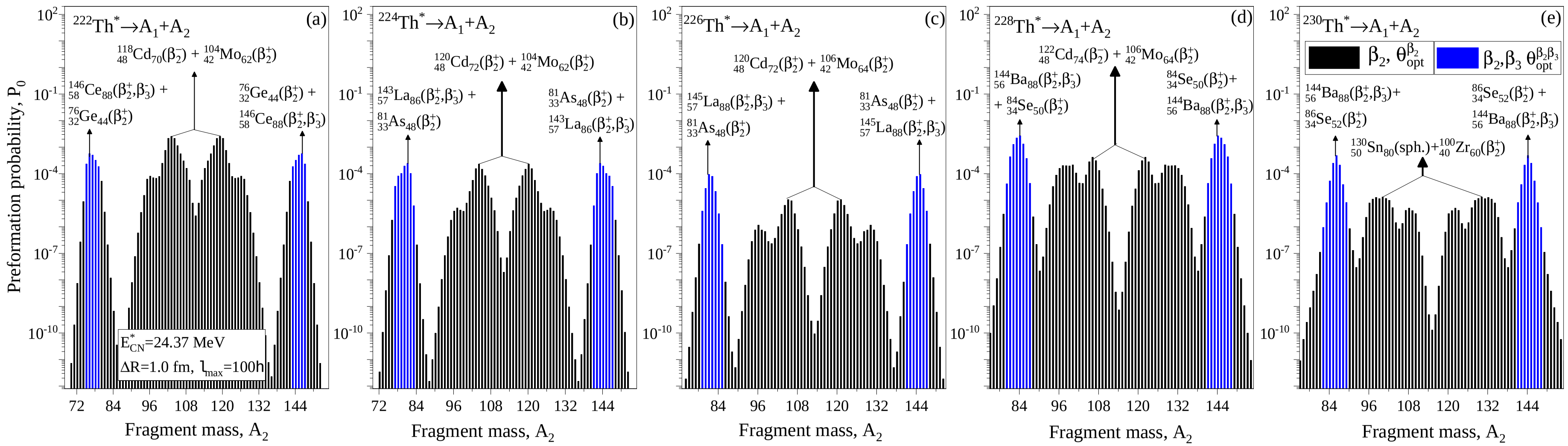

Figure 7.8: The variation of preformation probability 'P_0' as a function of mass number of decaying fragment (A_2) from the even-even isotopes of $^{222-230}$Th$^* \rightarrow A_1 + A_2$ is shown firstly with the inclusion of quadrupole β_2 deformation and related optimum orientation ($\theta_{opt}^{\beta_2}$) and secondly higher-order deformations (up to β_3) and $\theta_{opt}^{\beta_3}$ being involved.

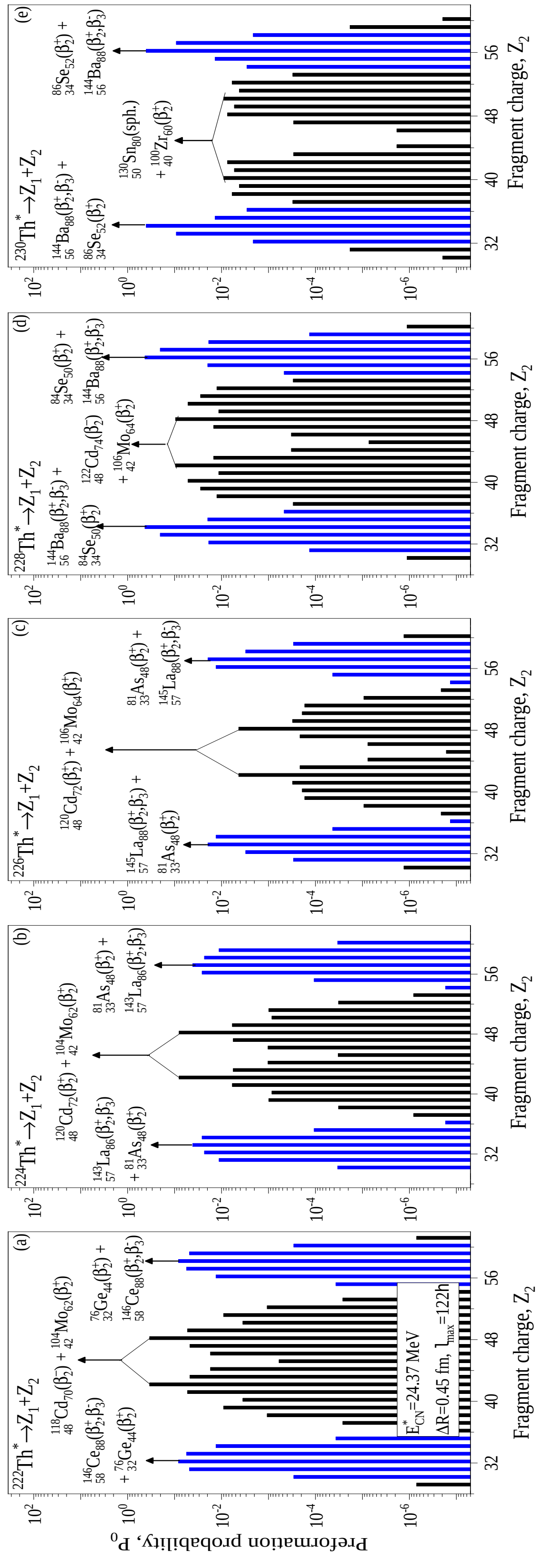

Figure 7.9: Same as Fig. 7.8, but for the charge dispersion case, i.e. $^{222-230}$Th$^* \to Z_1 + Z_2$.

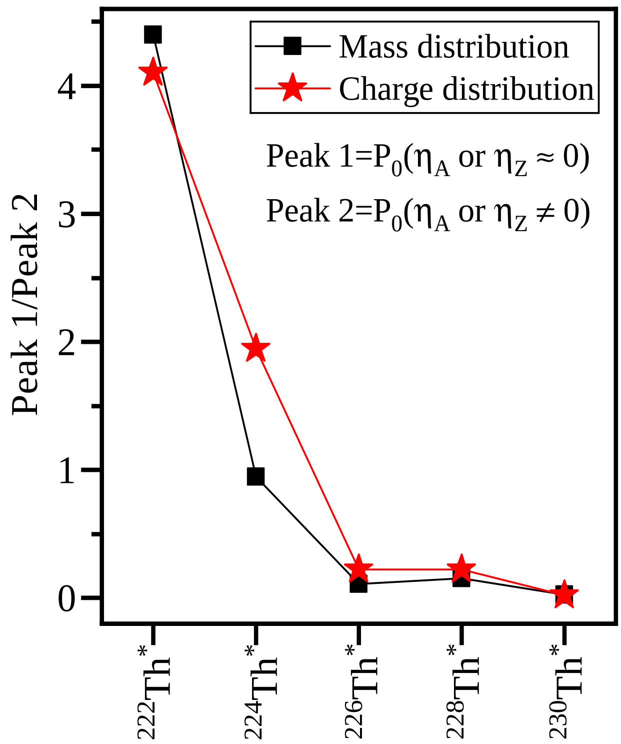

Figure 7.10: The ratio of Peak 1 [= $P_0(\eta_A$ or η_Z $\approx$0)] and Peak 2 [= $P_0(\eta_A$ or η_Z $\neq$0)] obtained for even-even isotopes of ^{A}Th*, here A = 222, 224, 226, 228 and 230, at a common excitation energy, E^*_{CN} = 24.37 MeV.

the preformation probability (P_0) of even-even isotopes of $^{222-230}$Th* are discussed and also shown in Figs. 7.8 and 7.9 respectively for mass- and charge-dispersion cases. It is clear from these figures that, the octupole deformed nuclei always appear in the asymmetric mass regions, irrespective of the choice of mass and excitation energy range considered in the present work. In the above analysis, the near-symmetric fission is found dominant over asymmetric fission for ^{222}Th* case, at E^*_{CN} = 24.37 MeV. For ^{224}Th*, the contribution of near-symmetric and asymmetric components is comparable. On the other hand, for heavy-mass isotopes ^{226,228,230}Th*, the octupole deformed decaying nuclear partner of atomic number equal or close to 56 (^{145}La and ^{144}Ba) in asymmetric region shows dominant behavior. In other words, it can be said that, the asymmetric fission fragments of octupole-quadrupole deformed kind (^{145}La+^{81}As, ^{144}Ba+^{84}Se and ^{144}Ba+^{86}Se) enhances the preformation probability P_0 with a larger extent. Also, in a recent experimental work [10], the authors have given the evidence of pear-shape nuclei (i.e. ^{144}Ba) in asymmetric region of heavy-mass actinides and the present work is in line with the result of experimental observations.

Further, the ratio of preformation probability P_0 peaks obtained near the symmetric region (Peak 1) and the one in the asymmetric region (Peak 2) is shown in Fig. 7.10 for

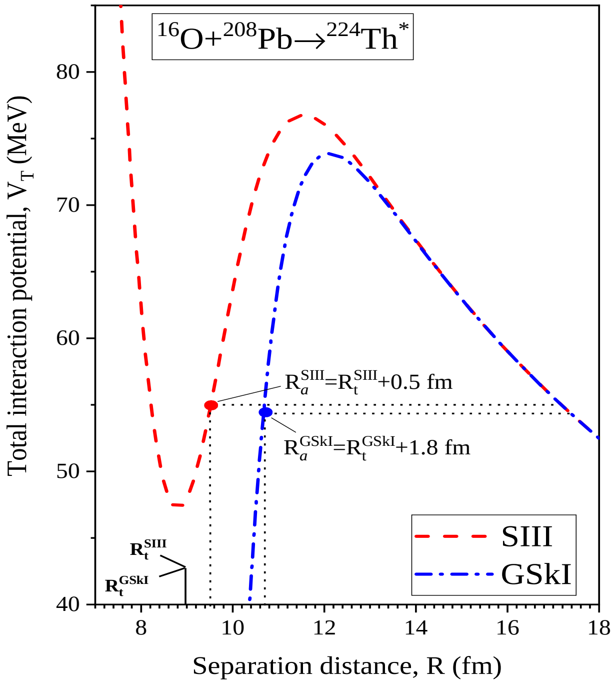

Figure 7.11: Same as Fig. 7.1, but for Prox77 [31], SIII [32] and GSkI [33] Skyrme forces.

^{222,224,226,228,230}Th* fission nuclei. In this figure, the ratio $\left(\frac{Peak1}{Peak2}\right)$ is obtained for both the mass- as well as charge-distributions of above said compound nuclei. It is observed that, the peak ratio decreases with increase in mass number of compound nuclei. Clearly, the lighter-mass compound nuclei prefer near-symmetric fragmentation of quadrupole-quadrupole deformed pairs of fission fragments. However, asymmetric fission of octupole-quadrupole deformed fragments is prominent in the heavier isotopes, i.e. ^{226,228,230}Th*.

7.2.3 Role of different Skyrme forces in mass and charge distributions of ^{224,230}Th* nuclei

Apart from above, the role of different choices of Skyrme forces has also been explored in terms of the mass and charge distributions of ^{224,230}Th* isotopes. Out of numerous Skyrme forces available in literature [33–40], we have considered SIII (an earlier version) [32] and GSkI (a modified version which considers the isospin dependence) [33], and subsequently cover a wide range of barrier characteristics, as shown in Fig. 7.11. For the mass and charge dispersion analysis of above said Thorium isotopes, the fission modes are studied at

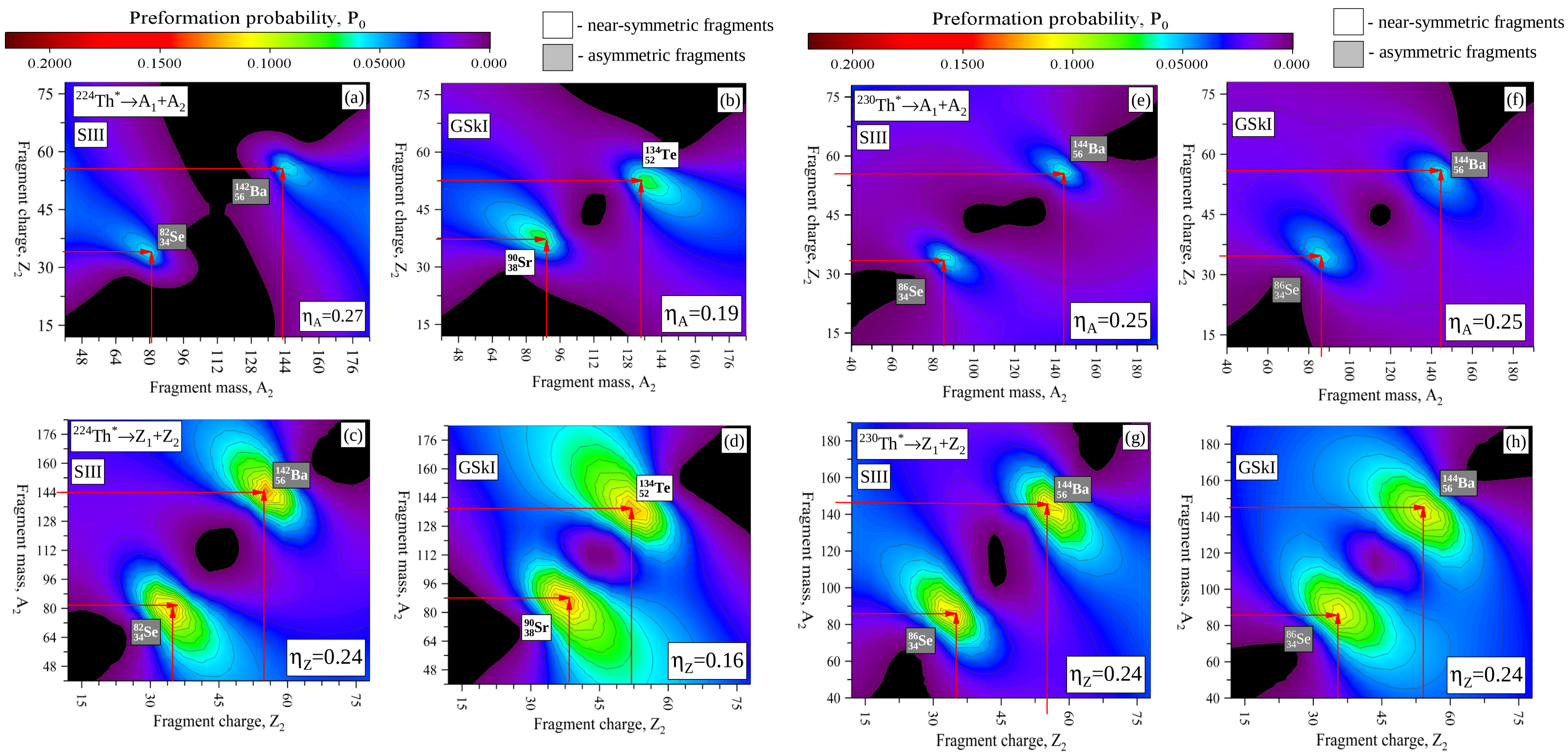

Figure 7.12: The color map represents the mass and charge distributions of $^{224,230}Th^*$ isotopes in terms of preformation probability, P_0, using two different Skyrme forces, i.e. SIII and GSkI.

$E^*_{CN} \approx 20$ MeV using above said Skyrme forces within the SEDF approach. As said earlier in the discussion of Fig. 7.1 that, the preformed clusters/fragments within the compound nuclear system start to penetrate through the first classical tunneling point i.e. R_a and terminates through the second point R_b. Due to different choices of nuclear potentials, the corresponding changes in total interaction potential V_T come into picture, and subsequently modify the tunneling path, as shown in Fig. 7.11 for SIII and GSkI forces. With such modifications, we intend to analyze the role different Skyrme forces in the mass as well as charge distributions of compound nucleus. The color maps of Fig. 7.12 represent the mass/charge distribution in terms of preformation probability, P_0, for masses $A = 224$ and 230 of Th. The color indicates the scales of P_0 for the fission fragments falling in the near-symmetric and asymmetric regions.

For ^{224}Th* case, using SIII force, the decay fragments (^{96}Zr, ^{128}Sn) in the near-symmetric region have relatively lower preformation probability than the fragments of asymmetric region (^{82}Se, ^{142}Ba), see panels (a) and (c) of Fig. 7.12. However, with the use of modified version of Skyrme force i.e. GSkI, the near-symmetric fission fragments (^{90}Sr, ^{134}Te) have larger possibility of emission from ^{224}Th* compound nucleus, as compared to asymmetric fragments (^{81}As, ^{143}La), as shown in panels (b) and (d) of Fig. 7.12. The above results hold true for both the mass as well as charge dispersion cases. As per earlier study [30] for E^*_{CN} around 20 MeV, the disintegration of ^{224}Th* shows symmetric fission with larger effect from that of asymmetric fission, which seems justified for the use of GSkI force. Further, as we look on to the mass and charge distributions of heavier isotope of Thorium (^{230}Th*), both the forces show higher peak of P_0 for asymmetric fission fragments, see panels (e)-(h) of Fig. 7.12. This result is in agreement with the experimental analysis [29]. In conclusion, it can be said that, the modified version of Skyrme force (i.e. GSkI) is able to explain the symmetric and asymmetric fission modes not only for heavy-mass isotope of Th, ^{230}Th*, but also for lighter-mass nucleus ^{224}Th*.

7.3 Conclusion

In this Chapter, we have included the deformations up to β_3 and related cold optimum orientation (θ_{opt}), within the Dynamical Cluster-decay Model, to study the nuclear fission dynamics of even-even isotopes of Thorium, i.e. $^{222-230}$Th*. The above analysis is exercised at the low excitation energy, which corresponds to the cold optimum configurations of the nuclei involved.

Initially, the neck-length parameter $\triangle R$ is optimized in reference to the available experimental data of fusion cross-sections of ^{224}Th*, formed via ^{208}Pb-based reaction, at the below barrier energies. Subsequently, the dips of fragmentation potential and corresponding peaks of preformation probability are analyzed in the near-symmetric (η_A and $\eta_Z \approx 0$) and asymmetric fission (η_A and $\eta_Z \neq 0$) regions of considered isotopes. It is observed that octupole deformed fragments appear in the asymmetric region, irrespective of the mass of Th isotopes. Note that, for both the mass- as well as charge-dispersion fragmentations, the most probable fission fragments observed are found identical. In the decay of light-mass isotopes of Th, i.e. ^{222,224}Th*, the near-symmetric fission is preferred due to deformed magic number of neutrons ($N = 62$) of quadrupole deformed fragment. However, the asymmetric fission involving octupole deformed fragment ($Z = 56$; ^{144}Ba or in its vicinity) is found prominent in the case of heavier isotopes of Th, i.e. ^{226,228,230}Th*. From above analysis, the near-symmetric and asymmetric fission modes observed in the decay of Th isotopes, due to involvement of deformations (up to β_3) and related cold optimum orientation, are in agreement with the experimental results. A comparative analysis of different Skyrme forces in terms of mass- and charge-distributions with the experimentally obtained yields helps us to make a better choice of Skyrme force to study fusion-fission dynamics. In the present work, the GSkI force due to additional terms involved in the Skyrme Hamiltonian density function is found to give better results, which are in match with the available data for 'Th' isotopes.

Bibliography

[1] S. Hofmann and G. Munzenberg, Rev. Mod. Phys. **72**, 733 (2000).

[2] S. Hofmann *et al*, Eur. Phys. J. A **14**, 147 (2002).

[3] Y. T. Oganessian *et al*, Phys. Rev. C **70**, 064609 (2004).

[4] Y. T. Oganessian, J. Phys. G **34**, R165 (2007).

[5] U. Brosa, S. Grossmann and A Muller, Phys. Rep. **197**, 167 (1990).

[6] K. Nisho *et al*, Phys. Rev. C **77**, 064607 (2008).

[7] R. K. Gupta *et al*, J. Phys. G: Nucl. Part. Phys. **31**, 631-644 (2005).

[8] S. Jain, M. K. Sharma and R. Kumar, Phys. Rev. C **101**, 051601(R) (2020).

[9] S. Jain, M. K. Sharma and R. Kumar, Chin. Phys. C, Vol. **46**, 1, 014102 (2022).

[10] G. Scamps and C. Simenel, Nature **564**, 382 (2018).

[11] R. K. Gupta, in *Clusters in Nuclei*, edited by C. Beck, Lectures Notes in Physics 818, Vol. I (Springer-Verlag, Berlin, 2010), p.223.

[12] D. Jain, R. Kumar and M. K. Sharma, Phys. Rev. C **87**, 044612 (2013).

[13] A. Kaur and M. K. Sharma, Nucl. Phys. A **99**, 044611 (2019).

[14] H. J. Fink, J. Maruhn, W. Scheid, and W. Greiner, Z. Phys. **268**, 321 (1974).

[15] J. Maruhn and W. Greiner, Phys. Rev. Lett. **32**, 548 (1974).

[16] R. K. Gupta, W. Scheid, and W. Greiner, Phys. Rev. Lett. **35**, 353 (1975).

[17] M. Dasgupta *et al*, Phys. Rev. Lett. **99**, 192701 (2007).

[18] H. S. Khosla and S. S. Malik, Nucl. Phys. **A513**, 115-124 (1990).

[19] S. Kumar and R. K. Gupta, Phys. Rev. C **55**, 1 (1997).

[20] R. K. Gupta, S. Kumar and W. Scheid, Int. J Mod. Phys. E, Vol. **6**, No. 2, 259-274 (1997).

[21] S. J. Sanders *et al*, Phys. Rev. C **40**, 2091 (1989).

[22] S. Sander, Phys. Rev. C **44**, 2676 (1991).

[23] T. Matsuse, Phys. Rev. C **55**, 1380 (1997).

[24] M. K. Sharma, G. Sawhney, R. K. Gupta and W. Greiner, J. Phys. G: Nucl. Part. Phys. **38**, 105101 (2011).

[25] N. Gover, I. Sharma, G. Kaur and M. K. Sharma, Nucl. Phys. A **959**, 10-26 (2017).

[26] A. Kaur, N. Sharma and M. K. Sharma, Phys. Rev. C **103**, 034618 (2021).

[27] B. Bucher *et al*, Phys. Rev. Lett. **116**, 112503 (2016).

[28] B. Bucher *et al*, Phys. Rev. Lett. **118**, 152504 (2017).

[29] A. Chatillo *et al*, Phys. Rev. C **99**, 054628 (2019).

[30] H. Pasca *et al*, Phys. Rev. C **94**, 064614 (2016).

[31] J. Blocki *et al*, Ann. Phys. **105**, 427-462 (1977).

[32] M. Brack, C. Guet, H. -B. Hakanson, Phys. Rep. **123**, 275-364 (1985).

[33] B. K. Agarwal, S. Shlomo and V. Kim Au, Phys. Rev. C **72**, 014310 (2005).

[34] D. M. Brink and Fl. Stancu, Nucl. Phys. A**243**, 175-188 (1975).

[35] Fl. Stancu and D. M. Brink, Nucl. Phys. A**270**, 236-254 (1976).

[36] D. M. Brink and Fl. Stancu, Nucl. Phys. A**299**, 321-332 (1978).

[37] Keh-Fei LIU *et al*, Nucl. Phys. A**534**, 1-24 (1991).

[38] Lie-Wen Chen *et al*, Phys. Rev. C **82**, 024321 (2010).

[39] M. Dutra *et al*, Phys. Rev. C **85**, 035201 (2012).

[40] Zhen Zhang and Lie-Wen Chen, Phys. Rev. C **94**, 064326 (2016).

Chapter 8

Summary and Outlook

In this thesis, the main focus is to study the formation of compound nuclear systems and subsequent decay mechanisms, which are induced via heavy-ion reactions at the low-energy regime i.e. $\leq$15 MeV/nucleon. For the above analysis, the nucleus-nucleus interaction potential plays an important role and is used to investigate the role of different nuclear properties in the fusion and the decay mechanisms. The semiclassical approach of Skyrme Energy Density Formalism (SEDF) has been employed to derive the effective nuclear interaction potential. Further, the fusion barrier characteristics extracted from the total interaction potential are used as input in the calculation of fusion cross-sections, which are estimated using the Wong formula and its extended version. The subsequent decay mechanisms of formed Compound Nucleus (CN) have been studied within the framework of Dynamical Cluster-decay Model (DCM). This model is based on the collective clusterization approach of Quantum Mechanical Fragmentation Theory (QMFT).

Within the framework of SEDF, the effect of different nuclear density approximations, i.e. sudden, modified sudden and frozen density approximation, has been analyzed in terms of the fusion barrier characteristics and subsequently on the fusion cross-sections for a variety of CN, formed via ^{58}Ni-based reactions, over a wide range of incident energies. For comparative analysis, the phenomenological Woods-Saxon potential parameterized under the relaxed-density approximation has been used for the above mentioned reactions. In results, for the selected choices of projectile-target combinations (^{18}O, ^{40}Ca, ^{58}Ni and ^{132}Sn+^{58}Ni), the frozen density approximation is found to give relevant details of the fusion barrier characteristics (barrier position R_B, barrier height V_B and barrier curvature $\hbar\omega_B$), which in turn, address the available experimental data across the Coulomb barrier energies. In context to the other choices of density approximations, the modified-sudden density approximation gives almost similar magnitude of R_B, V_B and $\hbar\omega_B$ as that of frozen density approximation and gives good agreement with the experimental data for the lighter (^{76}Kr* and ^{98}Cd*) and medium mass (^{116}Ba*) CN systems, formed via ^{18}O, ^{40}Ca and ^{58}Ni+^{58}Ni reactions. On the other hand, for these projectile-target combinations, the sudden and relaxed-density approximations show the fusion hindrance at the sub-barrier energies. For heavy-mass system, i.e. ^{190}Pt* formed via ^{132}Sn+^{58}Ni reaction, the relaxed-density approximation starts behaving alike frozen-density approximation and gives relevant barrier characteristics in addressing the fusion cross-sections for the available energies.

Further, with the use of the semiclassical SEDF approach, the corresponding effect of two- (2pF) and three-parameter (3pF and 3pG) density functions has been explored in the calculation of fusion barrier characteristics (due to relative change in the tail and nearby region of nuclear density). The collective effect of V_B, R_B and $\hbar\omega_B$ has been analyzed in determining the fusion cross-sections using the extended ℓ-summed Wong model for mass-symmetric (^{58}Ni+^{58}Ni) and asymmetric (^{8}B, ^{18}O and ^{132}Sn+^{58}Ni) choices of ^{58}Ni-based reactions. The obtained results are compared with the available experimental data for the above said colliding nuclear partners over a wide range of incident energies. For the symmetric reaction, it is observed that, the density profile of 2pF density function is different in the vicinity of tail region, which is incepted due to its larger value of half-density radius (or equivalently lower barrier height), from that of the three parameter density functions i.e. 3pF and 3pG. As a consequence, the 2pF density function reduces the fusion hindrance and gives better agreement with the data of ^{58}Ni+^{58}Ni reaction using SLy4 Skyrme force. On the other hand, for the case of mass-asymmetric nuclear reaction partners, the 3pF and 3pG density functions has larger half-density radius, which in turn, lowers the barrier height in comparison to 2pF case. Hence, the three-parameter density functions are found to give better comparison of fusion cross-sections with the data, for ^{8}B, ^{18}O and ^{132}Sn+^{58}Ni reactions especially at the below barrier energies. It is worth mentioning that the tail and nearby region of the density distributions play an important role in the heavy-ion induced reactions.

With different choices of density approximations and density distribution functions employed within the semiclassical SEDF approach, I have analyzed the corresponding influence on the fusion barrier characteristics, which are sensitive towards the deformation and orientation degrees of freedom. Therefore, in further study, the relevance of these factors has been explored in synthesizing heavy and superheavy nuclei via hot and cold fusion processes. Initially, I have obtained the optimum orientations (θ_{opt}) for the 'elongated or cold' and 'compact of hot' fusion configurations of octupole (β_3) deformed nuclei. Due to distortion in the spherically symmetric shape nuclei with the inclusion of deformations up to β_3, the pear shape of octupole deformed nucleus modifies the hot and cold optimum orientations from the ones reported for the quadrupole β_2-deformed nuclei. The optimum orientations obtained for β_3-deformed nuclei are dependent on +/- signs as well as the magnitude of β_3-deformation. In addition to this, it has also been observed that the values of θ_{opt} obtained with the effect of β_3-deformation are independent of the choice of nuclear potential and the nuclear radius. On the basis of above results, I have investigated the impact of soft- (with small β_3-deformation) and rigid-pear shapes (with strong β_3-deformation) of octupole deformed nuclei on the fusion barrier characteristics. The analysis has been exercised to approximately 200 spherical-plus-β_3 deformed nuclear partners, that is, ^{16}O, ^{48}Ca+octupole deformed nuclei. It has been observed that, the cold fusion configuration of octupole deformed nuclei show relatively larger impact on the fusion barrier and subsequently on the fusion cross-sections, in comparison to the hot fusion configuration. This result in agreement with the available experimental data for the ^{16}O+^{150}Sm (β_{22} = 0.205, β_{32} = -0.055) reaction improves when the optimum orientation is fixed in view of the octupole deformations. Such analysis reinforces that the nuclear structure effects play an important role in nuclear fusion dynamics. Consequently, it can be said that the octupole deformed nuclei can be used for the synthesis of heavy and superheavy elements.

Furthermore, in the de-excitation process of the formed compound nuclear system, the role of deformations up to β_3 and related cold optimum orientation has been explored within the framework of the DCM. As per earlier investigations, it has been observed that, the spherical and quadrupole deformed nuclei with the closed shells are found to be more probable fission fragments in the decay of heavy-mass compound nuclei at the low excitation energies. In this theoretical work, an exercise is done to analyze the possibility of octupole deformed fragments in the decay of light- and heavy-mass isotopes of Thorium, i.e. ^{222,224,226,228,230}Th*. To carry forward with this idea, the mass and charge dispersions of chosen 'Th' isotopes have been analyzed by including deformations (up to β_3) and related cold optimum orientations within the DCM, which is based on the collective clusterization approach of the QMFT. The analysis is worked out at the low excitation energy, which correspond to the cold synthesis criteria. In the decay of light-mass isotopes of Th, i.e. ^{222,224}Th*, the near-symmetric fission is preferred possibly due to deformed magic number of neutrons (N = 62) of the quadrupole deformed fragment. However, the asymmetric fission involving an octupole deformed fragment (Z = 56; ^{144}Ba and in its vicinity) is found to be prominent in the case of heavier isotopes of Th, i.e., $^{226,228,230}\mathrm{Th}^*$. From the above analysis, the near-symmetric and asymmetric fission modes observed in the decay of Th isotopes, due to involvement of deformations (up to β_3) and related cold optimum orientation, are in agreement with the experimental data. Such investigations help in understanding the fission dynamics, especially in the asymmetric region of heavy-mass actinides.

In conclusion, the effective nuclear interaction potential derived using SEDF approach is employed to address the nuclear fusion-fission dynamics. From this analysis, it has been observed that, the densities added in frozen way offers a larger reaction time as compared to the other density approximations. Such situation gives larger possibility of fusion among two nuclei and also justifies the experimentally obtained fusion cross-sections. Moving ahead with this result, I have examined the significance of different density distribution functions at the sub-barrier region for Ni-based reactions. The involvement of wine-bottle parameter in three-parameter density functions has been found to give better agreement with the data of mass-asymmetric colliding nuclear partners, especially at the sub-barrier region. On the other hand, the two-parameter density function is found to be a better choice for the symmetric reactions.

Apart from above, while investigating the relevance of deformations and orientations degrees of freedom in nuclear fusion-fission dynamics using the SEDF and phenomenological potentials, the pear-shape nuclei and the respective optimum orientations have been found to contribute significantly in the formation of heavy/superheavy compound nuclear systems with larger extent from that of quadrupole deformed nuclei. Also, in the de-excitation of heavy-mass isotopes of Thorium, the octupole deformed nuclei have been found to emit out with relatively larger probability, in comparison to the spherical and quadrupole deformed fragments.

FUTURE SCOPE

The present work can be extended by analyzing the density profile of exotic nuclei, e.g. proton- and neutron-drip line elements, in reference to the nuclei lying along the β-stability line. Also the corresponding influence can be investigated in the fusion-fission dynamics. In the above analysis, a comparison between the microscopic and semiclassical calculations can be exercised at the deep sub-barrier regions.

In heavy-ion collision, the tail and its nearby region of nuclear density play a very important role. In the present work, the importance of two- and three-parameter density functions has been explored for the spherical choices of projectile-target combinations in terms of fusion barrier characteristics. Further, in the extension of this work, one may also analyze the influence of deformation/orientation degrees of freedom and temperature effects in the tail and near-by region of the density profile, which would affect the fusion barrier characteristics and fusion cross-sections at the sub-barrier region. The above analysis can be exercised with the use of semiclassical Skyrme Energy Density Formalism and also for comparative analysis at the deep sub-barrier energies, the nucleus-nucleus potential derived using the microscopic calculations can be used.

Additionally, to have a comprehensive knowledge about the deformation and orientation degrees of freedom in the fusion-fission dynamics, the significance of higher-order deformations can be explored in comparison to that of symmetry-breaking pear shape octupole deformed nuclei. This study can be discussed for the co-planar and non co-planar interactions of spherical-deformed and deformed-deformed pairs of colliding nuclei, which may lead toward the formation of heavy and superheavy elements.